Yann Gaillard

Numerical investigation of thermo-electrohydrodynamic driven convection in spherical Taylor-Couette flow

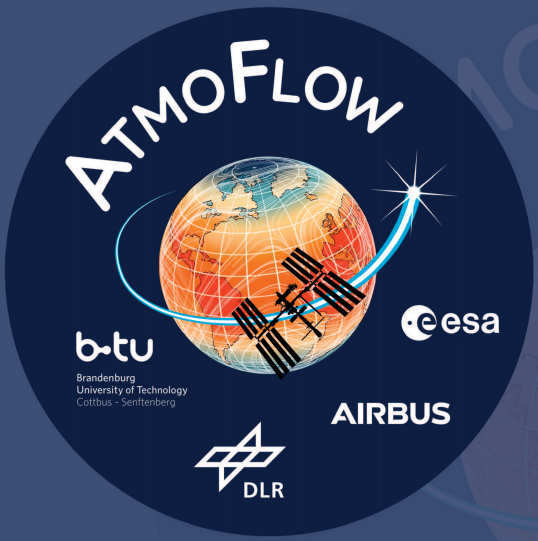

Cuvillier Verlag Göttingen
Internationaler wissenschaftlicher Fachverlag

Numerical investigation of thermo-electrohydrodynamic driven convection in spherical Taylor-Couette flow

Numerical investigation of thermo-electrohydrodynamic driven convection in spherical Taylor-Couette flow

Von der Fakultät für Maschinenbau, Elektro- und Energiesysteme
der Brandenburgischen Technischen Universität CottbusSenftenberg
zur Erlangung des akademischen Grades eines
Dr.-Ing.

genehmigte Dissertation
vorgelegt von

M.Sc. (TUM)
Yann Ingo Philippe Gaillard

geboren am 09.01.1996 in Karlsruhe

Vorsitzender: Prof. Dr. rer. nat. Uwe Harlander

1. Gutachter: Prof. Dr.- Ing. Christoph Egbers
2. Gutachterin: Prof. Dr. rer. nat. Susanne Horn
3. Gutachter: Prof. Dr. rer. nat. Florian Zaussinger

Tag der mündlichen Prüfung: 08.09.2025

Impressum

Titel des Werkes: Numerical investigation of thermo-electrohydrodynamic driven convection in spherical Taylor-Couette flow
Autor: Yann, Ingo, Philippe Gaillard
Cuvillier Verlag GmbH Nonnenstieg 8 37075 Göttingen
Telefon: 0049-551-547240
Webseite: www.cuvillier.de **E-Mail:** info@cuvillier.de

Bibliografische Informationen der Deutschen Nationalbibliothek
Die Deutsche National-bibliothek verzeichnet diese Publikation in der Deutschen Nationalbibliografie; detaillierte bibliografische Daten sind im Internet über http://dnb.dnb.de abrufbar.

1. Auflage, Göttingen. 2025
Zugl.: BTU Cottbus-Senftenberg, Univ., Diss., 2025
1. Gutachter: Prof. Dr.- Ing. Christoph Egbers
2. Gutachterin: Prof. Dr. rer. nat. Susanne Horn
3. Gutachter: Prof. Dr. rer. nat. Florian Zaussinger
Vorsitzender: Prof. Dr. rer. nat. Uwe Harlander
Tag der mündlichen Prüfung: 08.09.2025

ISBN 978-3-68952-375-6
eISBN 978-3-68952-376-3
ORCID 0000-0003-4464-8901
ISNI 0000 0005 2894 9792
DOI 10.61061/ISBN_9783689523756

Abstract

Thermo-Electrohydrodynamics (TEHD) investigates convection in dielectric fluids triggered by electric fields. In a spherical geometry, TEHD convection produces radially oriented plume structures, while differential rotation, realised as spherical Taylor-Couette (sTC) flow, drives meridional and azimuthal flow. When combined, these heterogeneous forcing mechanisms generate a wide variety of flow regimes and patterns due to the interplay between dielectrophoretic (DEP) and rotation-induced forces.

This study examines the interaction between TEHD convection and rotation-driven flow in the context of the AtmoFlow experiment, an upcoming spherical-shell experiment to be deployed on the International Space Station (ISS) by 2026. An idealised numerical model is developed using a finite volume solver based on the OpenFOAM ecosystem. The solver employs a modified, time-resolving SIMPLE algorithm incorporating Gauss's law to compute the electric field and the DEP force under non-isothermal conditions.

The basic flows driven independently by TEHD and sTC forcing are first characterised. TEHD convection is benchmarked against classical Rayleigh-Bénard convection, with scaling relations derived for heat transport (Nusselt number, Nu) and kinetic energy ($\tilde{E}_{\mathrm{kin}}$) as functions of the electric Rayleigh number ($\mathrm{Ra_E}$). Likewise, steady and transient sTC flow regimes are analysed in the co-rotating frame, using key dimensionless parameters such as the Taylor number (Ta) and Rossby number (Ro). These flows exhibit meridionally dominant flow and tangent cylinder structures. Scaling laws are formulated for Nu and $\tilde{E}_{\mathrm{kin}}$ in each regime.

The combined TEHD-sTC system is then investigated to understand the competing effects of radial DEP-driven convection and the meridional-azimuthal sTC flow. Transitional behaviour in heat transport, from DEP-dominated to rotation-driven regimes, is analysed using a custom-defined in-flow Nusselt number (Nu^q) that separates conductive and convective heat transfer within the fluid bulk.

Finally, the influence of heterogeneous thermal boundary conditions is explored. The resulting thermal convection patterns are analysed using Empirical Orthogonal Functions (EOF) and Fast Fourier Transforms (FFT), leading to a regime classification diagram that captures the dominant structures in the flow.

Zusammenfassung

Die Thermo-Elektrohydrodynamik (TEHD) untersucht die Konvektion in dielektrischen Fluiden, die durch elektrische Felder angeregt wird. In einer sphärischen Geometrie erzeugt die TEHD radial ausgerichtete Plumenstrukturen, während die differentielle Rotation auch als sphärische Taylor-Couette-Strömung (sTC) bekannt meridionale und azimutale Strömungen antreibt. Die Überlagerung dieser heterogenen Strömungen führt zu einer Vielzahl komplexer Regime und Strömungsmuster, die aus dem Zusammenspiel dielektrophoretischer (DEP) und rotationsinduzierter Kräfte entstehen.

In dieser Studie wird die Wechselwirkung zwischen TEHD-Konvektion und rotationsgetriebener Strömung im Kontext des AtmoFlow-Experiments untersucht. Bei diesem sphärischen Schalenexperiment, das ab 2026 auf der Internationalen Raumstation (ISS) zum Einsatz kommen wird, werden die Effekte der TEHD-Konvektion auf die rotationsgetriebene Strömung analysiert. Mithilfe eines Finite-Volumen-Lösers, der mittels OpenFOAM programmiert ist, wird ein idealisiertes numerisches Modell entwickelt. Der Löser verwendet einen modifizierten, zeitauflösenden SIMPLE-Algorithmus, der die Gaußgleichung zur Berechnung des elektrischen Feldes und der DEP-Kraft unter nichtisotheren Randbedingungen berücksichtigt.

Zunächst werden die Grundströmungen untersucht, die jeweils durch TEHD oder sTC separat erzeugt werden. Die TEHD-Konvektion wird mit der klassischen Rayleigh-Bénard-Konvektion verglichen. Dabei werden Skalierungsgesetze für den Wärmetransport (Nusselt-Zahl, Nu) und die kinetische Energie ($\tilde{E}_{\mathrm{kin}}$) in Abhängigkeit von der elektrischen Rayleigh-Zahl ($\mathrm{Ra_E}$) erstellt. Ebenso werden stationäre und transiente sTC-Strömungsregime im mitrotierenden Bezugssystem analysiert und durch die Taylor-Zahl (Ta) und die Rossby-Zahl (Ro) charakterisiert. Dabei zeigen sich meridional dominierte Grundströmungen und Strukturen wie die des Tangentialzylinders. Auch für die resultierenden Strömungen werden Skalierungsgesetze für Nu und $\tilde{E}_{\mathrm{kin}}$ formuliert.

Anschließend wird das kombinierte TEHD-sTC-System untersucht, um die konkurrierenden Effekte zwischen radialer, durch DEP angetriebener Konvektion und der meridional-azimutalen sTC-Strömung zu verstehen. Das Übergangsverhalten des Wärmetransports von DEP-dominierten zu rotationsdominierten Regimen wird mithilfe einer eigens definierten Strohm-Nusselt-Zahl (Nu^q) analysiert. Diese teilt den Wärmetransport im Spalt in seine konduktiven und konvektiven Anteile auf.

Abschließend wird der Einfluss heterogener thermischer Randbedingungen untersucht. Die entstehenden thermischen Konvektionsmuster werden mittels empirischer Orthogonalfunktionen (EOF) und Fast-Fourier-Transformationen (FFT) analysiert. Daraus

ergibt sich ein Regimeklassifikationsdiagramm, das die dominanten Strukturen in der Strömung erfasst.

Contents

List of Figures

List of Tables

Nomenclature

Greek letters

λ_{D}	Debye length
ΔT	Temperature gap
ϵ	Permitivity
ϵ_0	Vacuum permittivity
ϵ_{r}	Relative permittivity
η	Aspect ratio
κ	Thermal diffusivity
$\mathbf{\Omega}$	Rotation vector
μ	Dynamic viscosity
ν	Kinematic viscosity
ω	Dimensionless angular velocity
Ω_1	Angular velocity of the inner sphere
Ω_2	Angular velocity of the outer sphere and simultaneously of the rotating reference frame
ϕ	Electric potential
ρ	Density
ρ_0	Density at reference temperature T_0
ρ_e	Electric charge density

σ Criticality

σ_e Electric conductivity

τ Dimensionless time

τ_κ Thermal time scale

τ_ν Viscous time scale

τ_e Electric time scale

τ_m Migration time scale

τ_D Diffusion time scale

τ_{ij} Stress tensor

ϖ Dimensionless relative rotation rate

ϑ Dimensionless electric potential

Latin letters

$\tilde{E}_\mathrm{kin}$ Averaged kinetic energy

$\mathbf{d}_\mathrm{p}$ Dipole moment

$\mathbf{E}$ Electric field vector

$\mathbf{E}_{\mathrm{b},\gamma_\mathrm{e}}$ Conductive base state temperature dependent electric field vector

$\mathbf{E}_\mathrm{b}$ Conductive base state electric field vector

$\mathbf{g}_\mathrm{e}$ Electric gravity vector

$\mathbf{n}$ Normal vector

$\mathbf{u}$ Velocity vector

$\mathbf{x}$ Cartesian location vector

A Surface area

A_m Amplitude of mode m

c_p Heat capacity

d	Charactersitic length
e	Permitivity thermal coefficient
f	Frequency
h	Enthalpy
J^{ω}	Angular momentum flux
L	Angular momentum
P	Pressure including the static part
p	Pressure
Q_{cond}	Conductive heat-flux
Q_{t}	Total heat-flux
r	Radius
r_1	Dimensionless inner radius
r_2	Dimensionless outer radius
$R_{1/2}$	Dimensional mid-gap
$r_{1/2}$	Dimensionless mid-gap radius
$r_{1/4}$	Dimensionless quarter gap radius
$r_{3/4}$	Dimensionless three-quarter gap radius
T	Temperature
t	Time
T_0	Reference temperature
T_{b}	Conductive base state temperature
u_θ	Meridional velocity
u_φ	Azimuthal velocity
u_r	Radial velocity

u_T Thermal wind

V Votage over time from AC source

V_0 Effective voltage from AC source

var_{exp} Explained variance

g_{e} Electric gravity scalar

m Mass

Dimensionless numbers

CFL Courant-Friedrichs-Lewy number

γ_{e} Thermo-electric parameter

Nu Nusselt number

Nu^{ω} Angular momentum Nusselt number

Nu^{q} In-flow Nusselt number

Pe Peclet number

Pr Prandtl number

Ra_{E} Electric Rayleigh number

Ro Rossby number

Ta Taylor number

Re Reynolds number

Abbreviations

AC Alternative current

BE Backward-Euler

BTU Brandenburg University of Technology

CK Crank-Nicolson

DC Direct current

DEP Dielectrophoretic

DNS Direct numerical simulation

EHD Electrohydrodynamic

EOF Empirical orthogonal function

EP Electrophoretic

ES Electrostrictive

FEM Finite Element Method

FFT Fast Fourier Transformation

FVM Finite volume mehod

GAMG Geometric-Algebraic MultiGrid

ISS International space station

PAS Pseudo-analytic solution

PCA Principal component analysis

PDE Partial differential equation

PISO Pressure-Implicit with Splitting of Operators

PIV Particle image velocimetry

PSM Pseudo Spectral Method

RoI Region of interest

SIMPLE Semi-Implicit Method for Pressure-Linked Equation

sTC Spherical Taylor-Couette

STME Spatial thermal mode energy

TC Taylor-Couette

TEHD Thermo-electrohydrodyamic

WSI Wollaston-schlieren-interferometry

Miscellaneous

$< \cdots >_A$ Surface averaged

$< \cdots >_t$ Time averaged

$< \cdots >_V$ Volumetric averaged

$\overline{(\ldots)}$ Mean operator

Acknowledgements

I express my deepest gratitude to my professor, Prof. Dr.-Ing. Christoph Egbers and my supervisor, Dr. Peter Szabo, for their invaluable guidance, support, and encouragement throughout this project. I am especially thankful to Peter for continuously motivating me and pushing me through the final stages. I also extend my sincere thanks to Prof. rer. nat. habil. Uwe Harlander for the many insightful discussions on differential rotation, which often pleasantly drifted into conversations about gliding and aviation. Their expertise and perspectives have significantly shaped the direction and depth of my research.

Thanks to my colleagues, Peter Haun, Matthias Strangfeld, Franz-Theo Schön, Kushal Nagaraj, Yousuf Ali Mohammed, Robin Stöbel, and Silke Kaschwich, for making this journey enjoyable and encouraging lunchtime discussions. I would like to thank my friend Lucas Brenner for taking the time to read my thesis and for providing valuable remarks and suggestions.

I would also like to sincerely thank the Deutsches Zentrum für Luft- und Raumfahrt (DLR) for funding this project and Airbus for constructing the experimental setup. I am grateful to Nationales Hochleistungsrechnen (NHR) for providing the essential computational resources that made this research possible.

Finally, I would like to extend my heartfelt thanks to my family, my partner Annabell, and my children, Isaak and Yaron, for their endless patience, understanding, and unwavering encouragement. Their steadfast support has been my anchor throughout this endeavour.

List of publications

Author: Yann Gaillard

Journal articles

1. Y. Gaillard, P. S. B. Szabo and C. Egbers, Convection in spherical Taylor-Couette flow under the influence of the dielectrophoretic force *Journal of Fluid Mechanics*, **vol.**, submitted May 2025.

2. V. Travnikov, P. S. B. Szabo, Y. Gaillard, and C. Egbers, Centrifugally driven spherical gap convection with polar angle-dependent boundary condition: Can the Nusselt number fall below unity?, *Physics of Fluids*, **vol. 37**, no. 8, p. 083618, Aug. 2025, doi: 10.1063/5.0281082.

3. Y. Gaillard, P. S. B. Szabo, V. Travnikov, and C. Egbers, Modelling Thermo-Electrohydrodynamic Convection in Rotating Spherical Shell Using OpenFOAM, *OpenFOAM Journal*, **vol. 5**, pp. 116, Jan. 2025, doi: 10.51560/ofj.v5.136.

4. Y. Gaillard, P. S. B. Szabo, V. Travnikov, and C. Egbers, Thermo-electrohydrodynamic convection in a rotating shell with central force field, *International Journal of Heat and Mass Transfer*, **vol. 218**, p. 124760, Jan. 2024, doi: 10.1016/j.ijheatmasstransfer.2023.124760.

5. Y. Gaillard, P. S. B. Szabo, and C. Egbers, Thermo-electrohydrodynamic convection in the thermally driven spherical shell with differential rotation, *PAMM*, **vol. 24, no. 1**, p. e202300036, 2023, doi: 10.1002/pamm.202300036.

6. P. S. B. Szabo, Y. Gaillard, F. Zaussinger, and C. Egbers, Thermo-electrohydrodynamic convection in a differentially heated shell with electric central force field, *PAMM*, **vol. 23, no. 1**, p. e202200121, 2023, doi: 10.1002/pamm.202200121.

Conference presentations

1. Y. Gaillard, P. S. B. Szabo, and C. Egbers, Dielectrophoretic-driven convection in the spherical shell experiment AtmoFlow, abstract accepted for *EFDC2*, Aug. 2629, 2025

2. Y. Gaillard, P. S. B. Szabo, and C. Egbers, Dielectrophoretic-driven convection in spherical Taylor-Couette flow, abstract accepted for *ICTW2025*, Jul. 1416, 2025

3. Y. Gaillard, P. S. B. Szabo, and C. Egbers, Dielectrophoretic-driven convection in the spherical shell, abstract accepted for *ICTW2025*, Jul. 1416, 2025

4. Y. Gaillard, P. S. B. Szabo, and C. Egbers, Convective regimes in differential spherical shell rotation with electric central force field, presented at *AGU2024*, Dec. 13, 2024

5. Y. Gaillard, P. S. B. Szabo, and C. Egbers, AtmoFlow: Convective regimes in differential spherical shell rotation with electric central force field, presented at the *EFDC1*, Sep. 17, 2024

6. Y. Gaillard, P. S. B. Szabo, and C. Egbers, Convective regimes of planetary atmospheres in the AtmoFlow spherical shell experiment: Solid-body and differential rotation, presented at the *ELGRA2024*, Sep. 04, 2024

7. Y. Gaillard, P. S. B. Szabo, and C. Egbers, Convective regimes in differential spherical shell rotation with electric central force field, presented at the *IUTAM2024*, Sep. 03, 2024

8. Y. Gaillard, P. S. B. Szabo, and C. Egbers, Exploring Thermo-Electrohydrodynamic Flows with Differential Rotation in AtmoFlow, presented at the *EGU24*, Mar. 07, 2024. doi: 10.5194/egusphere-egu24-3509.

9. Y. Gaillard, P. S. B. Szabo, and C. Egbers, Thermo-electrohydrodynamic convection in differentially rotating spherical shell, presented at the *GAMM2023*, May 31, 2023.

10. Y. Gaillard, P. S. B. Szabo, and C. Egbers, AtmoFlow: Thermo-electrohydrodynamic convection in the thermally driven spherical shell with differential rotation, presented at the *EGU23*, Feb. 22, 2023. doi: 10.5194/egusphere-egu23-1841.

11. Y. Gaillard, P. Haun, P. S. B. Szabo, Y. Sliavin, and C. Egbers, Numerical investigation of cell formation in a 2-dimensional differentially heated shell utilizing thermo-electrohydrodynamics, presented at the *EGU22*, Mar. 25, 2022. doi: 10.5194/egusphere-egu22-1687.

1 Introduction

Fluids, in principle, experience density variation due to temperature changes. This density variation results in a body force on the fluid due to gravity, known as buoyancy. Convection occurs when these forces overcome the fluid's viscosity, resulting in the so-called natural convection.

Convection can be initiated by applying an electric field in a temperature-varying environment. Thermo-Electrohydrodynamic (TEHD) convection studies the behaviour of a differentially heated fluid under the influence of an electric field. Similarly to density, the permittivity of matter changes with temperature. An uneven distribution of permittivity in a fluid under an electric field behaves similarly to natural convection, causing electric-driven convection. Adjusting the electric potential allows control of the amount of forcing from the electrical field.
Brandenburg University of Technology (BTU) conducted GeoFlow I and GeoFlow II experiments to study Earth's mantle and core convection. The experiments involved using two concentric, differentially heated spheres with an applied electric potential to create a radially oriented electric field, which mimicked a planet's gravitational force and triggered convection in the direction of the electric field.
Both experiments were conducted on the International Space Station (ISS). The research focused on TEHD-triggered convection, excluding natural convection, which requires microgravity conditions on the ISS. Additionally, the concentric shells rotate on a turning table, such that both spheres rotate simultaneously, which is known as solid-body rotation. This applied centrifugal and Coriolis forces on the system similar to a planet.

The AtmoFlow experiment, GeoFlow's legacy, brings similar capabilities. It uses an electric field to induce a radial force on the fluid, with expanded parameters for the electric potential and rotation compared to the GeoFlow experiment. The AtmoFlow experiment is conducted on a rotating table, as visible in Figure 1.1(a) to investigate solid-body rotation, and the inner shell is placed on an independently rotating shaft (see

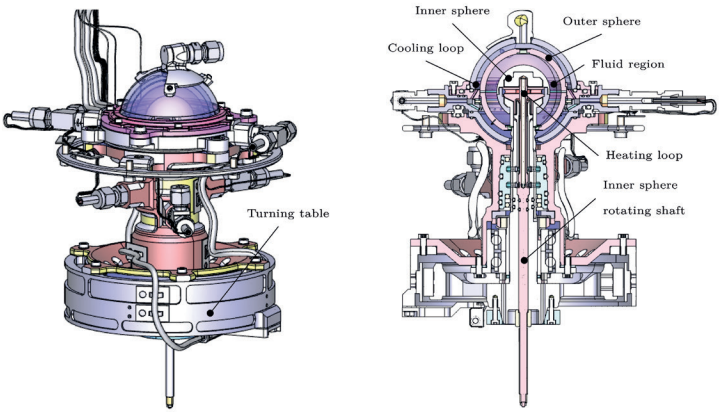

(a) (b)

Figure 1.1.: CAD model of the flight model for the ISS operation of the AtmoFlow experiment in (a) isometric and (b) side cut view, designed and built by Airbus Defense and Space(figures provided by Airbus, funding from DLR via BMWK grant No. 50WP2209).

Figure 1.1(b)), enabling the study of both differential rotation and TEHD convective flows.

The thermal convection pattern is analysed using Wollaston-Schlieren-Interferometry (WSI) [1], where a laser beam is directed through the fluid region and reflected on the inner shell of the experiment. Variations in temperature cause differences in the refractive index along the beam, leading to interference patterns [2] that are captured using a visual recording device. This data is then used to deduce convective patterns in the field.

The method is preferred over other methods like Particle Image Velocimetry (PIV) because of the ISS's strict safety requirements. The particles in the fluid necessary for PIV can alter dielectric fluid properties, leading to voltage breakthrough, potential experiment damage, fire, or toxic fumes.

Composition of the fluid cell

The fluid cell in Figure 1.2 consists of several parts to fulfil the experiment's demands. A steel sphere is positioned in the centre and heated using a heating loop in the equatorial region, applying a temperature gap ΔT to the reference temperature T_0. The steel guarantees good heat conduction from the loop and reflects the laser beam, which is necessary for the WSI. Next is the fluid gap region, also the Region of Interest (RoI). A glass sphere seals the gap, allowing the laser beam to pass through. The top and bottom of the glass sphere are milled to create space for copper inserts. The fluid is continuously pumped around the first glass sphere at the reference temperature. Because copper has higher thermal conductivity, the Poles appear colder to the fluid in the RoI than the glass sphere. A second glass sphere encapsulates this cooling loop. This experiment's heterogeneous temperature boundary condition intends to trigger flow patterns in combination with the differential rotation.

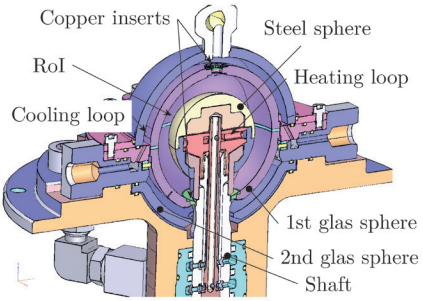

Figure 1.2.: Schematics of the AtmoFlow experiment's fluid cell (figure provided by Airbus, funding from DLR via BMWK grant No. 50WP2209).

The entire setup, including the interferometry system, is placed on a turntable (see Figure 1.1(a)), which is designed to rotate up to 2 Hz. Hence, the experiment occurs in a rotating reference frame. Differential rotation is acquired by turning the inner steel sphere, which is placed on the shaft, up to 2 Hz.
An electric field sets in the gap region. This is achieved using an alternating current source with frequency $f = 1 \cdot 10^4$ Hz connected to the experiment shells. The potential reaches up to 10 kV. Because the inner sphere is made of steel, it is electrically conductive and best suited for building an electric potential on the fluid. However, the sink for the potential, the first glass sphere, is made of glass and hence not electrically conductive. Therefore, a conductive coating is necessary to ensure the sustainability of the electric

Table 1.1.: Geometries and boundaries capabilities of the AtmoFlow experiment

Property	Symbol	Value
Inner radius of RoI (steel sphere)	R_1	18.9 mm
Outer radius of RoI (1st glass sphere)	R_2	27.0 mm
Reference temperature	T_0	293 K
Temperature gap range	ΔT	0-20 K
Steel sphere speed range	Ω_1	$0 - 2$ Hz
Turntable rotation speed range	Ω_2	$0 - 2$ Hz
Electric potential range	V	± 10 kV
Voltage frequency range	f	10 kHz

field. The AtmoFlow's fluid cell geometries and boundary capabilities are summarised in Table 1.1.

1.1 Motivation

The investigation of rotating fluids has a long history. Understanding the physics behind the flow opens new applications for engineering, geophysics, and astrophysics. The pioneer experiment started with the rotation of cylindrical geometries, resulting in Taylor-Couette (TC) flows [3]. The setup consists of two concentric cylinders with a fluid in between. The nature of this setup remains stable until a threshold, and can be described analytically for the stable regime. A cylinder's stable creeping flow depends only on the radial component. Beyond stability, the flow is three-dimensional and needs additional analysis methods. This stability persists due to the evenly distributed angular momentum along the rotating cylinder until the Taylor vortex establishes a new stability level.

The spherical Taylor-Couette (sTC) flow is always three-dimensional due to the curvature of concentric spherical shells, which results in different levels of angular momentum along the meridional component. This imbalance leads to a primary flow in the radial direction in the equatorial region and a secondary flow in the meridional direction that separates at the inner or outer shell to conserve continuity. The choice of rotation speed, whether the inner shell rotates faster or slower than the outer one, can result in different flow configurations, ranging from steady-state flow to transient periodic or turbulent flow.
In spherical TEHD convection, the force vector is mainly in the radial direction and remains stable initially. However, it destabilises after reaching the onset, resembling natural convection. A transient solution sets in by further increasing the force from the

electric field on the fluid. This becomes even turbulent by further increasing it.

The AtmoFlow experiment investigates the combined effects of these mechanisms on flow stability. The campaign focuses on the impact of TEHD convection on the stability of a co-rotating sTC, transitioning from stable parameters to periodic transient and irregular flow. This helps to determine the destabilising or stabilising effect of TEHD convection on sTC.

1.2 Aims and objectives

This thesis investigates the effect of TEHD convection in a spherical gap. The study extends this investigation by independently rotating the shell, creating differential rotation. The aim is to analyse the impact of this combined forcing. The various forces and their interactions result in different flow patterns, profiles, and magnitudes. These variations simultaneously lead to varying levels of heat flux, which depend on the concurrent flow patterns. Based on these findings, the intention is to classify the regimes using diagrams.
The method of information extraction in the ISS experiment is the WSI, which is limited to a temperature gradient. When resolving the interference fringes in time, a velocity deduction is possible. However, this requires an existing thermal convection pattern in the RoI. Tracing it over time provides a rough indication of velocity. Steady-state regimes do not have a moving pattern in the interferogram and, therefore, cannot return velocity information. Retrieving heat flux information from the experiment is also limited. An estimation is possible using the thermal differences in the experiment's heating or cooling loops. However, this returns an integral value but cannot return local phenomena. The aim is to obtain more detailed information regarding velocity and heat transport in the overall gap width.

This work conducts an investigation using Computational Fluid Dynamics (CFD), providing detailed results and refining the parameter space for the ISS onboard experiment. The OpenFOAM engineering toolbox is well-suited since it allows simple implementation of custom equations and post-processing routines.
The experiment built by Airbus is a setup with numerous parts, as shown in Figure 1.1. The boundary condition of the temperature of the fluid spreads through conduction from the heating and cooling loop. Therefore, the boundary condition on the fluid is a Neumann boundary condition, requiring a simulation that includes the solid part around the fluid region. The OpenFOAM CFD software allows this so-called multi-

region simulation. However, the additional complexity makes it much more challenging to interpret the result and associate a specific regime with a given temperature gap or set electric potential.
Current work processes an idealised model with Dirichlet temperature boundary conditions that link the dimensionless numbers directly to a resulting regime. This model simplifies the origin of the resulting flow patterns and heat flux, allowing for a more accurate analysis of the kinetic energy and its correlation with the heat flux. It also explores the transition from stable to transient and irregular flows. The investigation does not account for the influence of centrifugal buoyancy or dielectric heating, which restricts the number of parameters and provides a more accurate conclusion regarding the origin of the flow state, the resulting heat flux, and flow patterns.
The equations in this work are solved dimensionless, and the forcing parameters are lumped into dimensionless parameters. In a numerical model, the range for those dimensional parameters is endless. However, this investigation stays within the experiment's capabilities. The fluid in use boils at high temperatures and also has a breakdown voltage. Hence, the temperature and voltage parameters lumped in the dimensionless numbers must fulfil AmtoFlow's capabilities seen in Table 1.1.
The parameters for sTC range from viscous to periodic transient cases. The maximum rotation rate is determined when the flow from TEHD convection becomes marginal compared to the induced convection from rotation. This initial step provides preliminary parameters of interest for the upcoming AtmoFlow campaign on the ISS. Since the parameters for the ISS experiments are limited, this work simultaneously offers a priority classification for the onboard experiment.
To summarise, the focus of retrieved information is therefore set to:

- Resulting temperature and velocity profile for qualitative pattern analysis
- Quantitative analysis of heat flux from inner to outer shell
- Investigation about conductive and convective heat and the associated kinetic energy
- Propose a resulting regime diagram based on the competing pattern from sTC flow and the TEHD convection

1.3 Outline

The thesis is structured in nine chapters. An appendix provides further details about derivation and verification. After the introduction, the following sections are written:

- **Fundamentals and theory**: This section details the governing equations necessary to understand the modelling employed. It also explains the procedure for obtaining dimensionless equations and the resulting dimensionless numbers, representing the forcing parameters for the computed cases.

- **The current state of research**: The past research about TEHD convection and differential rotation is summarised in the named section. Each forcing and resulting flow of the literature is chronologically named, and the quintessence of each paper is briefly stated.

- **Computational and numerical modelling**: This chapter outlines transitioning from the physical experiment to the numerical model. It provides a detailed description of the simplified geometry and boundary conditions. Additionally, it includes information about the choice of solver and its settings, as well as evidence supporting mesh independence. Furthermore, due to limited computational time and the need to save only a reasonable amount of data, the capabilities of the AtmoFlow parameters must be selected. The methods used for selecting the processed parameters are explained. Finally, the chapter outlines the diagnostics necessary to achieve the aims previously mentioned.

- **TEHD convection in spherical shell**: Before stepping into the combination of differential rotation and TEHD convection flows, this section investigates the basic state of TEHD convection simulation with isothermal boundary conditions. The results presented are an extension of the existing GeoFlow experiments, and the differences from the current work are discussed.

- **Non-isothermal spherical Taylor-Couette flow**: Analogously, the differential rotation flow is investigated. The blend from steady-state to transient simulations of the selected parameter is shown and discussed for these simulations. This section, in particular, highlights the non-linear behaviour of differential rotation, which makes scalability challenging. Furthermore, the impact of the chosen aspect ratio on the margin of transient cases is shown.

- **TEHD convection in spherical Taylor-Couette flow with meridional isothermal boundary conditions**: After analysing the forcing independently, this chapter investigates the results by combining TEHD convection with differential rotation in a spherical system. The temperature boundaries remain isothermal for the processed case, and the new resulting patterns are compared to the isolated forcing from the prior chapter. Ultimately, a regime diagram is proposed.

- **TEHD convection in spherical Taylor-Couette flow with experiment-like thermal boundary conditions**: This chapter changes the isothermal temperature boundary condition to more experiment-like boundary conditions from the AtmoFlow experiment. The results are processed similarly to prior outcomes, compared and discussed.
- **Conclusion and outlook**: The last chapter summarises the knowledge gained from this thesis and proposes an outlook for future work.

2 Fundamentals and theory

This chapter introduces the fundamentals and theory of the governing equations to solve sTC flows and TEHD convection. It begins with the equations related to electric fields and the resulting force on fluids, followed by a description of the continuity and motion equations. The section then covers the transport of heat and concludes with the process of non-dimensionalising these equations.

2.1 Fluids under electric fields

The current section introduces the resulting force and heat generation from an electric field on a fluid. The focus is on dielectric fluids, and the sections explain the Kortweg-Helmholtz force density to a dielectric fluid and simplify Maxwell's equations.

2.1.1 Fluid properties

The effect of an electric field on a given fluid depends significantly on the molecular structure and charge of the fluid's composition. Fluids with free charges, like ions, see them moving within the fluid, generating an electric current. For a direct current (DC) source, those ions deposit on the cathode or the anode, depending on their charge. The moving charges between the ions cause ohmic heat, and if the current becomes significant, electromagnetism also needs to be considered [4]. An alternating current (AC) source with a high enough frequency can maintain those free charges in place, as

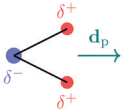

Figure 2.1.: Schematic of a polar molecule and its dipole $\mathbf{d}_\mathrm{p}$.

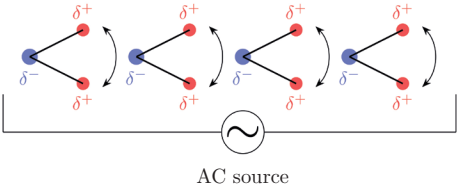

Figure 2.2.: Schematic of the source of dielectric heating from a high-frequency AC source on polar molecules.

their acceleration is not strong enough to follow the change of direction of the electrical field.

Dielectric fluids do not have free-moving charges by definition, but they can be polar. In the presence of an electric field, they orient according to the direction of the electric field and their dipole $\mathbf{d}_\mathrm{p}$ as schematically shown in Figure 2.1.

For the DC source, the molecules remain stationary. The non-polar module sees its dipole shift according to the source but remains stationary. Suppose an AC source is applied to a dielectric fluid composed of polar molecules, schematically shown in Figure 2.2. The molecules oscillate according to the source frequency. If the frequency becomes high enough, the friction on the molecular level becomes significant enough to generate measurable heat. This phenomenon is called dielectric heating.

2.1.2 Force resulting from an electric field on a dielectric fluid

The electric field $\mathbf{E}$ resulting in a force on a dielectric fluid is derived by the Kortweg-Helmholtz force density $\mathbf{f_E}$ described by Landau and Lifshitz [5] and written as

$$\mathbf{f_E} = \rho_\mathrm{e}\mathbf{E} + \boldsymbol{\nabla}\left[\rho\left(\frac{\partial\epsilon}{\partial\rho}\right)_T \frac{\mathbf{E}^2}{2}\right] - \frac{1}{2}\mathbf{E}^2\boldsymbol{\nabla}\epsilon \tag{2.1}$$

where ρ_e is the electric charge density, ϵ the permittivity and ρ the density. $\boldsymbol{\nabla}$ describes the nabla operator.

The first term

$$\mathbf{f}_\mathrm{EP} = \rho_\mathrm{e}\mathbf{E} \tag{2.2}$$

in the eq. (2.1) represents the electrophoretic (EP) force, which arises from the interaction of the moving free charges in the fluid within the electric field $\mathbf{E}$. This force is significant in cases where static or low-frequency electric fields are being studied. The

EP force becomes negligible when the frequency f is much greater than the charge relaxation rate τ_{e}^{-1}, where τ_{e} is defined as $\epsilon/\sigma_{\mathrm{e}}$ and σ_{e} represents the electric conductivity of the dielectric fluid in use. This study focuses explicitly on dielectric fluids with negligible conductivity, which aligns with previous works cited in references [6, 7, 8].

Moreover, when the frequency of the electric field changes rapidly enough, the fluid cannot respond effectively to it. In this situation, the frequency f surpasses several relaxation times like the viscous dissipation τ_{ν}^{-1}. Besides, there is the thermal dissipation time τ_{κ}^{-1} and the timescale τ_{m}^{-1}, τ_{D}^{-1} representing the charge migration, and diffusion processes, respectively as defined in [9]

$$f \ll \tau_{\mathrm{e}}^{-1}, \tau_{\nu}^{-1}, \tau_{\kappa}^{-1}, \tau_{\mathrm{m}}^{-1}, \tau_{D}^{-1}. \tag{2.3}$$

Additionally, the absence of current in the fluid eliminates any contributions from electrically induced magnetic fields.

The second term,

$$\mathbf{f}_{\mathrm{ES}} = \boldsymbol{\nabla}\left[\rho\left(\frac{\partial\epsilon}{\partial\rho}\right)_{T}\frac{\mathbf{E}^2}{2}\right] \tag{2.4}$$

describes the electrostrictive (ES) force. This term represents the force induced by the electric field on the fluid due to the non-proportional change of permittivity to a change in density. This term has a static contribution to the fluid in an incompressible closed environment. It is often combined with the pressure term [9].

The remaining term

$$\mathbf{f}_{\mathrm{DEP}} = -\frac{1}{2}\mathbf{E}^2\boldsymbol{\nabla}\epsilon \tag{2.5}$$

in the equation is the dielectrophoretic (DEP) force, which describes the force on a fluid under an electric field due to changes in permittivity. Since permittivity changes with temperature, the force is related to the electric field and temperature variations.

Analogous to buoyancy problems, the permittivity can be described using the Electrohydrodynamic (EHD) Bousinessq approximation [6, 10, 11], which is valid for small temperature changes

$$\epsilon(T) = \epsilon_0\epsilon_{\mathrm{r}}\left[1 - e\left(T - T_0\right)\right], \tag{2.6}$$

where ϵ_0 represent the vacuum permittivity and ϵ_{r} the relative permittivity at the reference temperature T_0. The thermal expansion coefficient of the permittivity is defined

as e. This method were aplied by numerous previous works before [12, 13, 14].

In a quasistatic electric field, Maxwell's equations reduce to

$$\boldsymbol{\nabla} \times \mathbf{E} = \quad 0 \tag{2.7}$$

$$\boldsymbol{\nabla} \cdot [\epsilon\,(T)\,\mathbf{E}] = \quad 0 \quad , \quad \text{with} \quad \mathbf{E} = -\boldsymbol{\nabla}\phi \tag{2.8}$$

where ϕ is the electric potential[15]. The rotation of a scalar's gradient in eq. (2.8) remains zero by definition, implying no electric field rotation over time. The Gauss eq. (2.8) couples the electric field with the temperature-sensitive permittivity in the field.

The Debye length λ_{D} characterises the diffusion layer, which is the electrically charged outer region of the electric double layer formed at the interface between a fluid and an electrode. Using the condition from eq. (2.3) and the Debye length condition [6]

$$\lambda_{\mathrm{D}} \ll d \tag{2.9}$$

satisfies the quasi-static approach of Maxwell's equations. This approach has also been used in references [16, 17].

The electric potential ϕ is subjected to boundary conditions; it is connected to an alternating current source with a voltage defined as $V(t) = \sqrt{2}V_0 \sin(2\pi f t)$. As a result, the alternating peak voltage over time at the boundary results in an effective voltage V_0 derived from the voltage's root mean square over a period.

The EHD Bousinessq approximation from eq. (2.6) for the permittivity also applies to the Gauss eq. (2.8), resulting in

$$\boldsymbol{\nabla} \cdot [(1 - e(T - T_0))\,\mathbf{E}] = 0. \tag{2.10}$$

The approximation is necessary for making the equations later dimensionless.

2.2 Continuity equation

For a given volume, the mass flow entering a control volume needs to equal the mass flowing out of it [18]. In an Eulerian reference frame, a fixed control volume is considered, and the mass m is processed via

$$m = \int_V \rho \, \mathrm{d}V. \tag{2.11}$$

The change rate over time t of the mass through the face area A for the given control volume is calculated using

$$\partial_t m = \oint_A \rho \mathbf{u} \cdot \mathbf{n} \, \mathrm{d}A \tag{2.12}$$

where $\mathbf{n}$ is the normal vector to the surface A.
Adding the current mass of the control volume from eq. (2.11) to the change rate of eq. (2.12) results in

$$\partial_t m = \partial_t \int_V \rho \, \mathrm{d}V + \oint_A \rho \mathbf{u} \cdot \mathbf{n} \, \mathrm{d}A. \tag{2.13}$$

By applying the divergence theorem (also known as Gauss's theorem) to eq. (2.13) leads to the volume integral

$$\partial_t m = \int_V \left(\partial_t \rho + \boldsymbol{\nabla} \cdot (\rho \mathbf{u}) \right) \, \mathrm{d}V \tag{2.14}$$

Considering now an intifisimal control volume for eq. (2.14) simplifies to

$$\partial_t \rho + \boldsymbol{\nabla} \cdot \rho \mathbf{u} = 0. \tag{2.15}$$

The flow is incompressible for the current work, and the density ρ becomes a constant. The continuity equation, hence, is simplified as follows

$$\boldsymbol{\nabla} \cdot \mathbf{u} = 0 \tag{2.16}$$

and is now density and time independent.

2.3 The equations of motion

The current section provides an overview of the various equations and terms found in the momentum equations. These are essential for describing the forcing on the fluid and the conservation and resulting momentum.

2.3.1 The material derivative

The material derivative is the fundamental concept used to describe the change of a specific quantity in fluid dynamics. It explains the rate of change of a given quantity within an Eulerian frame in the x, y, and z directions over time t [18]

$$\frac{D}{Dt} = \frac{\partial}{\partial t} + u_x \frac{\partial}{\partial x} + u_y \frac{\partial}{\partial y} + u_z \frac{\partial}{\partial z}. \tag{2.17}$$

When applying the material derivative to the velocity $\mathbf{u} = (u_x, u_y, u_z)^T$, the description of the rate of change of velocity for all three directions, which also represents the fluid's

acceleration in the control volume is obtained. Defining the material derivative of $\mathbf{u}$ for an incompressible fluid cell with constant density ρ_0 leads to the definition of the advection term $\rho_0 \left(\partial_t \mathbf{u} + (\mathbf{u} \cdot \boldsymbol{\nabla})\mathbf{u}\right)$.

2.3.2 Surface forces

The forces presented apply directly to the boundaries of the infinitesimal control volume, known as surface forces. Force densities are then deduced and applied to the control volume.

Pressure force on a control volume

For a control volume, the pressure, p, exerts a force on the volume's surfaces. These surface forces can be represented by a surface integral over the boundary of the control volume [19]. By applying the divergence theorem, the surface integral is converted into a volume integral

$$-\oint_A p \, \mathrm{d}A = -\int_V \boldsymbol{\nabla} p \, \mathrm{d}V. \tag{2.18}$$

This equation shows that the force density from pressure on the boundary is equivalent to the volume integral of the pressure gradient. Hence, the force per unit volume due to pressure is

$$\mathbf{f}_p = -\boldsymbol{\nabla} p. \tag{2.19}$$

Viscous stress

Viscous stress arises from the shearing motion between adjacent fluid molecules due to velocity differences. In the context of infinitesimal control volumes, this shearing is represented by the rate of velocity change (velocity gradient) across the cell boundaries. The viscous stress is proportional to this velocity gradient, multiplied by the fluid's dynamic viscosity μ.
The viscous stress tensor $\boldsymbol{\tau}_{ij}$, expressed in Einstein notation, is defined

$$\boldsymbol{\tau}_{ij} = \mu \left(\frac{\partial u_i}{\partial x_j} + \frac{\partial u_j}{\partial x_i} \right). \tag{2.20}$$

where u_i and u_j are the components of the velocity vector in the i- and j-directions, respectively, and x_i and x_j are spatial coordinates. This equation describes the relationship between the velocity gradients and the viscous stresses in the fluid, with the

dynamic viscosity scaling the magnitude of the stress response from shearing from material properties.
The integral of the normal stress tensor component to the control volume's faces gives the shear force resulting from viscous stress on the surface. Similarly, the Gaussian integration law is used to calculate a volumetric integral.

$$\oint_A \boldsymbol{\tau} \cdot \mathbf{n} \, \mathrm{d}A = \int_V \boldsymbol{\nabla} \cdot \boldsymbol{\tau} \, \mathrm{d}V = \mu \int_V \boldsymbol{\nabla} \cdot \left(\boldsymbol{\nabla}\mathbf{u} + (\boldsymbol{\nabla}\mathbf{u})^T \right) \, \mathrm{d}V. \tag{2.21}$$

For incompressible flows, where the divergence of the velocity field is zero $\boldsymbol{\nabla} \cdot \mathbf{u} = 0$ (see. eq. (2.16)), the part $\boldsymbol{\nabla} \cdot (\boldsymbol{\nabla}\mathbf{u})^T$ vanishes. Thus, the surface integral simplifies to:

$$\int_V \boldsymbol{\nabla} \cdot \boldsymbol{\tau} \, \mathrm{d}V = \mu \int_V \boldsymbol{\nabla}^2 \mathbf{u} \, \mathrm{d}V. \tag{2.22}$$

On the control volume, the force density from viscous stress results in

$$\mathbf{f}_\tau = \mu \boldsymbol{\nabla}^2 \mathbf{u}. \tag{2.23}$$

The simplifications of the tensor apply to Newtonian fluid, where the stress scales in an isotropic manner over the shear rate.

2.3.3 Body forces

Body forces act on a fluid volume. Section 2.1 showed already the force densities resulting from an electric field on a fluid. The electrophoretic force $\mathbf{f}_{\mathrm{EP}}$ is neglected. The electrostrictive force density $\mathbf{f}_{\mathrm{ES}}$ adds a static contribution and is lumped into the pressure term [10], such as

$$P = p + \rho \left(\frac{\partial \epsilon}{\partial \rho} \right)_T \frac{\mathbf{E}^2}{2} \tag{2.24}$$

Finally, the DEP force $\mathbf{f}_{\mathrm{DEP}}$ from eq. (2.5) adds a dynamic contribution to the momentum equation. Applying the simplification seen in section 2.1, the dielectrophoretic force is simplified to

$$\mathbf{f}_{\mathrm{DEP}} = \frac{\epsilon_0 \epsilon_{\mathrm{r}} e}{2} \left(\boldsymbol{\nabla}\phi \right)^2 \boldsymbol{\nabla} T. \tag{2.25}$$

The electric field is substituted by the gradient of electric potential ϕ.

Rotating flows can be described in two ways. The first approach involves defining a rotating boundary condition, where the boundary of the fluid domain moves with a prescribed rotational velocity. In this approach, the inertial reference frame is non-

rotating, and an external observer measures the motion from a stationary frame of reference. The fluid's rotation results purely from the boundary conditions, and no fictitious forces, such as Coriolis or centrifugal forces, are introduced directly into the momentum equations.
Alternatively, rotating flows can be solved in a rotating reference frame involving the rotation frame of reference along with the investigated model. Fictitious forces can be added to the momentum equations as body forces while the system's boundaries remain stationary.
The Coriolis force is defined as

$$\mathbf{f}_{\mathrm{Co}} = -2\rho_0\, \boldsymbol{\Omega} \times \mathbf{u} \tag{2.26}$$

and the centrifugal force as

$$\mathbf{f}_{\mathrm{Cf}} = -\rho_0\, \boldsymbol{\Omega} \times (\boldsymbol{\Omega} \times \mathbf{x}) \tag{2.27}$$

where $\boldsymbol{\Omega} = (\Omega_x, \Omega_y, \Omega_z)^T$ represent the sphere rotation vector and $\mathbf{x} = (x, y, z)^T$ is the spatial coordinate vector. In this thesis, the centrifugal force in eq. (2.27) is considered a static term and can be similar to the electrostrictive force lumped in the pressure term as centrifugal pressure [20]. However, when considering centrifugal buoyancy, colder fluid is displaced to the outer shell while hot fluid remains on the inner side of the gap due to rotation[1].

2.3.4 Combined momentum equations

Together, the named forces form the momentum equation. On the left side, the advection term describes the fluid motion subjected to the forcing terms of the right side: the pressure, viscous, and body forces from eq. (2.25), eq. (2.26) and eq. (2.27)

$$\partial_t \mathbf{u} + (\mathbf{u} \cdot \boldsymbol{\nabla})\mathbf{u} = -\frac{1}{\rho_0}\boldsymbol{\nabla} P + \nu \boldsymbol{\nabla}^2 \mathbf{u} + \frac{1}{\rho_0}\left(\mathbf{f}_{\mathrm{DEP}} + \mathbf{f}_{\mathrm{Co}} + \mathbf{f}_{\mathrm{Cf}}\right), \tag{2.28}$$

where ν is the kinematic viscosity.

2.4 Heat equation

For the definition of transport of heat in fluid the material derivative eq. (2.17) is applied on an energy related term like the enthalpy $h = c_{\mathrm{p}} T$ [21]. It is assumed in the current study that the temperature variations are small, allowing for the approximation

[1] The centrifugal buoyancy is not considered in this work. For consistency reasons of the upcoming used solver, it is kept in the momentum equations here, not lumped in the pressure term P.

of constant heat capacity c_p. This work considers only incompressible fluids, and mutual effects like kinetic effects, such as viscous shearing, are not considered due to their negligible magnitude. Consequently, the enthalpy transport simplifies to the transport of temperature through the fluid, expressed as: $\partial_t T + (\mathbf{u} \cdot \boldsymbol{\nabla})\, T$.

Besides the temperature transport term, matter diffuses heat via conduction. The heat diffusion is defined by Fourier's law $\kappa \boldsymbol{\nabla}^2 T$. Together, they form the temperature equation of the fluid

$$\partial_t T + (\mathbf{u} \cdot \boldsymbol{\nabla}) T = \kappa \boldsymbol{\nabla}^2 T, \tag{2.29}$$

using the thermal diffusivity κ.

2.5 Dimensionless equations

The equations above solve the fluid problem while maintaining the physical dimensions of the properties. However, solving fluid problems in a dimensionless form offers several advantages. It allows for a more general analysis, independent of specific scales, and enhances comparability with other studies that may use different parameters, fluids, or conditions. Despite these differences, the underlying physical behaviour can be compared through dimensionless variables and numbers. To achieve this, the equations are non-dimensionalised to express the variables without units, and the characteristic forcing terms are grouped into dimensionless numbers.

For this task, the following scaling is proposed: The gap width is defined as $d = R_2 - R_1$ and scales the space coordinates by having a unity length for the gap width. The Prandtl number investigated in this work is considered $\mathrm{Pr} > 1$. Therefore, momentum diffuses faster than heat, and hence time scale t uses the heat diffusivity κ such that its scaling results in $\tau = t^* = t\ \kappa/d^2$. Here, Ω_2 is set to the rotating reference around the z-axis. Hence, the vector is defined as the outer sphere rotation $\boldsymbol{\Omega} = (0, 0, \Omega_2)^T$, in the dimensionless approach, this reduces to the coordinate system vector $\mathbf{e}_z$. The temperature T is scaled using the boundary temperature gap in the system, which refers to the inner boundary to outer boundary temperature difference $\Delta T = T_1 - T_2$. Hence, the following non-dimensional variables can be obtained; these are denoted

$$\begin{aligned} \mathbf{u}^* = \mathbf{u}\frac{d}{\kappa}, \quad \tau = t^* = t\ \frac{\kappa}{d^2}, \quad \boldsymbol{\nabla}^* = d\boldsymbol{\nabla}, \quad P^* = P\frac{d^2}{\rho_0 \kappa^2}, \\ T^* = \frac{T - T_0}{\Delta T}, \quad \mathbf{E}^* = \mathbf{E}\frac{d}{V_0}, \quad \vartheta = \phi^* = \phi\frac{1}{V_0}, \quad \omega = \Omega^* = \Omega\frac{d^2}{\kappa} \end{aligned} \tag{2.30}$$

The equation scaling is merged into non-dimensional numbers, and simultaneously, the forcing parameters for the upcoming simulations are determined. Starting with the thermo-electric parameter

$$\gamma_e = e\Delta T \tag{2.31}$$

which quantifies the linkage between the thermal boundary condition and the permittivity change rate due to temperature variation.

The amount of forcing from the electric field and the temperature of the fluid originating from the dielectrophoretic force $\mathbf{f}_{\mathrm{DEP}}$ is expressed via the electric Rayleigh number

$$\mathrm{Ra}_{\mathrm{E}} = \frac{\epsilon_0 \epsilon_r \gamma_e V_0^2}{2\rho_0 \nu \kappa}. \tag{2.32}$$

The rotation rate from the rotation reference frame, which concerns the fictitious Coriolis and centrifugal force is expressed using the Taylor number defined as

$$\mathrm{Ta} = \frac{4\Omega_2^2 d^4}{\nu^2} \tag{2.33}$$

The amount of differential rotation is defined using the Rossby number

$$\mathrm{Ro} = \frac{\Omega_1 - \Omega_2}{\Omega_2}. \tag{2.34}$$

Note that this dimensionless number does not directly affect the equation as a force but is involved in defining the boundary condition.

Finally, the Prandtl number

$$\mathrm{Pr} = \frac{\nu}{\kappa} \tag{2.35}$$

defines the ratio of viscosity to thermal diffusivity. It is a material property and varies only according to the fluid selection in this consideration.

Applying the scaling eq. (2.30) to the governing eq. (2.16), eq. (2.28), eq. (2.29) results in the dimensionless TEHD equations

$$\boldsymbol{\nabla} \cdot \mathbf{u} = 0 \tag{2.36}$$

$$
\begin{aligned}
\partial_t \mathbf{u} + (\mathbf{u}\cdot\boldsymbol{\nabla})\mathbf{u} = &-\boldsymbol{\nabla} P + \mathrm{Pr}\,\boldsymbol{\nabla}^2\mathbf{u} \\
&- \mathrm{Pr}\sqrt{\mathrm{Ta}}\,\mathbf{e}_z \times \mathbf{u} \\
&- \frac{1}{4}\mathrm{Pr}^2\,\mathrm{Ta}\,\mathbf{e}_z \times (\mathbf{e}_z \times \mathbf{x}) \\
&- \mathrm{Pr}\,\mathrm{Ra}_\mathrm{E}|\mathbf{E}|^2\boldsymbol{\nabla} T
\end{aligned}
\tag{2.37}
$$

$$
\partial_t T + (\mathbf{u}\cdot\boldsymbol{\nabla})T = \boldsymbol{\nabla}^2 T \tag{2.38}
$$

$$
\boldsymbol{\nabla}\cdot[(1-\gamma_e T)\,\mathbf{E}] = 0, \quad \text{with} \quad \mathbf{E} = -\boldsymbol{\nabla}\vartheta. \tag{2.39}
$$

For readability reasons, the non-dimensioned variable does not have the indexed asterisk in the upcoming results. The boundary conditions associated with the set of equations are detailed in the following sections. First, the model formulation from the experiment is detailed, and then each chapter covers a different set of boundary conditions investigated.

3 Current state of research

This chapter provides an overview of previous research that is relevant to this thesis. The first section discusses experiments and numerical investigations related to buoyancy caused by gravity and the comparison of convection in an electric field. Next, it covers the physics and convection in rotating systems, with a specific focus on differential rotation.

3.1 Buoyant flows

Buoyancy is the force resulting from density changes due to temperature differences under gravity. The first section provides the research, giving detailed information on this topic. In contrast, the second section explains the analogy using a temperature-dependent change in permittivity under an electric field to investigate convection resulting from temperature variation under an electric field.

3.1.1 Natural convection

At the beginning of the 20th century, the effects of natural convection were explored in Bénard's publication [22]. In his experiment, he set up a shallow layer of liquid, which formed a regular structure when the plate beneath the fluid was heated. Two mechanisms transport the heat in this system. Heat transfer through a material due to thermal diffusion occurs in all states of matter: solid, liquid, or gas. Convection under gravity occurs when heating causes variations in fluid density, leading to motion. The velocity of this motion scales with the amount of heat input and the resulting buoyant force, and is opposed by the fluid's viscosity. This process is known as natural convection. For a horizontally heated plate, buoyancy must overcome viscous resistance for motion to occur [23]; the point at which this motion begins is referred to as the onset of convection. Lord Rayleigh, in his work, made an initial attempt to characterise the forming structure and classify them based on the acting forcing [24]. His name was later given to the dimensionless Rayleigh number Ra, which quantifies the amount of buoyancy over viscous and thermal diffusion. Busse et al. [25, 26] conducted a more detailed analysis

of the forming structures. Near the critical number, stationary structures begin to form. They are initially referred to as stationary rolls and characterise long upcoming and downstream flow structures. As the Rayleigh number increases, these rolls develop into zigzag instabilities. From now on, the rolls are no longer straight. Additionally, a further increase in the Rayleigh number leads to cross-roll instability and to the bi-modal hexahedron forming cells, which Bénard already observed. Busse proposed a non-linear approach for the Boussinesq equation to investigate these structures forming [27].

While the previously named work investigates plane cavities, natural convection can also be observed in spherical, differentially heated cavities. The first experiments were provided by Bishop et al. [28] and Scanlan et al. [29], in which the heat transfer and related temperature profiles were investigated. These works focused on the non-linear characteristics of natural convection in spherical shells compared to plate cavities. This non-linearity results from the sphere curvature and causes early convection for comparable smaller Rayleigh numbers. Also, the flow is highly Prandtl number dependent, as shown in the work by Nakagawa et al. and Travnikov et al. [30, 31].

For a more planet-like model, Chandrasekhar investigates the onset of self-gravitating inner heated spherical shells numerically [32, 33] for mantle convection. This was a pioneering step in the upcoming research for investigating geophysical convection. Busse made a similar numerical investigation about patterns coming from differential, heated spherical shells for self-gravitating systems [34]. The work revealed different stationary flow structures, and increasing buoyancy led to a new appearance in the mode shape. A mode is a recurrent pattern appearing periodically in the azimuthal direction of the sphere. Patterns up to mode six could be shown in this investigation of [34, 35].

3.1.2 Buoyant flow in TEHD convection

The force generated by an electric field acting on a fluid was first explored in the pioneering work of Senftleben and Braun [36, 37]. They enhanced heat flux by applying an electric force field to a gas in a differentially heated cylindrical cavity, which resulted in improved heat transport due to increased convection. Various power sources, including a DC source and a low-frequency AC source, were utilised for these experiments. This setup requires including all terms from eq. (2.1), as later described by Landau and Lifshitz [5].

TEHD convection in planar cavities

The work by Roberts [10] showed the use of the ES and DEP force for investigating buoyancy problems and the states of the analogy to natural convection. The study examines a thermally differentially heated cavity with an isolating fluid to prevent free-moving charges. The remaining forces from the electric field on the fluid are the ES and DEP forces. The temperature-dependent permittivity is modelled using the Boussinesq approximation (see eq. (2.6)), and the electric Rayleigh number was defined, similar to natural convection, as the amount of forcing from the electric field over the thermal dissipation and viscosity. A perturbation analysis determines the onset of the critical electric Rayleigh number. In this work, he stated the advantages of the DEP and ES forces for laboratory-scale Earth mantle convection experiments, as the force field can be investigated in the radial direction for spherical geometries.

Turnbull [16] also investigated a thermally differentially heated cavity. In this study, an AC source was selected at 60 Hz to prevent the movement of free charges, and the influence of gravity was included in the body forces. His published work, similar to Rayleigh's research, utilised the Boussinesq approximation (see eq. (2.6)) to account for changes in permittivity and density due to temperature variations. The critical electric Rayleigh number was defined using a perturbation analysis to indicate when convection begins. Additionally, Turnbull's work examined the resulting pattern wavelength from the interaction of natural convection and convection driven by the electric field. The work by Turnbull is later reproduced experimentally by Stiles [17], where various experiments are performed to verify the critical electric Rayleigh numbers. Moreover, additional considerations are made to differentiate between polar and non-polar fluids and their impact on the critical electric Rayleigh number.

Smoridin et al. [38, 39] investigate the effect of the frequency of the AC source in the rectangular cavity. The studies show that the DEP force in a high-frequency range no longer depends on the field's polarity and remains constant over time.

The Gauss equation in eq. (2.8) has the temperature-dependent permittivity. Due to temperature variation, the electric field becomes inhomogeneous. The work from Yoshikawa et al. [6] then demonstrated via linear stability analysis the influence of different thermo-electric parameters γ_e from the boundaries on the onset of convection in a microgravity environment.

Subsequently, Barry et al. [40] conducted a detailed investigation of three-dimensional TEHD convection in the planar cavity under microgravity conditions. The work revealed structures resembling Rayleigh-Bénard flows, highlighting the similarity to natural con-

vection and comparing the critical electric Rayleigh number to the findings of Yoshikawa et al.

TEHD convection in cylindrical annulus

The electric field in the cylindrical annulus is, besides the thermal variation, affected by the curvature of the annulus. The field lines are closer to each other at the inner radius, resulting in a stronger electrical field. This is shown and investigated by Yoshikawa et al. [41] in a supposed microgravity environment. Using linear stability analysis, the study shows the change in the critical electric Rayleigh number when the aspect ratio η changes. The aspect ratio is defined by the ratio of the radii detailed by

$$\eta = \frac{R_1}{R_2}. \tag{3.1}$$

Furthermore, the resulting mode of the convection cells increases with the rising aspect ratio.
Travnikov et al. [42] completed and confirmed Yoshikawa's work using DNS with the pseudospectral method. This study from Travnikov investigates the impact of the thermo-electric parameter γ_e on the critical Rayleigh number for various aspect ratios. With a rising temperature gap from the boundaries, the onset happens at a higher critical electric Rayleigh number, especially for aspect ratios larger than 0.7; this becomes significant.

The thermal variation affects the density. Applying rotation to the cylindrical annulus applies a more significant force to denser, colder fluid, pushing it towards the outer boundary. This is called centrifugal buoyancy. The DEP force pushes for an inner heated annulus, the hot fluid outwards. Therefore, both forces oppose each other. The study from Kang et al. [43] investigates both configurations. At first, the inner cylinder is heated, and then the outer one is heated. Depending on the dominant force and configuration, different flows are observed and categorised into circular Couette flow, axisymmetric and non-axisymmetric flow and oscillatory flows. A regime diagram shows the margin of each appearing flow.
Another study by Kang et al. [44] looks at the influence of the DEP force on rotation-induced convection. For the outer heated cylindrical annulus with small aspect ratios, the DEP force delays the convection induced by the rotation. The DEP enhanced the convection in annuli with a high aspect ratio.

For verifying the numerical investigation of TEHD convection in cylindrical annuli, Meyer et al. [45, 46] performed an experiment on a parabolic flight to reach microgravity conditions. This experiment is further developed, and the parameter space is extended in the work by Szabo et al. [47, 48], the flow pattern is post-processed using the PIV method. The onset of convection for selected critical Rayleigh numbers could be compared to the linear stability analysis performed previously. Kang et al. [49] performed numerical simulations adding the terrestrial gravity. The study shows the effect of gravity on the resulting pattern, which can be compared to the annulus experiment in a lab setup.
For an infinite inner heated cylindrical annulus, Szabo et al. [13] investigate the resulting mode number and the associated Nusselt number. An estimate is made for the rising DEP, causing the mode number to initially increase and then decrease again. The Nusselt number increases constantly with the rise of the electric Rayleigh number. Gaillard et al. [14] extended this investigation by incorporating the rotation of the cylinder, which introduces centrifugal buoyancy. The counterforcing of the outward-oriented DEP forcing and the inward-oriented force from centrifugal buoyancy resulted in different regimes classified by the resulting mode energy. The various spatial thermal mode energy levels significantly affected the resulting Nusselt number.

TEHD convection in spherical geometries

In a spherical system, the curvature causes the electric field lines to converge even more at the inner side of the gap than in the cylindrical annulus, resulting in a more substantial electric field magnitude at the inner side. In spherical gap geometries, making the electric field only radially dependent without any temperature variation is common. This enables solving the Gauss equation analytically before processing the numerical simulation. Mutabazi et al. [50] reviewed the TEHD convection in canonical geometries and showed the curvature's influence and the temperature boundary conditions on the onset of TEHD convection. The findings are that the onset of TEHD convection in spherical systems is more sensitive to the aspect ratio than the temperature variation from the boundary.

As Roberts already stated in [10], the radial force from the DEP can be used for investigating the radial force field in a laboratory setup. This method can study planetary flow involving buoyancy induced by gravity on a lab scale. The key difference is that the gravity by Newton's law decreases with $\sim r^2$, and the DEP force decreases with $\sim r^5$ [50].

The first experiment using this method to study planet convection was conducted by Hart et al. [51] in 1986 on the International Space Station (ISS). Since Earth's gravity exerts a force on differentially heated fluid, which could interfere with the DEP force and potentially skew the results, the experiment had to be carried out under microgravity conditions. Numerical simulation completed the experiment conducted on the ISS [52]. The work demonstrated that the DEP force in spherical geometries can trigger patterns similar to those present in terrestrial flow.

The GeoFlow experiment, conducted by the BTU, investigates Earth's mantle convection using the DEP force in a rotating spherical gap. Analogous to Hart's experiment, GeoFlow is processed on the ISS to have microgravity conditions [53]. Travnikov et al. processed the numerical simulation and showed the different resulting modes and patterns resulting from the interaction of the DEP force and the rotation of the spheres [54]. The bifurcation by Beltrame et al.[55] demonstrated the possible outcomes in the near-onset region and how different modes interact in the flow.
The work from Futterer et al. [56, 57] processed numerically for idealised boundary conditions the convection patterns from the GeoFlow experiment. The studies identified the different flow types as axisymmetric steady-state, transient or irregular flow and categorised them in a regime diagram. The various emerging modes are also identified, and the numerical results are compared to those from the ISS onboard experiment.
A second experiment from BTU, named GeoFlowII, is performed on the ISS, which adds a viscosity-varying flow to investigate mantle convection done by Futterer et al. [58]. Numerically, Futterer et al. [59] investigated those flows and showed the transition from plume pattern to sheet pattern by increasing the electric Rayleigh number.

3.2 Fluids subjected to solid-body rotation

Fluid rotating around an axis experiences various forces. First, the fluid undergoes a centrifugal force due to the change in trajectory. Second, the Coriolis force deflects the path of an object moving within the frame, causing it to curve. The rotation of fluids in a rotating system can be described in two primary principles.
The system's boundaries create a rotating gap that induces rotation in the fluid using non-slip boundary conditions in a global reference frame. The change in trajectory occurs due to momentum exchange within the contained fluid. Another approach involves placing the contained fluid in a rotating frame, where the boundaries remain immobile, but the centrifugal and Coriolis forces are applied. When both shells rotate with the same angular velocity, they rotate in a solid-body manner. These cases remain in a

stable state for incompressible and thermally homogeneous descriptions. Chandrasekhar investigated instabilities in spherical systems by heating the inner sphere and rotating the system [60, 61]. In this work, the convection is driven by centrifugal buoyancy resulting from thermal-induced density changes under rotation.
Robert's work [62] defined the behaviour of fluid rotating and the resulting convection asymptotically by applying the linear theory by Chandrasekhar [63], where it could return an analytic result for the velocities. For small Prandtl numbers, Robert's work demonstrated that the fluid behaves in an asymptotic steady state of convection for high Taylor numbers. Later work by Roberts [64] completes that the primary convection occurs in a supposed cylinder between the shells.
Further investigating Roberts's work, Busse [65, 66] approximated the self-gravitating sphere to investigate radial oriented buoyancy by a highly rotating sphere. Note that the gravitation vector in this setup does not point in the radial direction of the spherical coordinate system but is colinear to the centrifugal force vector. This method is sufficiently accurate for high-rotating flow around the Equator. In these works, the relevance of centrifugal buoyancy for high-rotating systems is emphasised, and a defined application for Earth's convection systems is described by explaining the appearance of Rossby waves and the columnar vortices arranged in a cylindrical shape. The resulting patterns are afterwards reproduced in a laboratory experiment by Busse and Carrigan [67, 68].

Previously, the gravitation for the rotating system was simplified to a point in the centrifugal direction. These approximations for planetary systems are valid for high rotation rates. Numerical experiments by Gastine et al. [69] showed the transition from non-rotating to rotating convection under a radial-oriented buoyancy. The work by Gastine et al. shows, depending on the rotation rate, how much buoyancy from gravity is necessary to reach the onset or vice versa to reach a high rotation-dominant regime. Despite this investigation proposing an extensive range of regimes for defining the dominant force, it did not consider the stabilising effect of centrifugal buoyancy [70] and concentrated uniquely on the impact of the Coriolis force and natural convection. In opposition, the work by Potherat et al. [71] reviews the experiments conducted over the past seven decades and explicitly states not to neglect centrifugal buoyancy too quickly, as it significantly contributes to high-rotating systems.

3.3 Fluids subjected to differential rotation

Differential rotation, also known as TC flow in cylindrical geometries, refers to the phenomenon where concentric cylinders rotate at different speeds. This applies to both

the inner and outer shells. Although this application has many possible geometries, this section focuses on differential rotation in cylindrical and spherical configurations.

3.3.1 Cylindrical Taylor-Couette flow

In the context of cylindrical geometries, Lord Rayleigh established the stability criteria [72], indicating potential instability when the momentum of the inner shell L_1 exceeds that of the outer shell L_2. The angular momentum of a cylindrical shell is expressed as

$$L = \omega r^2 \tag{3.2}$$

where ω is the angular velocity and r the radius. Equilibrium is attained when $L_1 = L_2$ or $\omega_1 = \omega_2 \eta^{-2}$.

The work by Taylor[3] processed the rolls, resulting in differentially rotating cylinders, which later earned it the name Taylor vortices. The work employed a stream function to analyse the instability and subsequently verified the findings in an experimental setup.

The work by Eckhardt et al. [74, 75, 76] investigates the dissipation rate and momentum flux occurring in TC flows. A custom-defined Nusselt number, defined by angular momentum flux, helps establish scaling laws for the resulting torque resulting from the differential flow.

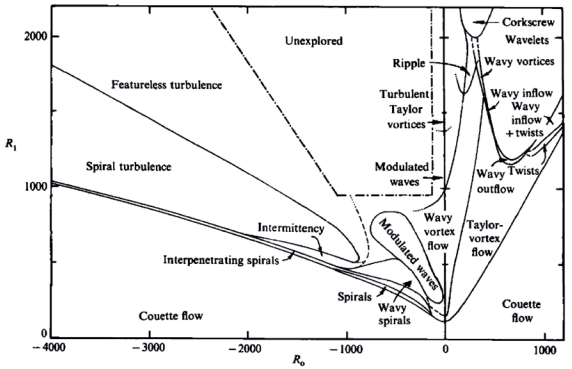

Figure 3.1.: Regime classification for TC flows, reproduced from Andereck et al. [73], with the permission of Cambridge University Press.

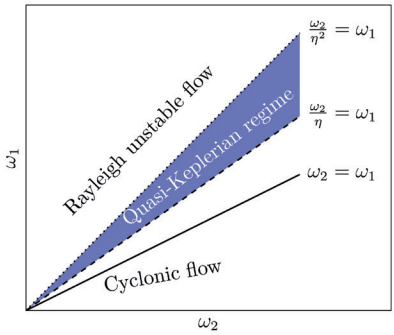

Figure 3.2.: Regimes classification in TC in cylindrical geometry with Rayleigh stability line (·····), rotation line (- - -) and solid body line (——).

The resulting flows in TC reach a vastly different regime, as shown in the work by Andereck et al. [73]. The various regimes found by the study are summarised in Figure 3.1. The most common and well-known is the transition from Couette flow to Taylor-vortex flow.

At this transition from Couette flow to Taylor-vortex flow visible in Figure 3.1, Coles explored the impact of the outer rotating cylinder utilising the Rayleigh stability criteria [77] schematically plotted in Figure 3.2.

Below the Rayleigh stability, the Quasi-Keplerian regime is defined for astrophysical models that describe the behaviour of massive celestial bodies [78, 79]. The differential rotation, as determined by the Kepler line, is proportional, such as $\omega \sim r^{-3/2}$. When considering the inner and outer rotation, this can be expressed as $\omega_1 = \omega_2 \eta^{-3/2}$.

In the specific case where the shells rotate at the same velocity, it's important to note that this does not refer to the angular velocity. Due to the different radii of the cylinders, the inner cylinder must rotate at a faster rate to match the outer cylinder. The velocity u_φ is defined as ωr. Therefore, it's desired that $u_{\varphi,1} = u_{\varphi,2}$, which results in $\omega_1 = \omega_2 \eta^{-1}$. The different regimes are summarised in Figure 3.2.

3.3.2 Spherical Taylor-Couette

Two scenarios are described for sTC. On the one hand, the inner or only the outer sphere rotates while the other rests. On the other hand, both spheres rotate, but not at the same rotation rate.

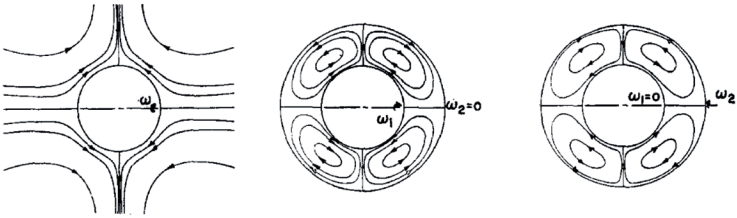

(a) Inner sphere rotation in free field

(b) Inner sphere rotation in wider outer sphere

(c) Outer sphere rotation around stationary inner sphere

Figure 3.3.: Secondary flow in sTC dependent on the rotating sphere configuration, reproduced from Habermann [80], with the permission of AIP Publishing, the rotation axis is horizontal in those cases.

Principally, a rotating shell induces momentum. For a sphere, as Habermann [80] described, in a free field, this momentum at the Equator causes the fluid to flee the sphere surface and, fulfilling continuity, entrains fluid at the Poles (see Figure 3.3(a)). Adding a secondary stationary sphere causes the entrained fluid to catch on the outflow from the Equator. This leads to a recirculation, as shown in Figure 3.3(b). Inverting the mechanism in the last Figure 3.3(c) by rotating the outer sphere instead of the inner one inverts the stream direction. The fluid there flows radially inward at the Equator and radially outward at the Poles.

Single-sphere rotation cases

This section presents cases of experiments in which only the inner sphere rotates while the outer one is at rest. Due to higher inner angular momentum $L_1 > L_2$, this principle causes potentially unstable flow, which is the focus of interest for the presented research. Investigation of differential rotating spheres was first investigated analytically using a series of Legendre polynomials by Ovsenko [81]. The referred work defined an analytic description for incompressible fluid motion in independently rotating shells. Moreover, some processed cases are presented where only the inner sphere rotates. These results were then verified by Sawatzki et al. [82], which used a boundary layer theory approach to describe the analytic solution. Moreover, Sawatzki's work went further, experimentally defining the threshold at which Taylor vortices begin to appear in the flow. These are similar to Taylor's cylinders experiment [3]; however, the vortex remains at the Equator in a spherical system and increases in mode and along the meridian with increasing velocity.

Wimmer [83] complemented the previous research with an extensive parameter range for Reynolds number $\mathrm{Re} = 10^2$ to 10^6 when $\mathrm{Re} = {}^{R_1^2\Omega_1}/_{\nu}$ using an experimental approach. The study also examined various gap sizes and provided a detailed analysis of the torque impact from the vortices. Additionally, the research investigated the number of vortices, referred to as the mode number, across the parameter range. Those results are verified numerically for the experiment's parameter range by the work of Marcus and Tuckermann [84, 85].

Bühler investigated the flow in more detail for Reynolds number $\mathrm{Re} < 5000$, focusing on the transition between the appearing modes [86]. Egbers and Rath, on the other hand, investigated transient phenomena. Depending on the gap width and the Reynolds number, their work defines a regime diagram with sections in laminar flow, Taylor vortices, secondary waves and turbulent flow [87, 88, 89]. The Taylor vortices vanish for small gaps, and only spiral structures remain. Later, the study by Hollerbach et al. [90] numerically completed these results. For increasing the aspect ratio, the results show that the number of azimuthal wavenumbers is rising.

The work from Feudel et al. [91] investigates the combination of a self-gravitating sphere where the inner shell rotates and the shells are non-isothermal. The findings, as revealed by a bifurcation analysis, show the modes of the flow pattern and heat flux resulting from this interplay. The thermal convection from the self-gravitating sphere has a destabilising effect on the inner sphere's rotational flows. The resulting mode directly affects the heat flux and results in a different mode for the same forcing, depending on the branch location of the bifurcation.

Differential rotation

Besides differential rotation, where only the inner sphere rotates, shells can rotate at different velocities. There are various possible combinations of parameters: both shells can rotate together, with either the inner or outer sphere rotating faster, or the inner shell can rotate in the opposite direction to the outer one. Ovseenko, Pearson and Munson presented initial flow analytic solutions [81, 92, 93, 94, 95]. These studies utilised a Legendre polynomial in a Taylor series to define a perturbation solution. However, obtaining high-order solutions for this description is not feasible due to the integrals becoming analytically unsolvable. Consequently, a pseudo-analytic approach was developed to generate an approximation. However, this approach does not accommodate non-linear effects and is mainly employed to describe Stokes's flow of differential rotation. Munson resolved the Taylor number using this method up to $\mathrm{Ta} = 3200$, while maintaining a Rossby number of $\mathrm{Ro} = -2$.

Surpassing the Stokes flow, the fluid streams tangentially to a supposed cylinder in the spherical gap. This was described by the Proudmann theorem [96]. Outside this tangent cylinder, the flow remains in a near-solid body manner. This is, however, only valid if the Rossby number $\mathrm{Ro} = {}^{(\omega_1-\omega_2)}/_{\omega_2} \ll 1$. At low rotation rates, the connection between the inner part of the tangential cylinder and the outer part is characterised by Stewartson layers [97, 98]. These layers are distributed in different sublayers, and their width scales with the Ekman numbers. The Ekman number, often defined as the squared inverse of the Taylor number, is represented as $\mathrm{Ek} = \mathrm{Ta}^{-0.5}$ in this case. Inside these layers, the fluid flows in opposite directions. The inner sub-layer flows from the Pole to the Equator along the tangential cylinder, while the outer layers' fluid moves from the Equator to the Poles [99].

Depending on the sign of the Rossby number, a different flow is established. Hollerbach's work [100] shows that for a high rotating sphere $\mathrm{Ta} \in [1.26 \cdot 10^4, 4.00 \cdot 10^5]$ with a small differential rotation $\mathrm{Ro} \in \pm\,[0.0316, 1[$, the flow enters a different state. For $\mathrm{Ro} > 0$, the resulting azimuthal wavenumber can reach up to 8 modes, while remaining below 3 for $\mathrm{Ro} < 0$, despite the similar angular velocity for the resulting flows. The work demonstrates the significant impact of the aspect ratio on the flow results compared with the rotation rate within the system.

The stability of the fluid flow in rotating systems depends on the rotation speed. As the differential rotation increases, the flow transitions from a stable to a transient state. In co-rotating sTC, this depends on the relative rotation speed expressed by the Rossby number and the outer rotation speed defined by the Taylor number. The Rayleigh criteria help analyse this behaviour in cylindrical geometries. Wimmer's research [101, 102] applied these criteria to sTC to find an analogy. However, it is challenging to identify the same stability margins in spherical geometries as in cylindrical geometries. The work by Wicht [20] shows that the critical Rossby number for transient flow strongly depends on the Taylor number. Furthermore, in sTC, there are additional patterns and flow regimes, such as secondary waves and fishbone patterns, as demonstrated by Egbers [87]. Nakabayashi's work [103] also explores the behaviour of rotating shells over a wide range of parameters in a regime diagram and categorises the resulting patterns based on the selected rotation rates.

4 Computational and numerical modelling

The following section introduces simplifications used in the numerical model to simulate the AtmoFlow experiment. It details the appropriate solver and the ongoing numerical discretisations for processing it. Additionally, the current section explains the selection of parameters for the force and rotation rate and concludes with the essential background for post-processing methods.

4.1 Research approach and modelling configuration

The spherical gap in Figure 1.2 is simplified to facilitate interpreting the upcoming results. Although not reproducing the experiment exactly, simplification induces greater comparability between the different parameters and the existing literature. First, a simple spherical gap geometry with aspect ratio $\eta = 0.7$, without the shaft, leads to the model's equatorial symmetry. Next, the experiment thermal Neuman's boundary conditions, equivalent to a heat flux from the heating and cooling pipes, are replaced by Dirichlet's fixed temperature boundary conditions. This step ensures better comparability between the processed simulations as the temperature applied to the fluid is not dependent on the thermal diffusion of various heat conduction sources between the heat and cooling pipes in the fluid region.
The approach includes two different thermal boundary settings. In the first scenario, known as the isothermal case (see Figure 4.1(a)), the temperature of both the inner and outer spheres is uniform in all directions, leading to a consistent temperature difference across the gap between them. This type of temperature boundary condition was also utilised in the GeoFlow experiment and is discussed in this work to bridge the gap between AtmoFlow and GeoFlow.
The second scenario shown by Figure 4.1(b) models a boundary condition resembling the AtmoFlow experiment with a heated Equator and cooled Poles. The Dirichlet boundary

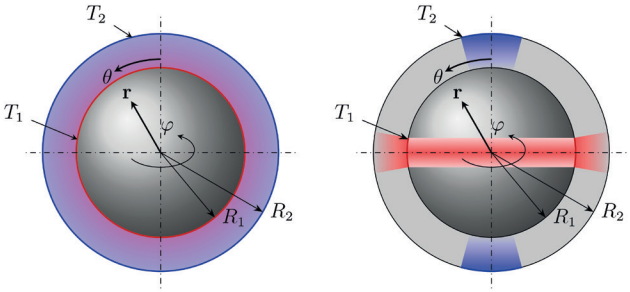

Figure 4.1.: Schematics of the numerical model for (a) the isothermal and (b) the experiment-like boundary conditions.

condition is defined by the temperature functions of the inner sphere, T_{in}, and the outer sphere, T_{out}, at the meridional angle θ, respectively.

$$T_{\text{in}}(\theta) = \left(\frac{T_1 + T_2}{2}\right) + \left(\frac{T_1 - T_2}{2}\right) \sin^n(\theta) \tag{4.1}$$

$$T_{\text{out}}(\theta) = T_2 + \left(\frac{T_1 - T_2}{2}\right) \frac{\cosh(a_{th}\cos(\theta)) - \cosh(a_{th})}{1 - \cosh(a_{th})} \tag{4.2}$$

The equations eq. (4.1) and eq. (4.2) are derived from the work of Travnikov et al. [12], and the coefficients n and a_{th} are chosen accordingly.

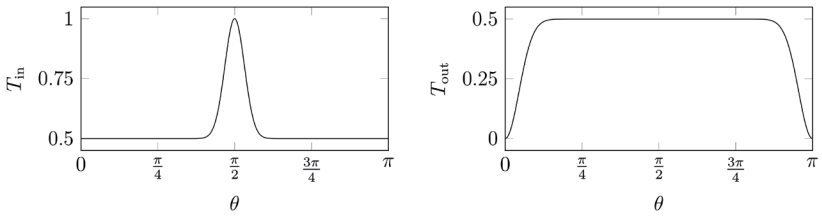

Figure 4.2.: Temperature boundary conditions for (a) the inner sphere and (b) the outer sphere for experiment-like boundary conditions.

For the non-dimensional cases where T_1 and T_2 remain at 1 and 0, respectively, the temperature distribution results over the meridian from Pole-to-Pole as shown in Figure 4.2.

4.2 Numerical methodology

This section outlines the numerical approach and settings used to address the problem. It begins with an explanation of the Finite Volume Method (FVM), followed by the formulation of discrete methods for space and time. The final part details the architecture of the solver.

The fluid in this study is assumed to be Newtonian and incompressible. Given that the focus is on the effects of the DEP force and differential co-rotation, this study utilises Direct Numerical Simulation (DNS). Turbulence models have not been validated for the current TEHD convection. Furthermore, isotropic turbulence, a requirement for models such as two-equation models [104], has not been demonstrated for buoyant flow yet.

4.2.1 The finite volume method

There are several approaches to solving CFD problems, with the FVM being one of the most widely used techniques. In FVM, the fluid domain is divided into small control volumes, allowing for a straightforward implementation of the Eulerian fluid description previously seen for the Navier-Stokes equations. OpenFOAM is based on the FVM. This approach offers several advantages for solving this problem, such as easily implementing custom equations like the DEP force. Additionally, OpenFOAM provides various built-in post-processing tools that streamline the workflow. Lastly, the FVM is known for producing accurate results while maintaining stability across numerous parameters, reducing the effort required to explore different settings.

For the incompressible continuity equation, the mass entering through one face of a control volume must match the total mass exiting through the other faces, ensuring the conservation of mass. This principle similarly applies to equations governing momentum and energy transport. For instance, momentum and temperature gradients induce fluxes at the faces of the control volumes. The sum of these fluxes across each control volume must balance to zero, maintaining the conservation laws.

This balance is used to solve the relevant Partial Differential Equations (PDEs) using the Gaussian integration method. In this process, volume integrals are transformed into surface integrals and vice versa.

4.2.2 Time discretisation

The simulations resolve time by discretising the partial derivative ∂_t to process from the time step to the next one. Using the trapeze rule at discrete time points results in the second-order accurate Crank-Nicolson (CK) scheme [21]. Blending the CK scheme with a further Backward-Euler (BE) is a common practice to ensure robustness while maintaining accuracy. This approach adds some numerical dissipation but accelerates convergence. Typically, a blend factor of 0.9 is used so that the CK scheme remains dominant over BE [105].

4.2.3 Space discretisation

In addition to time discretisation, space discretisation is necessary for calculating spatial derivatives in the partial differential equations involving the Nabla or Laplace operators. In FVM, the gradient is determined using Gauss' divergence law and is computed from each cell's centroid value and the centroid value of the neighbouring cell corresponding to that face [21].
The choice of gradient scheme, which is applied between the centroid values of these cells, significantly impacts the accuracy and robustness of the simulation. Given that Direct Numerical Simulation (DNS) is being investigated, using a second-order scheme with low dissipation is essential. The central difference scheme is well-suited for this purpose, as it is second-order and exhibits almost no dissipation compared to other second-order schemes. However, a disadvantage of this method is its dispersive nature, which necessitates more iterations to achieve convergence.

4.2.4 Methods of solution

The solvers core architecture for solving the velocity pressure coupled momentum equation is based on the Semi-Implicit Method for Pressure-Linked Equations (SIMPLE) algorithm [21, 106]. The SIMPLE algorithm addresses the coupling between pressure and velocity by incorporating all terms from the momentum equations into the pressure term, representing it as $p = F(u)$. The fluxes from the governing equation are processed using the time and space discretisation and the corresponding face of the cell's neighbour is linked in a matrix.
This work solves the pressure matrix implicitly using the Geometric Algebraic Multigrid (GAMG) solver. OpenFOAMs GAMG implementation currently performs a V-cycle; other cycle types, such as W or F, are not yet available [107]. The pressure-induced flux is then translated back into a velocity field. This iterative process continues until

the residual meets a predefined threshold, resulting firstly in a steady-state solution. To enhance the robustness and convergence of the solution, solving the pressure matrix can be repeated n times in the orthogonal correcting loop. The current simulations performed well, with $n = 3$, which ensured the pressure equation converged more quickly, thereby guaranteeing overall faster convergence.

The Pressure-Implicit with Splitting of Operators (PISO) algorithm is used to solve transient flows, but it requires the Courant-Friedrichs-Lewy (CFL) number

$$\mathrm{CFL} = \frac{|\mathbf{u}|\Delta t}{\Delta x} < 1 \tag{4.3}$$

to remain below one.

To merge the benefits of SIMPLE and PISO, a PISO loop is nested inside a SIMPLE loop, creating the PIMPLE solver. In this approach, the PISO algorithm solves the time-dependent temperature and momentum equations, repeating the process until the overall residual reaches a specified threshold. This combination allows for stable solutions even when the CFL number exceeds one. The Appendix A.2 shows a separate example for the SIMPLE and PISO algorithms.

The remaining equations, such as the temperature or the Gauss equation, do not have a vice versa correlation, such as pressure and velocity in the momentum equation. They are iteratively solved inside the SIMPLE loop. The temperature and potential flux matrices are solved using an implicit bi-conjugated gradient solver. Analogously to the orthogonal corrector loop, a general corrector loop is implemented to repeat m times the solving process before checking the residual. Current work sets for $m = 2$. An overview of the solver flowchart is located in Figure 4.3.

To ensure optimal convergence for all properties, the pressure, temperature, and potential matrices are solved until the residuals of all matrices fall below 10^{-4}. The source code and verification for the solver used are accessible via GitHub at `https://github.com/AtmoFlow/TEHDBoussinesqPimpleFoam` and through the work of Gaillard et al. [108].

4.3 Parameter space selection

Resource and computational capacity are limited, so selecting a range of parameters is essential to obtain a parameter space of interest and one of the experiment capabilities. First, the parameters for TEHD convection will be outlined, followed by a section that selects rotation rates for differential rotation.

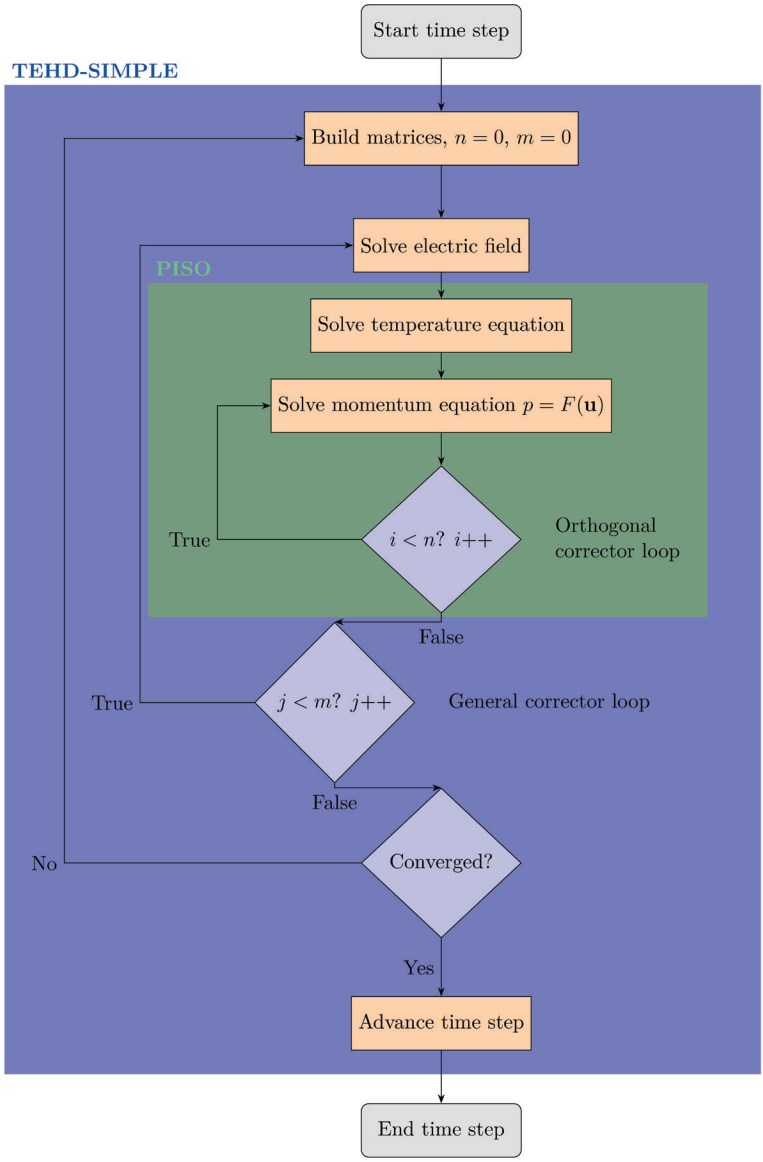

Figure 4.3.: Flowchart showing the different loops of the TEHD-PIMPLE solver until it reaches convergence.

4.3.1 Parameter selection for TEHD convection

The parameter selection for the TEHD convection is based on the capabilities of the AtmoFlow experiment, summarised in Table 1.1. It takes into account that the temperature difference must satisfy the Boussinesq approximation. For this work, four temperature differences and three electric potentials are selected. The highest temperature difference is set at $\Delta T = 20\,\mathrm{K}$, and the maximum voltage is $V_0 = 5000\mathrm{V}$. The peak voltage of the AC source will remain below 10 kV, which is within the limits of the AtmoFlow experiment.

The electric Rayleigh numbers for the dimensionless approach are calculated based on the selected potential and temperature and are summarised in Table 4.1. Notably, the Rayleigh number is the same for $\Delta T = 20\,\mathrm{K}$ with $V_0 = 1500\,\mathrm{V}$ and $\Delta T = 5\,\mathrm{K}$ with $V_0 = 3000\,\mathrm{V}$. This approach provides insight into the influence of temperature boundary conditions on the electric field in spherical geometries.

4.3.2 Parameter space for sTC

As defined in section 1.2, the objective is to study how the convection originating from the DEP force can affect the flow and pattern from differential rotation. When only the inner sphere is rotating, the flow is always potentially unstable due to the momentum flux $L_1 > L_2$. This instability is only suppressed by viscosity. Therefore, it is difficult to attribute the source of instability exclusively to the DEP force when only the inner sphere is rotating. The primary goal, however, is to identify the threshold at which the additional momentum from TEHD convection destabilises a previously stable differentially rotating flow or, conversely, to observe how the DEP force might stabilise an unstable transient sTC flow. This analysis is more effectively conducted using co-rotating spheres. Consequently, the current investigation focuses on this specific type of differential rotation, though other configurations are possible.

Table 4.1.: Parameter range for TEHD convection given by the electric Rayleigh number, $\mathrm{Ra_E}$.

V_0 \ ΔT	2	5	10	20
1500	$1.59 \cdot 10^4$	$3.98 \cdot 10^4$	$7.95 \cdot 10^4$	$1.59 \cdot 10^5$
3000	$6.36 \cdot 10^4$	$1.59 \cdot 10^5$	$3.18 \cdot 10^5$	$6.36 \cdot 10^5$
5000	$1.77 \cdot 10^5$	$4.42 \cdot 10^5$	$8.84 \cdot 10^5$	$1.77 \cdot 10^6$

Table 4.2.: Parameter range for the differential rotation rate Ro.

Ro	0.429	0.708	0.939	1.04	1.14
Ω_1	Ω_2/η	$\Omega_2/\eta^{3/2}$	$\Omega_2/\eta^2 \cdot 0.95$	Ω_2/η^2	$\Omega_2/\eta^2 \cdot 1.05$

Three distinctive regimes are chosen for differential rotation, adapted from typical regimes from TC seen in section 3.3.1. First, both spheres rotate at the same azimuthal velocity. It's important to note that the spheres are not the same size. The inner sphere's angular velocity must be higher than the outer one, resulting in a co-rotating differential rotating case. The velocity of the inner sphere is represented as $u_{\varphi,1}$ and the velocity of the outer sphere as $u_{\varphi,2}$. The condition states that $u_{\varphi,1} = u_{\varphi,2}$. Reformulating this in terms of angular velocities, results in $\Omega_1 = {}^{u_{\varphi,1}}/_{R_1}$ and $\Omega_2 = {}^{u_{\varphi,2}}/_{R_2}$ for the inner and outer sphere respectively. This results in $\Omega_1 = \Omega_2 {}^{R_2}/_{R_1} = {}^{\Omega_2}/_{\eta}$.

The second regime is related to a stellar system known as the quasi Keplerian-flow, where the angular velocity scales with the radius as $\Omega \sim r^{-3/2}$ [78]. When applied to the boundary conditions of the rotating shells, it results in $\Omega_1 = {}^{\Omega_2}/_{\eta^{3/2}}$.

The equilibrium for the angular momentum on the equatorial disc is achieved when the angular momentum on the inner shell, $L_1 = \Omega_1 R_1^2$, matches the angular momentum on the outer sphere, $L_2 = \Omega_2 R_2^2$ [102]. In other words, when $L_1 = L_2$. Rearranging this expression leads to the third regime $\Omega_1 = {}^{\Omega_2}/_{\eta^2}$. This regime is of significant interest as there are potentially unstable regimes due to the tipping point of the angular momentum in the equatorial slice. To investigate the stabilising or destabilising effect of the TEHD convection on this threshold, extended parameters around $L_2 = L_1$ are chosen. Hence, on one side, a differential rotation parameter is selected for the inner sphere rotating 5% faster, and on the other side, another parameter is determined to be 5% slower.

The resulting Rossby numbers and their corresponding angular velocities depend on the outer sphere angular velocity and are summarised in Table 4.2.

The relative differential rotation regime is established, such as $\Omega_1 = f(\Omega_2)$, clarifying the definition of the inner sphere's rotation relative to the outer sphere. However, the specific values for rotation are not defined yet, only the relative rotation between the outer and inner spheres. These values must be in the range of the capabilities of the experiment built by Airbus, which can rotate the outer sphere at a maximum frequency of 2 Hz. The experiment at this rotation rate at this level suppresses any convection pattern coming from TEHD, which is limited to 10 kV peak voltage, as seen before. The

current task is to determine an approximate threshold for rotation at which the influence of the DEP forcing becomes negligible.

The previous subsection 3.3.2 addressed differential rotation, explaining how the base flow circulates from the Poles to the Equator within the inner gap layer, generating an outflow at the equatorial level. The fluid subsequently returns to the Poles in the outer layer of the gap, ensuring continuity through an inflow in the polar region. This differential rotation, acting as a basic flow, is denoted by both meridional and azimuthal velocities extending from the Poles to the Equator. In contrast, the flow in spherical TEHD convection with isothermal boundary conditions is predominantly driven by radial velocity.

An estimation is performed by comparing the magnitudes of velocity from each mechanism. This analysis is aligned with the capabilities of the AtmoFlow experiment, and the following section will utilise its fluid properties. Detailed information required to trace the subsequent calculation steps can be found in Appendix A.1.

A conductive base state is assumed to estimate the velocity resulting from TEHD convection. The studies by Seelig et al. [109] and von Larcher [110] provide approximations for thermal wind

$$u_T = \sqrt{g_\mathrm{e}\gamma_\mathrm{e} d} \tag{4.4}$$

in stratified thermal layers under gravity. Instead of using the terrestrial gravitation defined by von Larcher, the electric gravitation g_e is chosen.

Yavorskaya et al. [111] and Mutabazi et al. [50] described an analytic form for conductive base state temperature T_b and electric field $\mathbf{E}_{\mathrm{b},\gamma_\mathrm{e}}$ in spheres. T_0 represent the reference temperature.

$$T_\mathrm{b}(r) - T_0 = \frac{\eta \Delta T}{1-\eta}\left(\frac{R_2}{r} - 1\right) \tag{4.5}$$

$$\mathbf{E}_{\mathrm{b},\gamma_\mathrm{e}}(r) = -\frac{\eta V_0}{d}\frac{\gamma_\mathrm{e}}{\ln(1-\gamma_\mathrm{e})}\left(\frac{R_2}{r}\right)^2\left[1-\gamma_\mathrm{e}\frac{T_\mathrm{b}(r)-T_0}{\Delta T}\right]^{-1} \tag{4.6}$$

Acceleration is deduced from the dielectrophoretic force $\mathbf{f}_\mathrm{DEP}$ resulting in the electric gravity $g_\mathrm{e} = |\mathbf{g}_\mathrm{e}|$

$$\mathbf{g}_\mathrm{e} = \frac{e\epsilon_0\epsilon_\mathrm{r}}{(2\rho_0)}\mathbf{E}_{\mathrm{b},\gamma_\mathrm{e}}(r)^2\frac{\partial(T_b(r)-T_0)}{\partial r} \tag{4.7}$$

Based on the assumption of a basic state, the velocity resulting from TEHD convection is strictly in the radial direction. The value for u_T is measured at the mid-gap, $R_{1/2} = {}^{(R_1+R_2)}/_2$, where it is expected to experience the maximum velocity from the DEP forcing due to the most significant distance from the walls. The AtmoFlow experiment can produce a thermal electric wind of $u_T = 5.30 \cdot 10^{-3}\mathrm{m\,s^{-1}}$ by applying this estimation for the highest temperature and electric potential values seen in Table 4.1. Using the previously defined dimensionless approach, the resulting velocity is $u_T^* = 1047$.

The velocity estimation from TEHD convection has been completed, and the Rossby numbers have been defined. The following steps outline the velocity estimation resulting from differential rotation in spherical coordinates, represented as u_r, u_θ, and u_φ. Except for u_r, these velocities are orthogonal to the processed base state velocity u_T and can be combined to yield

$$u_{\perp T} = \sqrt{u_\theta^2 + u_\varphi^2}. \tag{4.8}$$

To define $u_{\perp T}$, the analytic solution presented by Sawatzki [82] is referenced, where the boundary layer equation is developed into a system of differential equations. It is important to note that this solution is only valid to single-sphere rotation. Therefore, it is not recommended for benchmarking purposes, as will be demonstrated later in this work. This estimation was made in the early stages of this thesis, before some analytical tools, such as those later found in the DRACULA[1] code, were available. An attempt is made by taking the relative rotation $\Omega_{\mathrm{rel}} = \Omega_1 - \Omega_2$ of the two-sphere rotating system as the rotation speed of a single sphere rotating system, deliberately neglecting any effect from the Coriolis force.
The estimation follows

$$u_\theta = R_1\Omega_{\mathrm{rel}}\frac{\Omega_{\mathrm{rel}}R_1 d}{\nu}\frac{d}{R_1}\frac{\sin(\theta)\cos(\theta)}{24}d^*(1-d^*)(5(d^*)^2 - 9d^* + 3) \tag{4.9}$$

$$u_\varphi = R_1\Omega_{\mathrm{rel}}\sin(\theta)(1-d^*) \tag{4.10}$$

where $d^*(r) = {}^{(r-R_1)}/_{(R_2-R_1)}$. An average is calculated since the velocities u_θ and u_φ have dependencies in radial in meridional directions. So $\langle u_{\perp T}\rangle_V$ is the spatial average of $u_{\perp T}$ by the volume.
A two-dimensional field is defined in terms of the radial direction, represented by $\mathbf{e}_r$, and its orthogonal component in the meridional and azimuthal planes, denoted as $\mathbf{e}_{\theta,\varphi}$. The resulting angle α is calculated using the formula $\alpha = \tan^{-1}\left({}^{\langle u_{\perp T}\rangle_V}/_{u_T}\right)$. A schematic representation of this is shown in Figure 4.4(a).

[1] Repository `https://github.com/AtmoFlow/DRACULA`

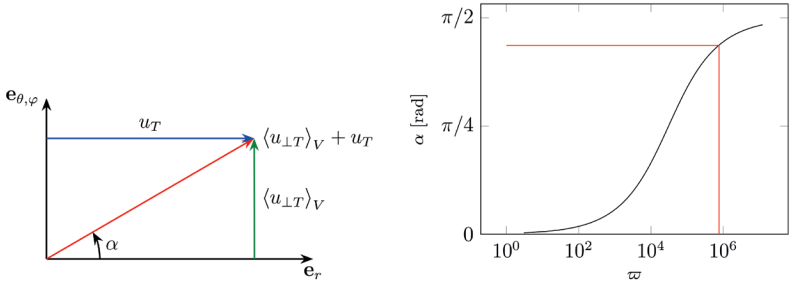

(a) (b)

Figure 4.4.: Plots of (a) the graphical representation of the angle α calculation and (b) the angle from the ratio of velocities from DEP forcing and differential rotation.

Table 4.3.: Parameters range selected for rotation rates ϖ. The red text colour indicates where the combined flow from the analytic solution reaches 90% of the velocity from sTC. The green columns are the selected parameters for the upcoming simulations.

Ta	13.1	48.5	110	194	601
Ro = 0.429	2.41	8.91	$2.02 \cdot 10^1$	$3.56 \cdot 10^1$	$1.10 \cdot 10^2$
Ro = 0.708	6.56	$2.43 \cdot 10^1$	$5.51 \cdot 10^1$	$9.71 \cdot 10^1$	$3.01 \cdot 10^2$
Ro = 0.939	$1.15 \cdot 10^1$	$4.27 \cdot 10^1$	$9.69 \cdot 10^1$	$1.71 \cdot 10^2$	$5.30 \cdot 10^2$
Ro = 0.104	$1.42 \cdot 10^1$	$5.25 \cdot 10^1$	$1.19 \cdot 10^2$	$2.10 \cdot 10^2$	$6.51 \cdot 10^2$
Ro = 1.14	$1.71 \cdot 10^1$	$6.34 \cdot 10^1$	$1.44 \cdot 10^2$	$2.53 \cdot 10^2$	$7.85 \cdot 10^2$
Ta	$1.76 \cdot 10^3$	$4.42 \cdot 10^3$	$1.25 \cdot 10^4$	$3.31 \cdot 10^4$	$8.85 \cdot 10^4$
Ro = 0.429	$3.23 \cdot 10^2$	$8.12 \cdot 10^2$	$2.30 \cdot 10^3$	$6.08 \cdot 10^3$	$1.63 \cdot 10^4$
Ro = 0.708	$8.81 \cdot 10^2$	$2.21 \cdot 10^3$	$6.26 \cdot 10^3$	$1.66 \cdot 10^4$	$4.43 \cdot 10^4$
Ro = 0.939	$1.55 \cdot 10^3$	$3.90 \cdot 10^3$	$1.10 \cdot 10^4$	$2.92 \cdot 10^4$	$7.80 \cdot 10^4$
Ro = 0.104	$1.91 \cdot 10^3$	$4.79 \cdot 10^3$	$1.35 \cdot 10^4$	$3.59 \cdot 10^4$	$9.59 \cdot 10^4$
Ro = 1.14	$2.30 \cdot 10^3$	$5.77 \cdot 10^3$	$1.63 \cdot 10^4$	$4.32 \cdot 10^4$	$1.16 \cdot 10^5$
Ta	$2.37 \cdot 10^5$	$6.37 \cdot 10^5$	$1.71 \cdot 10^6$	$4.58 \cdot 10^6$	$1.23 \cdot 10^7$
Ro = 0.429	$4.35 \cdot 10^4$	$1.17 \cdot 10^5$	$3.14 \cdot 10^5$	$8.41 \cdot 10^5$	$2.26 \cdot 10^6$
Ro = 0.708	$1.19 \cdot 10^5$	$3.19 \cdot 10^5$	$8.56 \cdot 10^5$	$2.29 \cdot 10^6$	$6.16 \cdot 10^6$
Ro = 0.939	$2.09 \cdot 10^5$	$5.61 \cdot 10^5$	$1.51 \cdot 10^6$	$4.04 \cdot 10^6$	$1.08 \cdot 10^7$
Ro = 0.104	$2.57 \cdot 10^5$	$6.90 \cdot 10^5$	$1.85 \cdot 10^6$	$4.96 \cdot 10^6$	$1.33 \cdot 10^7$
Ro = 1.14	$3.10 \cdot 10^5$	$8.32 \cdot 10^5$	$2.23 \cdot 10^6$	$5.98 \cdot 10^6$	$1.61 \cdot 10^7$

In a dimensionless framework, the relative velocity can be expressed as

$$\varpi = \mathrm{Ta} \cdot \mathrm{Ro}^2 = \frac{4\left(\Omega_1 - \Omega_2\right)^2 d^4}{\nu^2}. \tag{4.11}$$

At $\varpi = 7.65 \cdot 10^5$, the angle reaches 1.4 radians, as illustrated in Figure 4.4(b). This indicates that the combined velocity angle approaches 90% of the velocity achieved through differential rotation only. Moreover, a plateau begins to form, suggesting that significant changes in velocity do not occur beyond this point. As a result, it is essential to determine the rotation rate for cases where $\varpi < 7.65 \cdot 10^5$. The corresponding angular velocities for the specified Rossby numbers, along with all relevant outer rotation speeds applicable to the AtmoFlow experiment, are provided in Table 4.3.

This estimation indicates that the relative rotation surpasses the previously established limit at $\mathrm{Ta} = 6.37 \cdot 10^5$ and $\mathrm{Ro} = 1.14$. Consequently, cases involving more significant rotations are of lesser interest. However, there are still 12 outer rotation velocities available for consideration. Given the constraints of numerical calculation resources and finite data storage, further selections are necessary.

Six of these 12 potential outer rotation speeds have been chosen, ensuring that the Taylor numbers increase approximately equidistantly in powers of ten, starting from conditions close to Stokes flow.

To summarise, six outer rotation speeds have been selected, each associated with five different Rossby numbers, as highlighted in green in Table 4.3. Together with the 12 electric Rayleigh numbers identified earlier, this parameter range encloses a total of 360 simulations.

4.4 Diagnostics and evaluation

In addition to commonly used methods like Fast Fourier Transformation (FFT), some less common techniques and a self-derived in-flow Nusselt number are employed for post-processing. The approach behind these methods is summarised in this final section.

4.4.1 Thermal transport

The eq. (2.38) describes the non-dimensioned heat transfer. For stationary conduction cases, this equation reduces in cartesian coordinates to

$$0 = \boldsymbol{\nabla}^2 T. \tag{4.12}$$

In spherical coordinates, the conduction equation results in the following

$$0 = \frac{1}{r^2}\frac{\partial}{\partial r}\left(r^2\frac{\partial T}{\partial r}\right). \tag{4.13}$$

The PDE eq. (4.13) has been solved for an inner heated sphere and an outer cooled environment. The temperature at the dimensionless inner radius is $T = 1$ at $r_1 = \eta/(1-\eta)$, while at the dimensionless outer radius, the temperature is $T = 0$ at $r_2 = 1/(1-\eta)$.

$$T_\mathrm{b}(r) = \frac{\eta(\eta r - r + 1)}{r(\eta - 1)^2} \tag{4.14}$$

Its derivative is then calculated in the following equation

$$\frac{\partial T_\mathrm{b}}{\partial r} = \frac{\eta}{r^2(\eta - 1)^2}. \tag{4.15}$$

The derivative measures the conductive heat transfer through a sphere for a specified surface area. The conductive heat flux Q_cond is calculated by integrating the normal temperature gradient from eq. (4.15) using spherical coordinates.

$$Q_\mathrm{cond} = \int_0^{2\pi}\int_0^{\pi}\frac{\partial T_\mathrm{b}}{\partial r}r^2\sin(\theta)\,\mathrm{d}\theta\mathrm{d}\varphi \tag{4.16a}$$

$$Q_\mathrm{cond} = \int_0^{2\pi}\int_0^{\pi}\frac{\eta}{(\eta-1)^2}\sin(\theta)\,\mathrm{d}\theta\mathrm{d}\varphi \tag{4.16b}$$

$$Q_\mathrm{cond} = -\int_0^{2\pi}\frac{2\eta}{(\eta-1)^2}\,\mathrm{d}\varphi \tag{4.16c}$$

$$Q_\mathrm{cond} = -\frac{4\pi\eta}{(\eta-1)^2} \tag{4.16d}$$

This results in an analytic heat conduction solution, which depends only on the aspect ratio. Using this, the Nusselt number is determined at the wall. It is defined by the ratio of the total heat transfer Q_t to the conductive heat transfer Q_cond.

$$\mathrm{Nu} = \frac{Q_\mathrm{t}}{Q_\mathrm{cond}} \tag{4.17}$$

The total heat transfer in the numerator is later processed from the numerics.

Additionally, monitoring the Nusselt number across different radii in the flow is of major interest to see the evolution where the heat proceeds from one to the other shell. Using the methods described by Wang et al. [70], the in-flow Nusselt number Nu^q is defined as

$$\mathrm{Nu}^q = \frac{(\eta-1)^2}{4\pi\eta} \left\langle r^2 \left[u_r T - \partial_r T\right]\right\rangle_{A,t}. \tag{4.18}$$

It is important to note that this derivation is only valid for the integral taken over a time-averaged concentric sphere with surface area A within the gap. This integral is denoted by $\langle \dots \rangle_{A,t}$. A detailed derivation can be found in Appendix A.4.

4.4.2 Averaged kinetic energy

The kinetic energy is space and then time averaged $\langle \dots \rangle_{V,t}$ by the volumetric integral of kinetic energy $1/2|\mathbf{u}|^2$ by the fluid volume V and then time-averaged, such as

$$\tilde{E}_{\mathrm{kin}} = \frac{1}{2} \langle \mathbf{u}^2 \rangle_{V,t} \tag{4.19}$$

4.4.3 Spatial thermal mode energy (STME)

The STME E_m is used from the work of Gaillard et al. [14]. It is performed by applying a spatial Fast Fourier Transformation (FFT) over the domain of interest. The quantity of interest here is the temperature. The different modes from this analysis are then summed by weighting each mode increasingly, resulting in

$$E_m = \sum_m A_m^2 m \tag{4.20}$$

where A_m is the amplitude of mode m from the FFT.

This measure provides a single-value indicator of the mode distribution and offers qualitative insights into the flow regime. In stable flow conditions, dominant modes typically exhibit higher energy values, reflecting a more organised and coherent structure in the flow. Furthermore, higher-order dominant modes correspond to elevated energy levels. Conversely, when the energy is distributed across a broad spectrum of modes, particularly those with high wavenumbers and lower amplitudes, the overall mode energy decreases, indicating a more chaotic or less coherent flow structure.

4.4.4 Empirical orthogonal function

Empirical Orthogonal Functions (EOFs) are a mathematical technique used in multivariate data analysis, particularly for identifying patterns in datasets that exhibit variability across both space and time. The method aims to decompose a large dataset into a set of orthogonal basis functions, each representing a mode of variability, ranked in order of their contribution to the total variance. EOFs are closely related to Principal Component Analysis (PCA) but are specifically suited for data with both spatial and temporal dimensions. In the current work, the EOFs are performed on 300 equidistant time-steps. The time-step is selected using the CFL = 5 number after reaching convergence. This ensures that a period with the most usable data is retrieved, depending on the velocity in the field. Slow rotating flow has a bigger time-step while fast rotating flow has a lower time-step.

A given field is represented by x_{ij} in spaces n and m, and time is resolved in t. The field data is then concatenated in a matrix X. Then the covariance is processed, and the eigenvector is defined. Those eigenvectors are now the different EOFs sorted by decreasing amplitude, as schematically shown in Figure 4.5(a). The related PCA defines the level of the defined mode for a given time in Figure 4.5(b).

$$X = \begin{bmatrix} x_{11,t_1} & x_{12,t_1} & \dots & x_{nm-1,t_1} & x_{nm,t_1} \\ x_{11,t_2} & x_{12,t_2} & \dots & x_{nm-1,t_2} & x_{nm,t_2} \\ \vdots & \vdots & \ddots & \vdots & \vdots \\ x_{11,t_p} & x_{12,t_p} & \dots & x_{nm-1,t_p} & x_{nm,t_p} \end{bmatrix}$$

The current thesis utilises a Python-coded EOF library developed by Rieger [112, 113]. This library offers benchmark-verified tools for processing large data sets with EOFs. Given the substantial mesh size in this work, using this library is essential.

4.5 Mesh independence

In addition to the defined setup, a mesh independence test is performed. The primary quantities analysed in the results are heat flux and kinetic energy, which are used to assess mesh quality.
In Figure 4.6, the dimensionless heat flux, represented by the Nusselt number, and the dimensionless volumetric nd time-averaged kinetic energy are plotted against increasing mesh density. The strongest parameters from sTC and forcing from DEP are employed. The Taylor number is set at $6.37 \cdot 10^5$, while the Rossby number is Ro = 1.14, and the

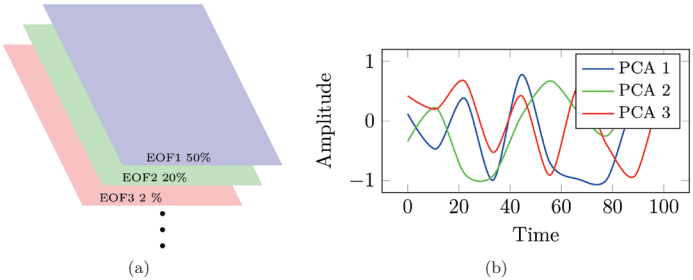

Figure 4.5.: Schematic representation of (a) EOF decomposition for space field and (b) its related PCA.

electric Rayleigh number is $\mathrm{Ra_E} = 1.77 \cdot 10^6$. A finer mesh is necessary to resolve smaller scales that occur at higher velocities due to stronger forcing, which ultimately leads to optimised mesh quality under these elevated conditions.

The selected mesh is structured and consists of hexahedrons. To improve boundary resolution, near-wall cell growth is implemented with a ratio of 10, transitioning from the smallest cell at the wall to the largest cell in the midgap.

Convergence for the Nusselt number occurs with $1.54 \cdot 10^6$ cells and is complete with $24 \cdot 10^6$ cells. The convergence of kinetic energy is achieved with a mesh of $5.18 \cdot 10^6$ cells. As shown in Figure 4.6, the optimal mesh configuration is the one with $24 \cdot 10^6$ cells. However, due to the number of parameters planned for this thesis and the need to

Figure 4.6.: Mesh independency for integral quantities Nusselt number Nu (—o—) and kinetic energy $\tilde{E}_{\mathrm{kin}}$(—×—).

store time-resolved quantities, using this mesh would result in an unmanageable amount of data and require significantly more computational resources.
In contrast, the mesh with $12.3 \cdot 10^6$ cells demonstrates an error of less than 1% compared to the converged case, making it a suitable alternative. Additionally, this mesh reduces the required storage by half, allowing for the resolution of time-resolved contours. Therefore, the mesh with $12.3 \cdot 10^6$ cells is selected for the current work.

5 TEHD convection in spherical shell

The following results concentrate exclusively on TEHD convection in spherical shells. This section begins with a brief description of the setup and the processed parameters. Next, the results present isosurfaces for qualitative analysis, followed by heat flux and kinetic energy for a more quantitative examination. Lastly, the results are compared with existing literature, particularly prior publications from the GeoFlow I and II experiments.

5.1 Model formulation

The governing equations outlined in section 2.5 are simplified for this case. Since no rotation is applied, they are simplified to

$$\boldsymbol{\nabla} \cdot \mathbf{u} = 0 \tag{5.1}$$

$$\partial_t \mathbf{u} + (\mathbf{u} \cdot \boldsymbol{\nabla})\mathbf{u} = -\boldsymbol{\nabla} P + \mathrm{Pr}\, \boldsymbol{\nabla}^2 \mathbf{u} - \mathrm{Pr}\, \mathrm{Ra}_\mathrm{E} |\mathbf{E}|^2 \boldsymbol{\nabla} T \tag{5.2}$$

$$\partial_t T + (\mathbf{u} \cdot \boldsymbol{\nabla}) T = \boldsymbol{\nabla}^2 T \tag{5.3}$$

$$\boldsymbol{\nabla} \cdot [(1 - \gamma_e T)\, \mathbf{E}] = 0, \quad \text{with} \quad \mathbf{E} = -\boldsymbol{\nabla} \vartheta \tag{5.4}$$

The momentum eq. (5.2) omits the Coriolis and centrifugal forces. The Gauss equation in eq. (5.4) must be solved to solve the temperature-dependent electric field. Additionally, the temperature eq. (5.3) must also be solved.

In this setup, the fluid between an inner isothermal heated sphere and an outer cooled one is investigated. Uniquely, the electric field is considered here as a source of force on

the fluid. The Dirichlet boundary conditions are summarised as follows

$$\begin{cases} \mathbf{u} = 0, \quad T = 1, \quad \vartheta = 1, \quad \boldsymbol{\nabla} p = 0, \quad \text{at} \quad r = \dfrac{\eta}{1-\eta} \\ \mathbf{u} = 0, \quad T = 0, \quad \vartheta = 0, \quad \boldsymbol{\nabla} p = 0, \quad \text{at} \quad r = \dfrac{1}{1-\eta} \end{cases} \tag{5.5}$$

Both spheres are at rest, having no-slip boundary conditions. The inner sphere has a uniform temperature of 1, while the outer one is set to 0. The inner sphere potential is set to 1 setting in the electric field as schematically represented in Figure 5.1

The parameters selected for this preliminary study are derived from all the TEHD parameters outlined in section 4.3.1 see Table 4.1. These parameters comprise four different temperature settings and three different electric potential values, leading to 12 simulations. For $\mathrm{Ra_E} = 1.59 \cdot 10^5$ from parameters section 4.3.1 there a two thermo-electric parameters γ_e which are equal for $\gamma_\mathrm{e} = 0.015$ and $\gamma_\mathrm{e} = 0.06$. To further quantify the effect of the thermo-electric parameter on the electric field, two additional simulations are processed at the remaining thermo-electric parameters $\gamma_\mathrm{e} = 0.006$ and $\gamma_\mathrm{e} = 0.03$. In total, 14 simulations are processed in this chapter.

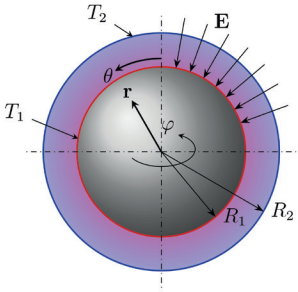

Figure 5.1.: Problem geometry and boundary conditions for TEHD convection in spherical shell.

5.2 Results

The results section is divided into two subsections. The first subsection presents four cases of rising electric Rayleigh numbers. For each simulation selected, the isosurfaces

of temperature and velocity are plotted. Following this, the temporal development is illustrated using space-time plots.
The second subsection compares the evolution of Nusselt number Nu and time and space averaged kinetic energy $\tilde{E}_{\text{kin}}$ related to the rising electric Rayleigh number.

5.2.1 Spatial and temporal evolution of TEHD convection

Figure 5.2 illustrates the temperature and the radial and meridional velocities for the selected electric Rayleigh numbers $\text{Ra}_{\text{E}} = 1.59 \cdot 10^4$, $\text{Ra}_{\text{E}} = 3.98 \cdot 10^4$, $\text{Ra}_{\text{E}} = 3.18 \cdot 10^5$ and $\text{Ra}_{\text{E}} = 1.77 \cdot 10^6$. The isosurfaces are taken on the Pole-to-Pole cut, the equatorial cut, and the spherical slice at radius $r_{1/4}$ defined as

$$r_{1/4} = (1 + 3\eta)/(4 - 4\eta) \tag{5.6}$$

The colour bar added to all figures simultaneously represents the maximal values present in the field.
The first column has the lowest electric Rayleigh number among the parameters studied. Plume structures are evenly distributed shown by the temperature isosurface in Figure 5.2(a). A plume is a rising column of hot fluid moving from the inner sphere to the outer sphere, marked by a dotted black circle. Over the overall surface of the sphere, six plumes are identified: four are positioned along the Equator, while one is located at each Pole. The shape of the plumes resembles a square structure on the shell layer.
Figure 5.2(e) shows the radial velocity, highlighting the outward-oriented velocity from the emerging plume. Each plume exhibits a substantial positive radial velocity ($u_r > 0$), indicating the mass transport and, therefore, the heat convection from the inner to the outer sphere.
In contrast, the final panel in the column Figure 5.2(i) depicts the meridional velocity in the θ-direction, where the secondary flow is noticeable. The outward-oriented flow from the Poles toward the Equator is visible for the plumes located at the Poles. Additionally, the plume at the Equator displays simultaneous rising flow toward the North Pole ($u_\theta < 0$) and meridional descending flow toward the South Pole ($u_\theta > 0$).
At the intersection of the secondary streams, the fluid moves toward the inner sphere ($u_r < 0$), entraining colder fluid from the outer boundary condition to preserve continuity. This interplay results in the formation of cold sheets that connect the edges of the plumes, as visualised by a white dashed line in Figure 5.2(a).

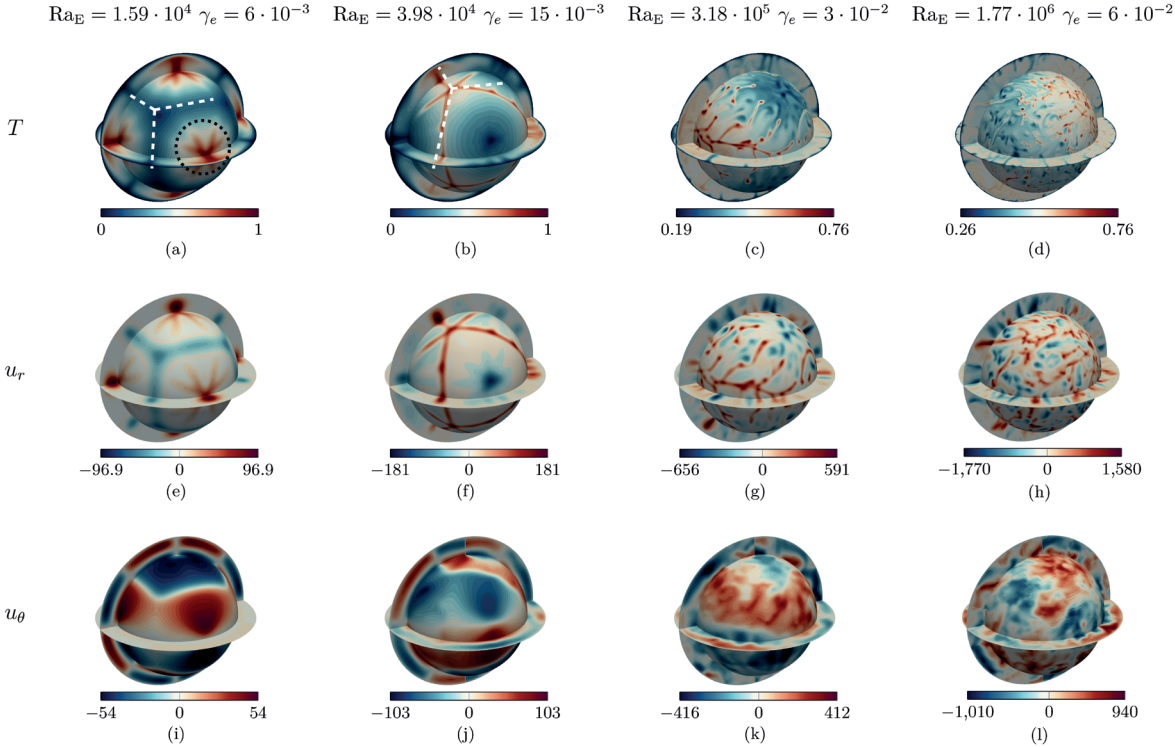

Figure 5.2.: Isosurface plots of temperature, T, radial velocity, u_r, and meridional velocity, u_θ, are shown in the top, middle, and bottom rows, respectively, across equatorial, meridional, and radial cross-sections on a spherical shell located at a quarter-radius $r_{1/4}$. Colour scales are provided below each panel. From left to right, the plots increase $\mathrm{Ra_E}$ incrementally.

The following electric Rayleigh number illustrated in the second column of Figure 5.2 is slightly higher, at $\mathrm{Ra_E} = 3.98 \cdot 10^4$. This increase leads to significant changes compared to the previously analysed case. While plumes are still present, the pattern of the hot plumes, shown in Figure 5.2(b), has become less organised than before. Instead of a uniform arrangement, the hot and cold plumes are now placed more randomly across the sphere and are no longer evenly distributed on the sphere's West, East, North and South.
The cold fluid sheets, previously depicted in Figure 5.2(a), are now rather hot and connect the areas of hot plume activity, also marked by a white dashed line in Figure 5.2(b). These sheets are no longer lines connecting the plumes perfectly, but instead have small vacillating structures along them. The shape of the plume cells has become triangular, and in this scenario, only five large-scale plumes remain.
In Figure 5.2(f), areas with positive radial velocity show hot plumes in the prior temperature isosurface of Figure 5.2(b). In these regions, the flow moves hot fluid from the inner shell toward the outer shell. Conversely, in areas where the radial velocity $u_r < 0$, cold plumes draw cold fluid from the outer shell back to the inner spherical shell.
In comparison to the previous electric Rayleigh number of the first column in Figure 5.2, the meridional velocity shown in Figure 5.2(j) does not clearly relate to the present sheet indicated in Figure 5.2(b).

The third column depicts the isosurfaces of temperature and velocities for the Rayleigh number $\mathrm{Ra_E} = 3.18 \cdot 10^5$. The temperature isosurface in Figure 5.2(c) illustrates clusters which agglomerate in finger-looking structures on the western side of the sphere. While there is still a distinct hot and cold region, the previously visible sheets are now irregular. Additionally, the rising plumes on the Pole-to-Pole cut and the equatorial cut show additional vacillation, which makes it hard to discern large-scale plume structures.
A similar trend is observed in the radial velocity shown in Figure 5.2(g). As depicted in the previous Figures 5.2(g) and 5.2(f), the regions of Figure 5.2(c) with hot fluid exhibit a significant positive radial velocity u_r shown by 5.2(g), which also clusters for outward-oriented flow on the western side of the sphere. Simultaneously, inward-oriented flow agglomerates on the east side of the sphere.
For the meridional velocity of the third case in Figure (5.2(k)), identifying organised structures becomes even more challenging, as the flow becomes irregular in this direction. The shape of the single plume does not adhere to any distinct geometry, appearing instead as isolated agglomerated structures. To summarise, the positions of the hot and cold fluid regions are linked to the radial velocity rather than to the meridional velocity.

The behaviour observed is similar to that in the previous simulation for the last selected example parameter shown in the last column of Figure 5.2. There are still areas of hot and cold regions where plumes cluster, but the structure within these clusters is even more scattered. Despite the high level of mixing caused by the forcing, there are noticeable cold spots within the hot cluster and vice versa, as illustrated in Figure 5.2(d). Additionally, the edge of the plume region is no longer distinguishable.

Furthermore, the radial velocity presented in Figure 5.2(h) now shows a homogeneous distribution of rising and descending flow from the inner to the outer sphere, eliminating any visible accumulation of radial velocity. It is important to note that the magnitude of the radial velocity aligns well with the estimation process discussed in the previous section, section 4.3.2. The velocity calculated using von Larcher's method, which incorporates an electrically defined gravity, yields a similar magnitude of radial velocity, approximately $\mathcal{O}(u_r) = 10^3$.

In the final Figure 5.2(l), the meridional velocity appears even more scattered than in the previous electric Rayleigh number analysis. The strong forcing from the DEP force induces highly irregular patterns.

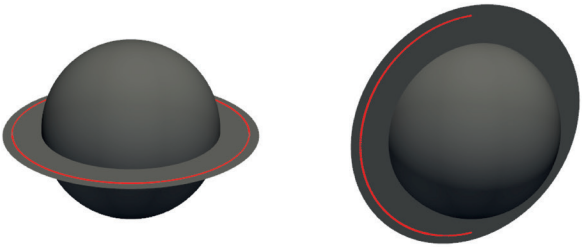

(a) (b)

Figure 5.3.: Schematic view of the probe location on (a) the Equator and (b) the Meridian

Space-time analysis

The following panels in Figure 5.4 and Figure 5.5 illustrate the evolution of temperature over time on the Equator and a selected Meridian at radius

$$r_{3/4} = (3 + \eta)/(4 - 4\eta) \tag{5.7}$$

which represents three-quarters of the gap width. The Equator and the Meridian probe locations are schematically shown in Figures 5.3(a) and 5.3(b) respectively.

Upon examining the space-time plots for electric Rayleigh numbers $\mathrm{Ra_E} = 1.59 \cdot 10^4$ and $\mathrm{Ra_E} = 3.98 \cdot 10^4$, one finds that the temperature remains time-independent, as no

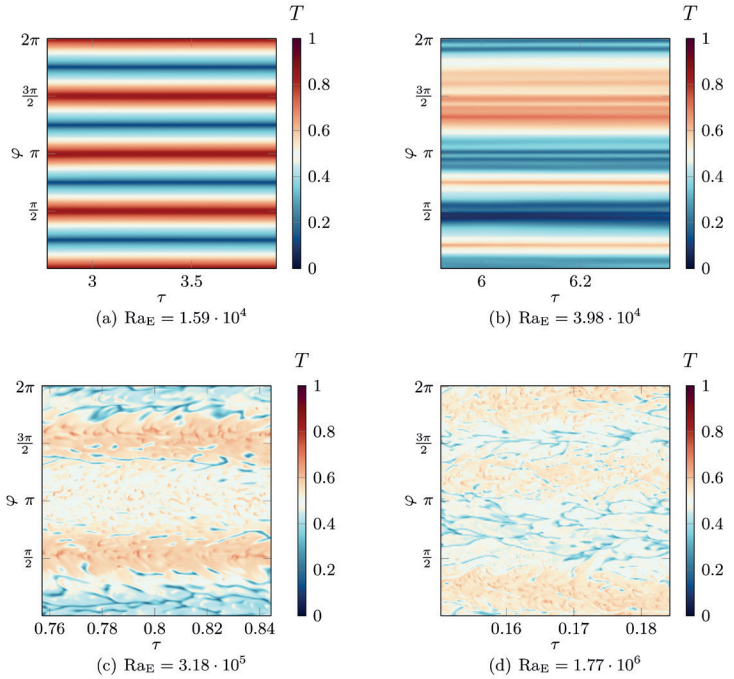

(a) $\mathrm{Ra_E} = 1.59 \cdot 10^4$ (b) $\mathrm{Ra_E} = 3.98 \cdot 10^4$

(c) $\mathrm{Ra_E} = 3.18 \cdot 10^5$ (d) $\mathrm{Ra_E} = 1.77 \cdot 10^6$

Figure 5.4.: Space-time plots on the Equator at $r_{3/4}$ and $\theta = \pi/2$ for rising electric Rayleigh $\mathrm{Ra_E}$ numbers.

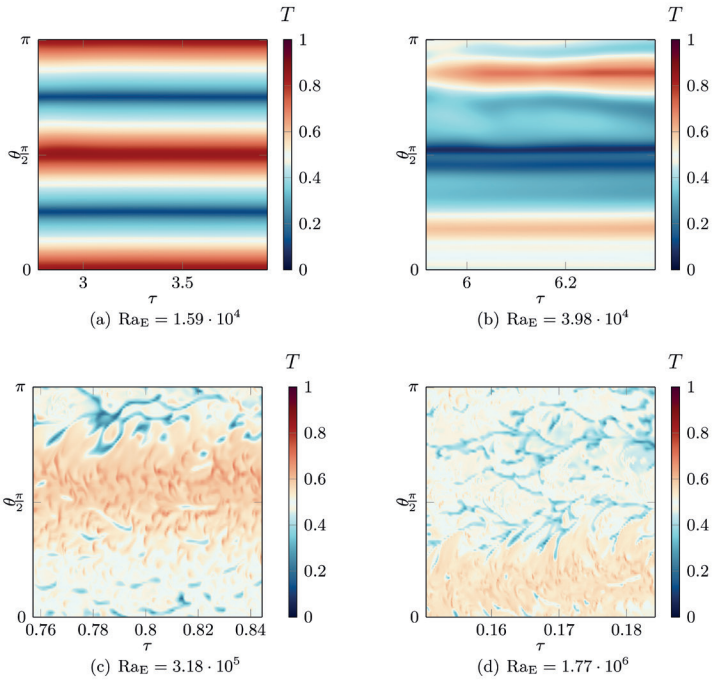

(a) $\mathrm{Ra_E} = 1.59 \cdot 10^4$ (b) $\mathrm{Ra_E} = 3.98 \cdot 10^4$

(c) $\mathrm{Ra_E} = 3.18 \cdot 10^5$ (d) $\mathrm{Ra_E} = 1.77 \cdot 10^6$

Figure 5.5.: Space-time plots on the Meridian at $r_{3/4}$ and $\varphi = 0$ for rising electric Rayleigh $\mathrm{Ra_E}$ numbers.

oscillating structures are observed in the equatorial plane shown in Figures 5.4(a) and 5.4(b). The hot fluid region on the investigated equatorial radius remains stationary, with no movement of the hot fluid region along the angular axis over time. The only difference between those Rayleigh numbers are the smaller structures occurring in Figure 5.4(b), showing the stronger forcing of the DEP force splitting apart the large plume to become smaller ones.

The next space-time plot in Figure 5.4(c) shows significant temperature variations over time. Notably, two adjacent bands of hot and cold fluid propagate as time progresses. The hot fluid band is consistently located at $\varphi = \pi/2$ and $\varphi = 3\pi/2$. Conversely, the cold band is observable at approximately $\varphi \approx 0$ and $\varphi \approx 2\pi$, which are nearly the same positions.

The final equatorial space-time plot in Figure 5.4(d) also shows fluctuating structures over time. Clustered bands of hot and cold fluid remain over the time axis, similar to what is observed in Figure 5.4(c). However, the bands are even more scattered in this case, and cold fluid presence is found within the predominantly hot region. Additionally, this contour's colour contrast is less pronounced than in the previously processed case, indicating a greater temperature mixing. This suggests that fluid mixing significantly increases for larger electric Rayleigh numbers.

Figure 5.5 depicts a view along the Meridian at $\varphi = 0$ from the Pole-to-Pole cut. As illustrated for the first Raleigh number in Figure 5.5(a), there is no variation in temperature over time. Additionally, this Figure is identical in the range $[0, \pi]$ to the previously seen plot of the Equator in Figure 5.4(a), showing the symmetric distribution of the plumes.

In the presented in Figure 5.5(b) for electric Rayleigh number $\mathrm{Ra_E} = 3.98 \cdot 10^4$, a slight drift over time is noticeable, but it is of low magnitude. Compared to Figure 5.5(a), the hot and cold regions are much more randomly distributed along the Meridian. This is further evident in the emergence of smaller structures inside the large-scale plume structure.

The Figure 5.5(c) also shows for the electric Rayleigh number $\mathrm{Ra_E} = 3.18 \cdot 10^5$ the scattered nature of the flow at this level of forcing. A significant band of fluid is observed in the equatorial region around $\theta = \pi/2$. Also, the hot and cold vacillation distribution is similar between the pre-seen equatorial plane and the current azimuthal plane.

The final Figure 5.5(d) also shows similar behaviour seen before in Figure 5.4(d). The vacillation distribution and magnitude are close, indicating that, for all seen cases, the DEP force acts equally over the sphere.

In conclusion, the flow displays uniformly shaped, time-invariant structures at lower electric Rayleigh numbers. However, as voltage and temperature increase, the flow becomes asymmetric, and the pattern becomes more random. This gives rise to sheet patterns and small-scale structures and leads to irregular behaviour. Additionally, convection intensifies and mixing increases due to the larger area exhibiting a temperature of $T = 0.5$. This observation will be explored quantitatively in the following section.

5.2.2 Heat transfer and scaling

After qualitatively examining some example cases, this section now explores integrals such as the Nusselt number and kinetic energy across the entire parameter space depicted in Figure 5.6.

First, the Nusselt number is plotted against the electric Rayleigh number in Figure 5.6(a). As the electric Rayleigh number increases, the Nusselt number also rises, indicating that the heat flux is enhanced due to the increasing forcing from the temperature gradient and the electric field in the simulation. This aligns with previous observations that the fluctuating structures promote greater fluid mixing, thereby improving convective heat transfer.

Notably, within a specific electric Rayleigh number combination, one electric Rayleigh number corresponds to four different temperature parameters, γ_e. As shown in the scope view, the higher temperature factor γ_e results in a slightly higher Nusselt number.

Furthermore, a linear regression function is presented, which is derived from Moores work is included [114],

$$\mathrm{Nu} \sim \mathrm{Ra}_\mathrm{E}^{1/3}. \tag{5.8}$$

This power law is relevant for heat transfer in Rayleigh-Bénard flows. But also, Grossmann et al. [115] reviewed thermal convection for the Prandtl number in order $\mathcal{O}(\mathrm{Pr}) = 10$, the relation seen in eq. (5.8). Despite the heterogeneous nature of TEHD convection compared to natural convection, the Nusselt number scales in a manner analogous to the forcing.

A similar analysis is conducted for the averaged kinetic energy displayed over the electric Rayleigh number in Figure 5.6(b). The results show that kinetic energy increases with rising electric Rayleigh numbers, which is attributed to greater fluctuations in the flow. As with the previous analysis, a linear data regression is made. The first proposition for a linear fit is given by

$$\tilde{E}_\mathrm{kin} = 0.04\,\mathrm{Ra}_\mathrm{E}. \tag{5.9}$$

However, a power law was also considered since the linear fit is slightly misaligned. This power law is defined as

$$\tilde{E}_\mathrm{kin} = 0.0075\,\mathrm{Ra}_\mathrm{E}^{1.155}. \tag{5.10}$$

In conclusion, kinetic energy does not scale linearly with the applied forcing from DEP. The procedure to make the velocity dimensionless in eq. (2.30) is the exact definition as the Peclet number $\mathrm{Pe} = |\mathbf{u}^*|$. To obtain the Reynolds Re number from the Peclet

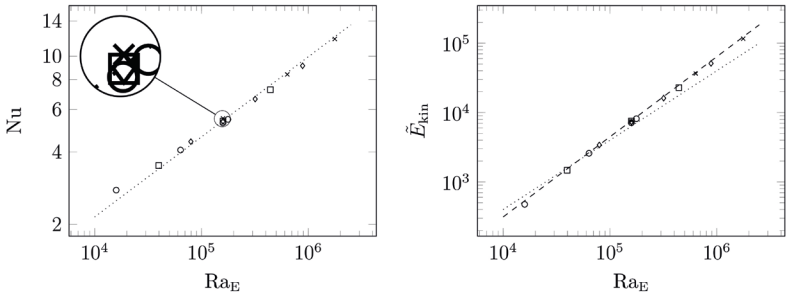

(a) (b)

Figure 5.6.: Plots of (a) Nusselt number at the inner boundary with power law $\mathrm{Nu} \sim \mathrm{Ra_E^{1/3}}$(·····), (b) volume, and time-averaged kinetic energy in the domain with power law $\tilde{E}_{\mathrm{kin}} = 0.04\,\mathrm{Ra_E}$(·····) and $\tilde{E}_{\mathrm{kin}} = 0.0075\,\mathrm{Ra_E^{1.155}}$(- - -) for rising electric Rayleigh number $\gamma_{\mathrm{e}} = 0.006$ (○), $\gamma_{\mathrm{e}} = 0.015$ (□), $\gamma_{\mathrm{e}} = 0.03$ (◇), $\gamma_{\mathrm{e}} = 0.06$ (×) .

number Pe, it must be multiplied by the inverse Prandtl number

$$\mathrm{Re} = \mathrm{Pr}^{-1}\mathrm{Pe}. \tag{5.11}$$

For the compared Nusselt number power law in eq. (5.8) Grossmann et al. [115] also proposed a power law for the dimensionless velocity expressed as the Reynolds number defined as follows

$$\mathrm{Re} \sim \mathrm{Ra}^{4/9}\mathrm{Pr}^{-2/3} \tag{5.12}$$

The relationship mentioned above has been reformulated into the current definition of kinetic energy. Since the Prandtl number remains constant over the range of the electric Rayleigh number, it can be ignored in this context. The reformulated expression proposed by Grossmann is as follows

$$\tilde{E}_{\mathrm{kin}} \sim \mathrm{Ra}^{8/9}. \tag{5.13}$$

The slope is close to what is found using TEHD convection in eq. (5.10); however, the power with DEP forcing is greater than 1, indicating that with a rising electric Rayleigh

number, slightly more energy is induced in the system compared to natural convection analysis.

5.3 Discussion

This section discusses the current work's results in relation to the previous project, GeoFlow. It then examines the impact of thermal boundary coupling with the electric field. Finally, a link between natural convection and TEHD flows within a spherical system is established.

5.3.1 Results in contrast to GeoFlow

The previous sections presented isosurfaces and space-time plots that illustrate the nature of convection, whether it is stable or exhibits irregular, chaotic behaviour as a function of the electric Rayleigh number. Since the AtmoFlow project is an extension of the GeoFlow project, it is beneficial to compare the current results with the work of Futterer et al. [57], who conducted a numerical investigation on GeoFlow. In the GeoFlow study, the boundary condition was isothermal, which aligns with the formulation of the current section. A key difference between GeoFlow and AtmoFlow is their aspect ratios. This variation in aspect ratio results in differences in the electric field, directly affecting the dielectrophoretic force. Consequently, this leads to a different critical threshold for the electric Rayleigh number [54]. To address the difference, it is recommended to normalise the electric Rayleigh number by the critical electric Rayleigh number, known as the criticality

$$\sigma = \frac{\mathrm{Ra_E}}{\mathrm{Ra_E^{crit}}} - 1 \tag{5.14}$$

also done by Yoshikawa et al. [6].

According to the research by Travnikovs et al. [54], the critical electric Rayleigh number for GeoFlow with an aspect ratio of $\eta = 0.5$ is defined as $\mathrm{Ra_E^{crit}}(\eta = 0.5) = 623.5$. In contrast, for the current formulation, with an aspect ratio of $\eta = 0.7$, it is $\mathrm{Ra_E^{crit}}(\eta = 0.7) = 1.203 \cdot 10^3$.

In the studies conducted by Travnikov et al. [54] and Futterer et al. [57], the definition of the electric Rayleigh number differs slightly from the one used in this thesis. Their definition of electric Rayleigh $\mathrm{Ra_{E,Futterer}}$ is equal to

$$4\mathrm{Ra_E} = \mathrm{Ra_{E,Futterer}} = \frac{2\epsilon_0\epsilon_\mathrm{r}\gamma_\mathrm{e}V_0^2}{\rho_0\nu\kappa}. \tag{5.15}$$

This definition has a factor of 4 difference compared to the one used in this work. The reason behind this discrepancy is that Futterer et al. used a static electrical field by solving the temperature-independent Gauss equation and implementing it in the DEP force. The gradient on the squared electrical field results in number 4 in the numerator. Multiplying it by $1/2$ in the DEP force results in the 2 in the numerator in Futterer et al.'s definition.

Emerging convective pattern in TEHD convection compared to other aspect ratios

A comparison of the patterns to the work of Futterer et al. [56] is presented for the initial electric Rayleigh numbers shown in 5.2(a), specifically for $\sigma(\eta = 0.7) = 12.22$. This case is in a steady state, which facilitates the comparison. As previously noted, the shape in this initial case resembles a square-like pattern.
For the scenario where $\sigma(\eta = 0.7) = 12.22$, the work of Futterer et al. [56] provides a case with a closely related electric Rayleigh number of $\sigma(\eta = 0.5) = 7.02$. The simulation displayed in Figure 5.7(a) reveals a different mode output due to different initial field calculations, where the solution starts from another before processing a lower electric Rayleigh number. The second mode outcome where the field is initiated at zero, illustrated in Figure 5.7(b), exhibits a similar square pattern and mode $m = 6$, which aligns with the current setup and result observed in the current work shown in Figure 5.2(a).

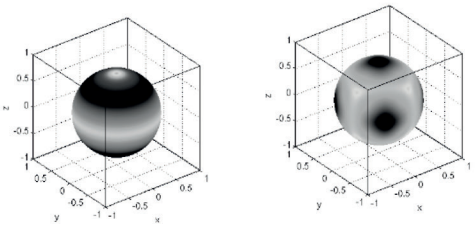

(a) (b)

Figure 5.7.: Thermal convection pattern in GeoFlow result for criticality $\sigma = 8.02$ (a) first mode pattern and (b) second mode pattern, reproduced from Futterer et al. [56], with the permission of IOP Publishing. ©IOP Publishing Ltd. Original content licensed under CC BY-NC-SA.

For the higher electric Rayleigh number $\mathrm{Ra_E} = 3.98 \cdot 10^4$ presented in Figure 5.2(b), a close comparison with previous cases is not feasible because the research by Futterer

does not include additional contour data. A notable difference between the cases with electric Rayleigh numbers $\mathrm{Ra_E} = 1.59 \cdot 10^4$ and $\mathrm{Ra_E} = 3.98 \cdot 10^4$ is the number of plumes observed (refer to Figure 5.2(a) and Figure 5.2(b)). In the first case ($\mathrm{Ra_E} = 1.59 \cdot 10^4$), there are six plumes, while the second case has only five.

As the electric Rayleigh number increases, the visible pattern becomes less distinct, resulting in isolated clusters of hot and cold fluid. This indicates a decrease in the number of prominent visible structures. Szabo et al. [13] illustrate that the mode of visible patterns initially rises from the onset until it reaches a threshold, after which it begins to decline. This behaviour of reducing modes is also evident in these spherical structures. However, the current study does not explore the rise of mode patterns as seen in [13], as it would require parameters much closer to the onset. It is important to note that the lowest electric Rayleigh number $\mathrm{Ra_E} = 1.59 \cdot 10^4$ has the criticality $\sigma > 12$, which is well above the onset. When comparing other works like those from Yoshikawa et al. [6, 41] or from Travnikov et al. [42], the mode analysis takes place principally in the near onset region, which is below $\sigma < 2$.

Nusselt number in comparison to kinetic energy

Another study conducted by Futterer et al. [59] investigates the heat flux resulting from TEHD convection. This study is related to the GeoFlow experiment, where the aspect ratio is set at $\eta = 0.5$. The resulting Nusselt number, correlating with the kinetic energy from the applied forcing, is illustrated in Figure 5.8. As the kinetic energy increases, the Nusselt number also rises.

The same figure also shows the Nusselt number from the present work concerning the resulting kinetic energy. The time-averaged Nusselt number remains consistent across the selected kinetic energy levels despite variations in the aspect ratio. Therefore, in spherical TEHD convection with isothermal boundary conditions, the Nusselt number is directly linked to the resulting kinetic energy, or in other words, to the resulting oscillating plumes over time, regardless of the aspect ratio.

The change of regular to irregular convection

In Figure 5.9, the regime diagram of Futterer et al. [57] is compared to the current work. The investigated simulated electric Rayleigh numbers are represented as vertical black bars. The color in blue indicates stable, time-invariant cases, while green denotes the transition towards irregular flow and red presents irregular time-dependent states. The processed simulations from Futterers and the current work have similar criticality levels

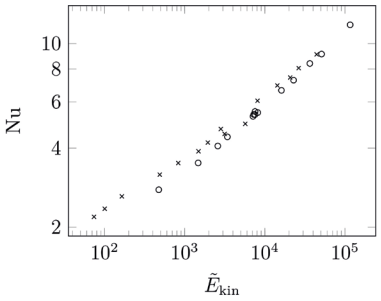

Figure 5.8.: Nusselt number in spherical TEHD convection for (GeoFlow (×) simulation and current work (○)).

for the three distinct regimes. First, until $\mathcal{O}(\sigma) = 10$, the resulting patterns are steady. Then, above $\sigma > 20$, they become irregular or at least time-variant for the current work. A slight offset in the transient region has been observed. Simulations from Futterer et al. indicate that irregular occurs at $\sigma = 19$, whereas the current study shows time-variant patterns at $\sigma = 32$.

Firstly, the definitions of stable and irregular behaviour are rather arbitrary since Futterer's work does not present any time-related plots, such as space-time diagrams. This leads to a potential bias in the region where $\sigma = [7 \dots 19]$.

Secondly, Futterer used a static electric field to model the electric Rayleigh number, while the current work employs the Gauss equation coupled with temperature. A detailed analysis of the influence of the thermal boundary on the onset has not been done yet. The research from Travnikov et al. [42] showed this for cylindrical geometries. Since cylinders and spheres do not have the same curvature effect on the electric field, the absolute values for critical electric Rayleigh numbers cannot be compared. However, the critical electric Rayleigh number trend dependent on the thermal factor should be

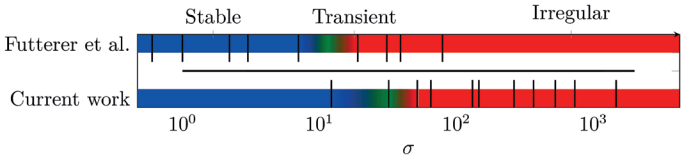

Figure 5.9.: Convective states between the GeoFlow experiment by Futterer et al. [57] and present work given by the criticality σ.

similar. The presence of a rising thermal boundary tends to raise the critical electric Rayleigh number. As a result, incorporating a thermally coupled electric field delays the onset of transience, leading to transient cases appearing at higher electric Rayleigh numbers in the thermal-dependent Gauss equation.

5.3.2 Consideration of the temperature-dependent Gauss in spherical geometries

This section analyses the increase in Nusselt number observed in Figure 5.6(a) at the same electric Rayleigh number for rising thermo-electric parameter γ_e. As previously mentioned, the effect of the thermo-electric parameter has not been thoroughly explored in spherical geometries. Therefore, the precise reason for the increase in the Nusselt number cannot be definitively established; however, an analytical solution based on the isothermal conductive base state is provided for investigation.

As shown in Table 5.1, the Nusselt number rises slightly with increasing thermo-electric parameter. In contrast, when the electric Rayleigh number is increased by a factor of 10, the Nusselt number does not exhibit a significant change with a tenfold increase in the thermo-electric parameter.

The thermo-electric parameter, alongside curvature, is the second factor influencing the electric field. To illustrate the variation in electric field magnitude, Figure 5.10 displays the electric field for different aspect ratios over the gap width without any thermal influence. This is defined by the following equation:

$$\mathbf{E}_\mathrm{b}(r) = \frac{\eta}{(1-\eta)^2}\frac{1}{r^2}\mathbf{e}_r \tag{5.16}$$

This equation is derived by solving the temperature-independent Gauss equation, $\boldsymbol{\nabla}\cdot\mathbf{E} = 0$. Note that the radius is adjusted so that they all start at the same value for different aspect ratios.

Next, Figure 5.10(b) presents the electric field across the gap width for various thermo-electric parameters at $\eta = 0.7$ for the conductive base state, as defined in eq. (4.6).

Table 5.1.: Nusselt number over thermo-electric parameter γ_e at electric Rayleigh number $\mathrm{Ra_E} = 1.59 \cdot 10^5$.

γ_e	$6 \cdot 10^{-3}$	$15 \cdot 10^{-3}$	$15 \cdot 10^{-3}$	$60 \cdot 10^{-3}$
Nu	5.285757	5.36835	5.372592	5.51596

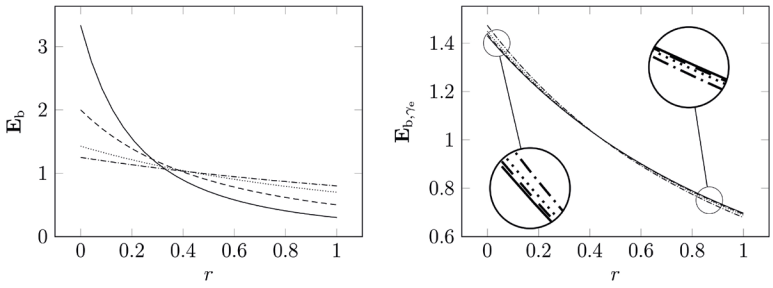

(a) (b)

Figure 5.10.: Non-dimensional electrical field over normed gap width for (a) aspect ratio variation $\eta = 0.3$ (——), $\eta = 0.5$ (- - -), $\eta = 0.7$ (·····) and $\eta = 0.8$ (- · - ·) and (b) thermal variation $\gamma_\mathrm{e} = 0.006$ (——), $\gamma_\mathrm{e} = 0.015$ (- - -), $\gamma_\mathrm{e} = 0.030$ (·····) and $\gamma_\mathrm{e} = 0.06$ (- · - ·) for $\eta = 0.7$.

When made dimensionless in accordance with eq. (2.30), the expression becomes

$$\mathbf{E}_{\mathrm{b},\gamma_\mathrm{e}}(r) = -\eta \frac{\gamma_\mathrm{e}}{\ln(1-\gamma_\mathrm{e})} \left(\frac{1}{1-\eta}\frac{1}{r}\right)^2 \left[1 - \gamma_\mathrm{e} T_\mathrm{b}(r)\right]^{-1} \tag{5.17}$$

The temperature $T_\mathrm{b}(r)$ for the conductive base state can be retrieved from eq. (4.14).

The change in the electric field due to curvature is significantly greater than that caused by thermal variation. In Figure 5.10(b), it is not immediately clear which plotted electric field exhibits the overall higher magnitude. For instance, with $\gamma_\mathrm{e} = 0.06$, the electric field is higher at $r = 0$, but it remains below all other thermo-electric parameters at $r = 1$.

To improve the visualisation, the electric field is integrated over the gap width. The values are all close to one due to the normed integral over the gap size of one. To highlight the variations, the integral is adjusted by subtracting the integral of the thermal independent base state electric field

$$\int_{\eta/(1-\eta)}^{1/(1-\eta)} \mathbf{E}_\mathrm{b}\,\mathrm{d}r = 1, \tag{5.18}$$

such as in the expression

$$var(\mathbf{E}) = \int_{\eta/(1-\eta)}^{1/(1-\eta)} \mathbf{E}_{\mathrm{b},\gamma_\mathrm{e}}\,\mathrm{d}r - \int_{\eta/(1-\eta)}^{1/(1-\eta)} \mathbf{E}_\mathrm{b}\,\mathrm{d}r. \tag{5.19}$$

Table 5.2.: Integral of electric field along the radius, excluding the temperature-independent electrical field resulting in $var(\mathbf{E})$ for various aspect ratios and thermo-electric parameters.

γ_e \ η	0.3	0.5	0.7
$6 \cdot 10^{-3}$	$5.834\,82 \cdot 10^{-8}$	$2.075\,56 \cdot 10^{-9}$	$-6.877\,75 \cdot 10^{-11}$
$15 \cdot 10^{-3}$	$5.9805 \cdot 10^{-8}$	$2.160\,91 \cdot 10^{-9}$	$-6.675\,78 \cdot 10^{-11}$
$30 \cdot 10^{-3}$	$6.236\,45 \cdot 10^{-8}$	$2.313 \cdot 10^{-9}$	$-6.2477 \cdot 10^{-11}$
$60 \cdot 10^{-3}$	$6.802\,88 \cdot 10^{-8}$	$2.658\,59 \cdot 10^{-9}$	$-4.981\,59 \cdot 10^{-11}$

The results are presented for different aspect ratios and thermo-electric parameters in Table 5.2. It can be observed that for $\eta = 0.7$, the electric field increases slightly with rising thermo-electric parameters, which may contribute to an increase in the Nusselt number as γ_e rises seen in Table 5.1.
A similar behaviour is noted when comparing the other aspect ratios ($\eta = 0.5$) and ($\eta = 0.3$). Further work needs to verify the analytical finding using numerical methods and expand it to the proposed aspect ratios.

5.3.3 Spherical TEHD convection compared to natural convection

The following section briefly discusses the differences between natural convection and convection resulting from the DEP force. While the TEHD convection has already been compared to a natural buoyancy in section 5.2.2, the figures presented in the current section provide a clear overview for spherical shells.
Starting with natural convection, the force is defined as $\rho\,\mathbf{g}$. In this context, hot fluid has a lower density, which, when combined with the gravitational field, results in a greater upward force in warmer regions. The simulation conducted by Ouertatani et al. [116] serves as a well-established benchmark for natural convection in a unit cell. As shown in Figure 5.11(a), the vector starting from the hot region from the left is more significant than from the lower temperature on the right. This imbalance of upward forces causes the hot fluid to rise on the left, resulting in a rotating cell.
To better visualise this effect, the simulation was reprocessed using OpenFOAM. And the buoyancy driven force vector $\rho\mathbf{g}$ plotted in Figure 5.11(b), which is consistent with the Figure 5.11(a) seen before. Now to better visualise where this force imbalance takes place, the mean force $\overline{\rho\mathbf{g}}$ vector is subtracted to the quiver field, acting as the actual driven force magnitude and direction. Figure 5.11(c) shows an upward-oriented force for the hot region, while on the cold side, the vectors are oriented downward. Note here

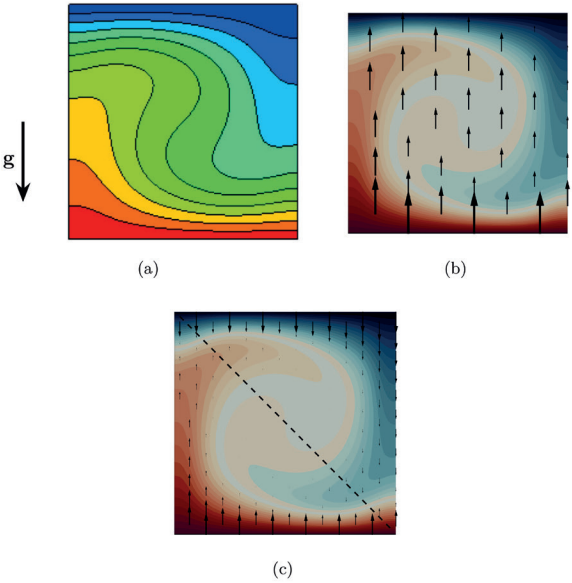

Figure 5.11.: Example of natural convection triggered cell in a differentially heated rectangular cavity, (a)reproduced from Ouertatani [116] published and granted by Elsevier Masson SAS. (b) numerical simulation a hot room cavity with quiver $\rho\mathbf{g}$ (c) numerical simulation of a hot room cavity with quiver $\rho\mathbf{g} - \overline{\rho\mathbf{g}}$ and dashed symmetry line.

that the vectors are symmetrically oriented to the dashed line. The hot region acts in the same way upward as the cold region downward.

For TEHD flows, the analogy is slightly more complex. The dielectric forcing, as defined in eq. (2.25), is influenced by both the magnitude of the electric field and the temperature gradient, represented by the relationship $\mathbf{f}_{\mathrm{DEP}} \sim \mathbf{E}^2\boldsymbol{\nabla}T$ for a chosen fluid. The other scaling factors involve material properties such as thermal diffusivity or viscosity, which remain constant for the investigated parameter space and, therefore, do not impact the local scaling or the orientation of the force vector.

Figure 5.12(a) illustrates the vector and magnitude orientation of $\mathbf{E}^2\boldsymbol{\nabla}T$ on a clipped equatorial temperature slice, corresponding to the case shown in the earlier Figure 5.2(a).

The hot and cold plumes are clearly visible; however, the orientation of the vectors does not align well with the direction of the plumes. Notably, at the base of the hot plume, the vectors even point in opposing directions, creating difficulty in observing the force imbalance that leads to the actual convection.
Fortunately, the dielectrophoretic force can be divided into two components: a static part that is comparable to hydrostatic pressure in natural convection, and a dynamic part. This concept was introduced by Hart et al. [52], which can be expressed mathematically as follows:

$$\mathbf{f}_{\mathrm{DEP}} = \frac{1}{2}\mathbf{E}^2\boldsymbol{\nabla}\epsilon = \underbrace{\frac{1}{2}\boldsymbol{\nabla}(\mathbf{E}^2\epsilon)}_{\mathbf{f}_{\mathrm{DEP,stat}}} \underbrace{-\frac{1}{2}\epsilon\boldsymbol{\nabla}\mathbf{E}^2}_{\mathbf{f}_{\mathrm{DEP,dyn}}}. \tag{5.20}$$

In this case, Figure 5.12(b) shows the dynamic part of the electrophoretic force, which immediately orients along the electric field direction. Moreover, in the hot plume region, the vectors are slightly more prominent than in the colder region, causing an imbalance in the flux responsible for the convection of the plume. Besides the inner area, the vectors along the radius remain close to the same size, all oriented outward. Since the fluid is incompressible, the force compensates itself on a selected radius.
In the work by Yoshikawa et al. [41], a mean force was defined, which subtracts from the dynamic component of the dielectrophoretic force. This leads to a force perturbation that is necessary to trigger convection. This is expressed in terms of a selected radius as follows

$$\mathbf{f}'_{\mathrm{DEP,dyn}} = \mathbf{f}_{\mathrm{DEP,dyn}} - \overline{\mathbf{f}_{\mathrm{DEP,dyn}}} \tag{5.21}$$

where $\overline{(\dots)}$ represents the mean value over the selected radius. In Figure 5.12(c), the local force perturbation scales with the electric field and temperature. This behaviour is similar to natural convection, where hot fluid is expelled outward while cold fluid moves toward the inner boundary. It is important to note that the force vectors near the inner boundary of the hot plume exhibit a greater magnitude than those at the cold plume near the outer boundary. This discrepancy arises from the stronger electric field close to the inner boundary, as illustrated in Figure 5.10. Therefore, the colder plume, oriented radially inward, is more closely related to a secondary flow from the hot plume, which ensures conservation of continuity. This asymmetric force distribution is a key difference in creating the convection compared to the natural convection seen before.

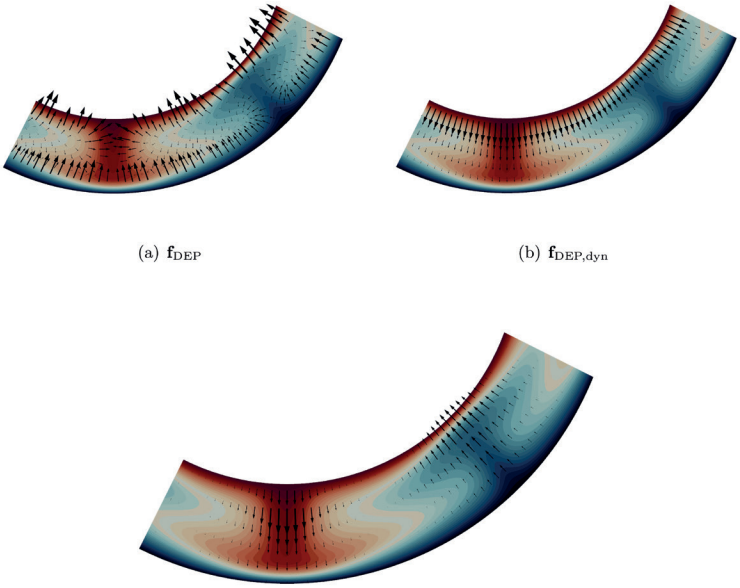

(a) $\mathbf{f}_{\mathrm{DEP}}$ (b) $\mathbf{f}_{\mathrm{DEP,dyn}}$

(c) $\mathbf{f}'_{\mathrm{DEP,dyn}}$

Figure 5.12.: Representation from whole force to static and dynamic part of the dielectrophoretic force $\mathbf{f}_{\mathrm{DEP}}$ as quiver and the evolution along a plume on part section of the temperature field.

5.4 Summary

This section investigates TEHD convection in spherical shell geometries. As the electric Rayleigh number increases, the flow pattern transitions from plume-like structures to sheet-like formations, ultimately resulting in only small, irregular, vacillating structures. The time evolution over the space is also shown, marking the heterogeneous evolution of the flow resulting from strong DEP forcing. The ratio of convective to conductive heat flux, measured by the Nusselt number, is also present, as well as the volume- and time-averaged kinetic energy. The power law eq. (5.8) used in Rayleigh-Bénard convection

represents the evaluation of the Nusselt number for rising DEP forcing well, underlining the good compatibility between natural convection and spherical TEHD convection according to the transport of heat. For the kinetic energy, a power law is proposed in 5.10 and eq. (5.9), marking that the kinetic energy does not increase proportionally with the forcing. Compared to the natural convection's power law in eq. (5.13), one sees the exponent greater than one for TEHD convection and lower than one for natural convection.

Despite the different aspect ratios compared to results from GeoFlow, similar patterns are observed, and the stability threshold is only slightly offset. This offset is possibly attributed to the implementation of the Gauss equation, which provides a more accurate temperature-coupled electric field and helps to mitigate instability in this investigation. Furthermore, the range of parameters explored in this study allows for much larger forcing compared to those used in GeoFlow.
The effect of the Gauss equation on the higher becoming Nusselt number with rising thermo-electric parameter is analysed. The influence of the temperature affecting the electric field is considerably lower than the effect of the curvature shown via an analytic solution at a conductive base state.

Finally, a comparison is made between natural convection in a cavity and TEHD convection between spherical shells. The homogenous force field from gravity induces a symmetrical force imbalance on cold and hot areas. TEHD convection, however, results from a radius-dependent electric field that decreases significantly with increasing radius. This results in strong DEP forcing in the hot fluid at the inner shell. The cold areas in the outer region see less forcing; the cold plume oriented radially inward results more from the continuity conservation of the radially outward-oriented hot plume.

6 Non-isothermal spherical Taylor-Couette flow

This chapter focuses on simulations with inner and outer non-isothermal boundary conditions that involve differential rotation. Given that the effects of differential rotation can vary significantly based on factors such as rotation rates, fluid properties, and aspect ratios, it is crucial to process the basic flow for the TEHD convection and sTC, respectively. Like the previous section, this will first present qualitative flow results using isosurfaces, followed by a more quantitative analysis.

The results of this work are discussed in relation to existing studies about sTC and the types of heat transfer in sTC.

6.1 Model formulation

The governing equations from section 2.5 are simplified in this section. The numerical case is analysed within a rotating reference frame, which incorporates both centrifugal and Coriolis forces in the governing equation

$$\boldsymbol{\nabla} \cdot \mathbf{u} = 0 \tag{6.1}$$

$$\partial_t \mathbf{u} + (\mathbf{u} \cdot \boldsymbol{\nabla})\mathbf{u} = \boldsymbol{\nabla} p + Pr\, \boldsymbol{\nabla}^2 \mathbf{u} - \mathrm{Pr}\sqrt{\mathrm{Ta}}\, \mathbf{e}_z \times \mathbf{u} - \frac{1}{4}\mathrm{Pr}^2\, \mathrm{Ta}\, \mathbf{e}_z \times (\mathbf{e}_z \times \mathbf{x}) \tag{6.2}$$

$$\partial_t T + (\mathbf{u} \cdot \boldsymbol{\nabla})T = \boldsymbol{\nabla}^2 T \tag{6.3}$$

Solving the Gauss equation is unnecessary since the DEP force $\mathbf{f}_{\mathrm{DEP}}$ is excluded from the investigation. The temperature eq. (6.3) is included but does not correlate with the momentum eq. (6.2). It is processed to compare the heat flux to TEHD convection.

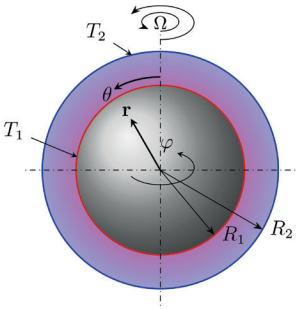

Figure 6.1.: Problem geometry and boundary conditions in non-isothermal sTC.

The inner boundary condition accounts for differential rotation, utilising the rotating wall function provided by OpenFOAM. The Dirichlet boundary conditions detail this

$$\begin{cases} \mathbf{u} = \mathrm{Pr}\,\mathrm{Ro}\,\sqrt{1/4\mathrm{Ta}}\,r\sin(\theta)\mathbf{e}_\varphi, & T = 1, \quad \boldsymbol{\nabla} p = 0, \quad \text{at} \quad r = \dfrac{\eta}{1-\eta} \\ \mathbf{u} = 0, & T = 0, \quad \boldsymbol{\nabla} p = 0, \quad \text{at} \quad r = \dfrac{1}{1-\eta} \end{cases} \tag{6.4}$$

and is schematically shown in Figure 6.1.
The temperature is uniformly applied to the surface of a spherical shell, with the inner shell heated while the outer one is cooled. The parameter range contains all the rotational combinations described in section 4.3.2, see Table 4.3, resulting in 30 parameters, including 6 Taylor numbers and 5 Rossby numbers.

6.2 Results

This section discusses the results obtained from simulations featuring differential rotation. The initial part presents the findings using isosurfaces and space-time plots of several representative examples. Following this, the analysis goes deeper into an integral analysis for the parameter space.

6.2.1 Spatial and temporal evolution in non-isothermal sTC

The first case illustrated in the first column of Figure 6.2 corresponds to the lowest boundary of the parameter space for the outer rotating shell and the minimum Rossby number Ro = 0.429 and rotation rate Ta = 110.3. Figures 6.2(a), 6.2(d), and 6.2(g) display the temperature, radial velocity, and meridional velocity, respectively. The tem-

perature exhibits a homogeneous distribution in the azimuthal direction, indicating an axis-symmetric pattern. Noteworthy temperature variations occur primarily in the radial direction, resembling a typical conductive base state, as schematically represented in Figure 6.1. The only notable difference compared to the conductive case is a slight shift in isolines in the equatorial region.
In Figure 6.2(d), the radial velocity indicates an outward-oriented flow in the radial direction within the equatorial region, while near the Poles, the flow is directed inward. This equatorial flow is linked to the previously mentioned broader band of hot fluid.
This set's final Figure 6.2(g), which depicts the meridional velocity, clearly illustrates that fluid from the poles is transported along the inner shell toward the Equator. Subsequently, this fluid returns to the Poles along the outer shell region. The profiles of the velocities maintain a symmetric and stable shape.

In the following case, a much higher Taylor number $\mathrm{Ta} = 2.37 \cdot 10^5$ is considered, as shown in Figures 6.2(b), 6.2(e) and 6.2(h). The Rossby number remains within the parameter space at its lowest value, $\mathrm{Ro} = 0.429$. Figure 6.2(b) illustrates the temperature distribution. On the equatorial plane, a stable hot fluid circular region is observed. The temperature transitions abruptly to colder fluid as it continuously processes radially outward. This is in contrast to the previous case, where the temperature decreases continuously along the radius of the equatorial plane. In the Pole-to-Pole slice, hot fluid accumulates in a tangent cylinder, marked by the white dashed line, around the rotation axis. Cold fluid is present both inside and outside the tangent cylinder.
Figure 6.2(e) shows the radial velocity, where an increase in velocity in outward orientation in the radial direction of fluid is noticeable in the equatorial region, which also comes to a sudden stop by a certain radius. In comparison, the remaining inward-oriented flow at the Pole is more widely distributed and not as concentrated in the polar region as in Figure 6.2(d).
The final figure, referenced as Figure 6.2(h), illustrates the meridional velocity. Here, the axially upward and downward-oriented flow responsible for the tangent cylinder is well visible. The hot fluid from the inner shell process radially continues axially, creating this cylindrical shape in the temperature isosurface in Figure 6.2(a). This tangent cylinder is referred to as a Stewartson-like pattern in this work due to its resemblance, despite the differing Taylor and Rossby numbers required for this type of pattern.

The final example case in the third column of Figure 6.2 is selected with the highest Taylor number $\mathrm{Ta} = 6.37 \cdot 10^5$ and the highest Rossby number $\mathrm{Ro} = 1.14$. Figures 6.2(c), 6.2(f), and 6.2(i) illustrate the temperature, radial velocity, and meridional velocity,

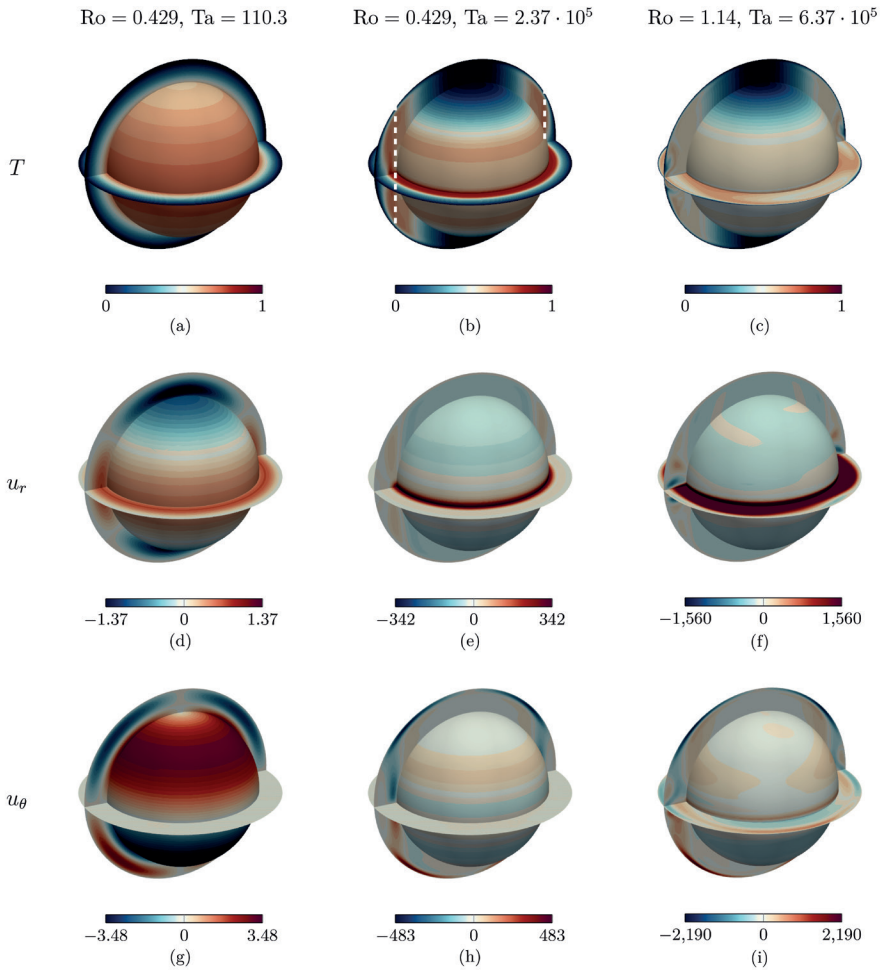

Figure 6.2.: Isosurface plots of temperature, T, radial velocity, u_r, and meridional velocity, u_θ, are shown in the top, middle, and bottom rows, respectively, across equatorial, meridional, and radial cross-sections on a spherical shell located at a quarter-radius $r_{1/4}$. Colour scales are provided below each panel. From left to right, the plots increase Ta and Ro incrementally.

respectively. The tangent cylinder, noted in previous cases, is no longer discernible. It looks blurred in the isosurface of the temperature over the gap width. An asymmetry is observed between the lower and upper equatorial regions, and the equatorial slice exhibits some variation in the azimuthal direction.

For the radial velocity in Figure 6.2(f), the outward-oriented radial velocity keeps a significant velocity until the outer shell. The flow in the equatorial cut is no longer rotationally symmetric in the azimuthal direction.

Finally, the meridional velocity 6.2(i) displays wavy patterns in the region near the Equator. Consequently, the case is no longer symmetric in either the meridional or azimuthal directions.

Space-time analysis

The Figure 6.3 presents space-time for temperature on the Equator with radius $r_{3/4}$. The first case in Figure 6.3(a) at Ro = 0.429 and Ta = 110.3 displays a completely homogeneous plane in both the time and spatial directions, indicating that no time variation is observed in the azimuthal direction, resulting in a steady-state, axis-symmetric case.

Figure 6.3(b) presents the following space-time plots for a Taylor number of $2.37 \cdot 10^5$. Similarly to the previous Figure 6.3(a), there are no fluctuations in the contour, indicating that the system is both time-invariant and space-invariant on this plane.

Figure 6.3(c) displays the equatorial space-time plot for Ro = 1.14 and Ta = $6.37 \cdot 10^5$. Here, diagonal hot fluid lines are observed, with two diagonal structures appearing slightly grouped. This hotter fluid diagonal originates from a vortex alternating in the radial direction, as seen in prior 6.2(c). The inner rotating sphere sweeps away the vortex, periodically moving it around the rotation axis.

Figure 6.4 shows the space-time plot for temperature on the Meridian at the same radius $r_{3/4}$. A time-varying pattern cannot be distinguished in the first Figure 6.4(b). However, a slightly brighter spot appears in the meridional location at $\theta = \pi/2$, which corresponds to the Equator. The thicker region of hot fluid, previously observed in Figure 6.2(a), is associated with this brighter spot on the space-time plot.

Figure 6.4(b) illustrates that temperature variation is noticeable across different angles θ in the meridional direction. The temperature is near zero in the polar regions at $\theta \approx 0$ and $\theta \approx \pi$. Additionally, the equatorial region at $\theta = \pi/2$ remains cold. Only the areas around $\theta = \pm\pi/4$ display a region of hot fluid, which originates from the Meridian traversing the previously discussed tangent cylinder. Importantly, the distribution of

hot and cold regions remains constant along the Meridian over time, and no fluctuations are detected. Therefore, this case can be characterised as a steady-state situation.
In Figure 6.4(c), the temperature in time on the Meridian reveals the vortex visible on the equatorial plane, identified at $\theta = \pi/2$ as a wave propagating over time. Additionally, slightly off-centred from the Equator, colder fluid can be observed, alternating periodically with the hot fluid.

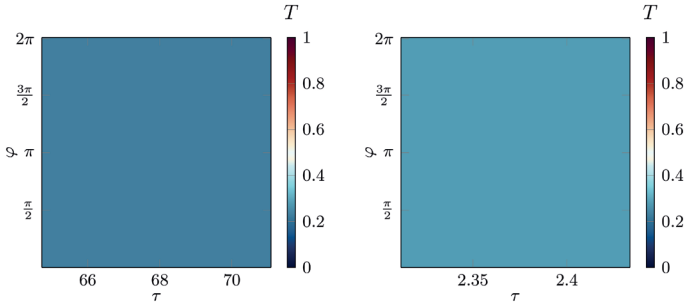

(a) Ro = 0.429, Ta = 110.3

(b) Ro = 0.429, $2.37 \cdot 10^5$

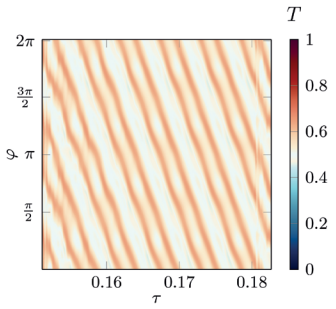

(c) Ro = 1.14, Ta = $6.37 \cdot 10^5$

Figure 6.3.: Space-time plots on the Equator at $r_{3/4}$ and $\theta = \pi/2$ for rising differential rotation.

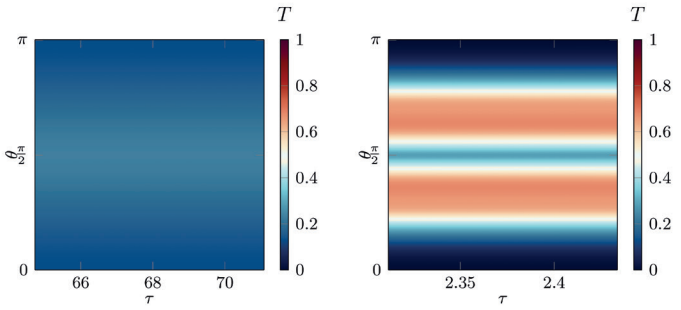

(a) Ro = 0.429, Ta = 110.3 (b) Ro = 0.429, $2.37 \cdot 10^5$

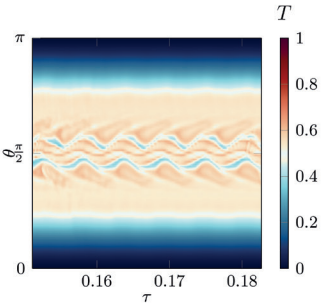

(c) Ro = 1.14, Ta = $6.37 \cdot 10^5$

Figure 6.4.: Space-time plots on the Meridian at $r_{3/4}$ and $\varphi = 0$ for rising differential rotation.

6.2.2 Velocity profiles in non-isothermal sTC

The plots in Figure 6.5 show the radial velocity. The velocity is retrieved along a radius on the equatorial slice and is then time-averaged. The radius r is normalised to the dimensional gap width to better visualise the profiles instead of using $r = \eta/(1-\eta)$ and $r = 1/(1-\eta)$. Figure 6.5(a) starts with the smallest Taylor number in the parameter range, Ta = 110.3, for the respective Rossby numbers. The radial velocity in these cases results in bell-shaped curves that are nearly symmetric around the mid-gap. As the Rossby number increases, the maximum magnitude of the radial velocity also rises, but the overall bell shape of the curve remains unchanged.

Similar patterns are observed in the following two cases, depicted in Figure 6.5(b) and Figure 6.5(c), which correspond to the Taylor numbers Ta = 600.6 and Ta = $4.42 \cdot 10^3$, respectively. The bell shape of the curves is still evident; the only difference is that the magnitude of the radial velocity increases with both the Taylor number and the Rossby number.

The Taylor number is set at Ta = $3.31 \cdot 10^4$ in Figure 6.5(d). A noticeable change in shape occurs for the smaller Rossby numbers, specifically from Ro = 0.429 to Ro = 1.04. The location of maximum radial velocity shifts to the left compared to previous Taylor numbers. Instead of the previously observed nearly symmetric bell shape, with the maximum occurring at the mid-gap ($r \approx 0.5$), the maximum radial velocity for Ro = 0.429 is now found at $r = 0.4$. Further increases in the Rossby number lead to diminished shifts in this location. For Ro = 1.04, the maximum velocity occurs at $r = 0.45$, which is closer to the mid-gap. This maximum location remains unchanged for the given Taylor number at the highest Rossby number Ro = 1.14.

Previously, Figure 6.2(e) showed that the radial outwards oriented velocity on the equatorial cut drops at a certain radius. Current plots provide a more precise depiction of the radial velocity distribution on the equatorial plane. Figure 6.5(e) illustrates the radial velocity for a Taylor number of $2.37 \cdot 10^5$, while Figure 6.5(f) represents the Taylor number Ta = $6.37 \cdot 10^5$ across chosen Rossby numbers. The velocity increases on the inner side of the gap due to the sphere giving momentum to the fluid. Since the fluid cannot pass the outer sphere, the velocity becomes zero at the outer sphere, where $r = 1$, to satisfy the boundary condition. However, the velocity distribution varies significantly with different Rossby numbers. Both plots reveal a substantial plateau of negligible radial velocity for $r > 0.5$ following the peak from the radial outward-oriented flow for the smallest Rossby number. The behaviour is similar for Rossby number Ro = 0.708, but the plateau is smaller. In this case, the radial velocity does not have a significant magnitude after $r > 0.7$.

The plateau becomes indistinguishable for a Rossby number Ro $\geq$ 0.939. The velocity decreases in the outer sphere region. In these cases, the velocity reduction is linked to the permeable definition of the outer shell.

Figure 6.6 displays the angular velocity ω over a radius r on the equatorial slice, which is then time-averaged. All plots are normalised to the rotation of the inner sphere, allowing them to overlap if the angular velocity behaves similarly across the normed radius $r \in [0, 1]$. The velocity is measured in the rotating reference frame, which means the velocity is zero for all simulations at the outer radius. Additionally, the angular

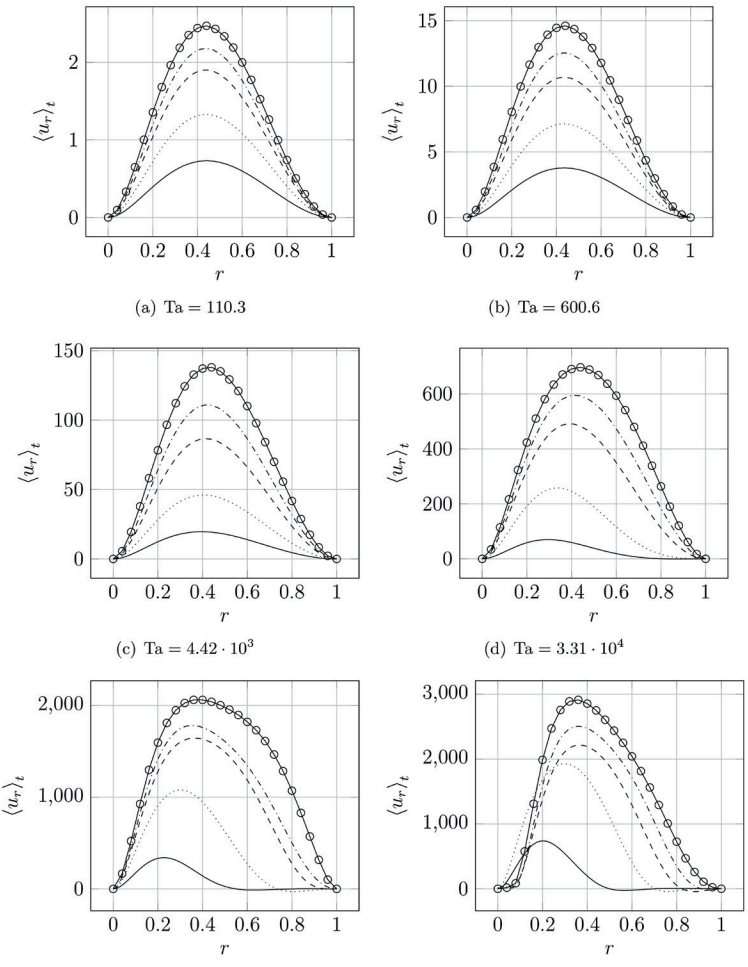

(a) Ta = 110.3

(b) Ta = 600.6

(c) Ta = $4.42 \cdot 10^3$

(d) Ta = $3.31 \cdot 10^4$

(e) Ta = $2.37 \cdot 10^5$

(f) Ta = $6.37 \cdot 10^5$

Figure 6.5.: Time-averaged radial velocity along the radius for $\varphi = 0$ on the equatorial plane at given Taylor and Rossby number Ro = 0.429 (——), Ro = 0.708 (·····), Ro = 0.939 (- - -), Ro = 1.04 (-·-·), Ro = 1.14 (—o—).

velocity from cylindrical Stokes flow, as written by Eckhardt et al. [76],

$$\omega_{\text{Stokes}}(r) = \frac{1}{1-\eta^2}\left[-\eta^2 + \left(\frac{\eta/(1-\eta)}{r+\eta/(1-\eta)}\right)^2\right] \tag{6.5}$$

is included for each Taylor number. This comparison aids in understanding when the equatorial azimuthal velocity no longer conforms to Stokes flow. The Stokes flow defines the flow when the viscous flow dominates over the convective flow.

The shapes of Figures 6.6(a), 6.6(b), and 6.6(c) are quite similar. The angular velocity ω decreases closely with the Stokes flow for increasing radius. In Figure 6.6(c) for $\text{Ro} = 0.429$, the angular velocity for the first time is significantly lower than the velocity from the Stokes flow.

The slope begins to differ from the Stokes flow for the cases shown in Figure 6.6(d) at a Taylor number of $\text{Ta} = 3.31 \cdot 10^4$. The solid line representing the Rossby number at $\text{Ro} = 0.429$ shows an even more rapid decrease in magnitude. After the fast descent, it reaches a more moderate decrease radius of $r = 0.65$. In contrast, for a higher Rossby number, such as $\text{Ro} = 0.706$, the threshold extends to a larger radius of $r = 0.7$. The three remaining cases, which exhibit even higher Rossby numbers, converge at a radius of $r = 0.9$, just before the outer radius. At this point, they show a negligible amount of angular velocity. All curves remain situated below the cylindrical Stokes flow.

Figures 6.6(e) and 6.6(f) for the two remaining Taylor numbers, $\text{Ta} = 2.37 \cdot 10^5$ and $\text{Ta} = 6.37 \cdot 10^5$, also exhibit some similarities. Notably, the velocity reaches the rapid descent area for the lowest Rossby number, $\text{Ro} = 0.429$, in the mid-gap area at $r = 0.5$. A similar pattern is observed for the Rossby number $\text{Ro} = 0.706$, which reaches zero around $r = 0.7$. In contrast to the previous case, the three remaining Rossby numbers indicate that the angular velocity even dips below zero at some points, suggesting that it falls slightly below the outer rotational boundary before increasing again to meet the outer rotating speed.

To conclude the observations from Figures 6.5 and 6.6, at low Taylor numbers, specifically up to $\text{Ta} = 4.42 \cdot 10^3$, the radial velocity at the Equator behaves symmetrically, and the angular velocity approximates that of cylindrical Stokes flow. However, Stokes flow is no longer observed beyond this threshold. For cases with high Taylor number $\text{Ta} \geq 2.37 \cdot 10^5$ and low Rosby number, this lack of observed angular velocity leads to decreasing angular momentum in the flow, which induces the radial velocity to decrease faster.

To preserve the continuity, the flow on the equatorial surface where the radial velocity comes to a stop needs to deviate away from the equatorial surface. This was visible in

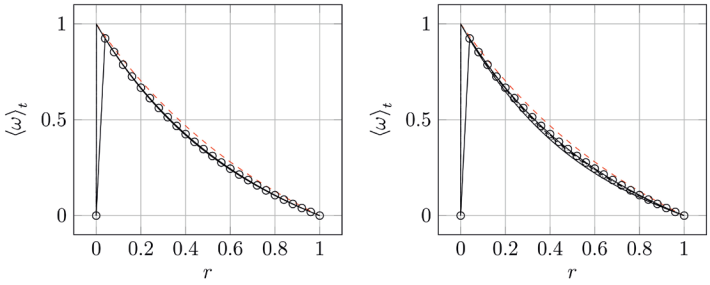

(a) Ta = 110.3

(b) Ta = 600.6

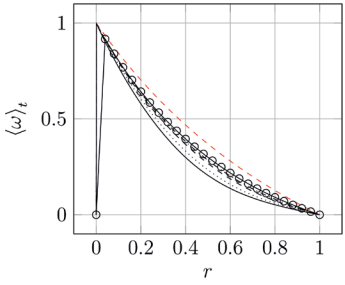

(c) Ta = $4.42 \cdot 10^3$

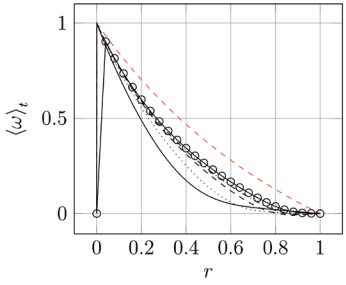

(d) Ta = $3.31 \cdot 10^4$

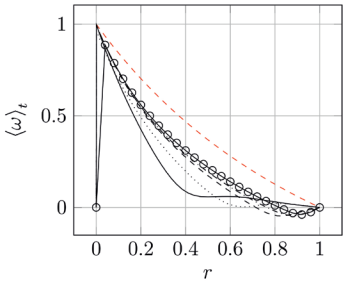

(e) Ta = $2.37 \cdot 10^5$

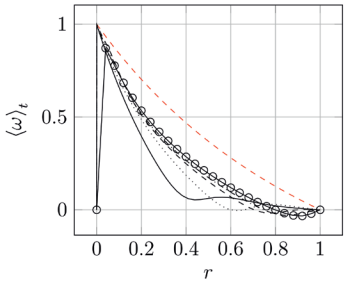

(f) Ta = $6.37 \cdot 10^5$

Figure 6.6.: Time-averaged angular velocity along the radius for $\varphi = 0$ on the equatorial plane at given Taylor and Rossby number Ro = 0.429 (——), Ro = 0.708 (·····), Ro = 0.939 (- - -), Ro = 1.04 (- · - ·), Ro = 1.14 (—o—), Stokes cylindrical flow (- - -).

Figure 6.2(h), where the axial upward and downward oriented flow creates the tangent cylinder seen in Figure 6.2(b).

For the higher Rossby numbers, the radial and angular velocities remain strong in the outer gap region of the equatorial slice. This significant push of the flow on the outer sphere is probably the cause of the flow becoming transient, showing a wavy pattern on the equatorial slice as seen in Figures 6.2(c) and 6.3(b).

6.2.3 Convective heat transfer in sTC

Figure 6.7(a) illustrates the Nusselt number at the inner boundary for the product of the Taylor and Rossby numbers defined earlier (see eq. (4.11)). The Nusselt number increases with an ascending rotation rate. The plot indicates that the convective heat flux rises significantly for small increases in rotation. However, with further increases in rotation, an asymptotic behaviour emerges, leading to a slower increase in heat flux. A power law

$$\mathrm{Nu} \sim (\varpi)^{1/4} \tag{6.6}$$

is proposed for this plot, represented by the dashed line.

An analogous analysis is conducted for the kinetic energy within the system. Figure 6.7(b) shows the kinetic energy as a function of the rotation rates ϖ where the slope

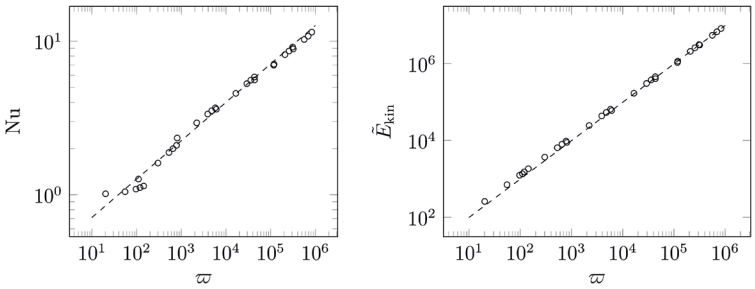

Figure 6.7.: Plots of (a) Nusselt number at the inner boundary with power law $\mathrm{Nu} \sim (\varpi)^{1/4}$ (- - -), and (b) volume, and time-averaged kinetic energy in the domain with linear regression $\tilde{E}_{\mathrm{kin}} = 0.5989\,\varpi$ (- - -) for rising differential rotation ϖ.

behaves linearly as defined

$$\tilde{E}_{\mathrm{kin}} = 0.5989\,\varpi. \tag{6.7}$$

This is because the defined rotation directly contributes kinetic energy to the system. In contrast, the power law from TEHD convection displayed a slight offset, highlighting a less perfect linear relation between the boundary conditions' forcing and the energy within the system. For differential rotation, linear regression yields the following relationship represented by the dashed line.

6.3 Discussion

This section first compares the current results' non-linearity to an analytical approach used to simulate current flows. Next, the stability of the processed cases is compared to existing numerical work for differentially rotating spheres. Finally, the investigation focuses on the source of heat transport between the previously processed TEHD convection and the newly analysed differentially rotating cases.

6.3.1 The non-linear nature of sTC flow

To better analyse the flow of sTC, the idea is to use an angular momentum flux Nusselt number Nu^{ω} as defined by Eckhardt et al. [76] as

$$\mathrm{Nu}^{\omega} = \frac{J^{\omega}}{J^{\omega}_{\mathrm{lam}}} \tag{6.8}$$

where J^{ω} defines the angular momentum flux and $J^{\omega}_{\mathrm{lam}}$ the laminar momentum flux. For cylindric geometries, the laminar momentum flux is analytically defined as

$$J^{\omega}_{\mathrm{lam,cyl}} = 2\nu R_1^2 R_2^2 \frac{\Omega_1 - \Omega_2}{R_2^2 - R_1^2}. \tag{6.9}$$

The goal is to establish a single scalar value for sTC that provides insights into the nature of the current flow, as Eckhard did. This section will discuss the non-linear behaviour of sTC flow, highlighting the challenges in defining $J^{\omega}_{\mathrm{lam}}$ for spherical geometries using analytic solutions.

Munson et al. [93, 94, 95] described a Pseudo-Analytic Solution (PAS) that can be applied to any flow in differentially rotating spheres. The approach is based on a linear perturbation analysis developed using a series of Legendre polynomials. Munson demonstrates

that the problem, which includes an integral that may not have an analytic solution, can be transformed into a system of ordinary differential equations (ODEs). This enables a numerical solution that is both more stable and efficient, without compromising the integrity of the analytic formulation.

Munson [117] developed a Fortran77 code to solve this ODE using discrete points in the radial and meridional directions. For convenience, this code has been reimplemented in Python, utilising state-of-the-art boundary problem solvers, and it is published on GitHub[1].

To demonstrate the differences between the analytic solution and the numerically processed case, four scenarios are compared. The analytic solution employs a series expansion. It was found that the differences between polynomial orders $N_t = 5$ and $N_t = 9$ are negligible. The Rossby number is maintained at $\mathrm{Ro} = 0.429$, which is the lowest value within the current parameter space.

The Taylor number is subsequently increased, with the first case for the Taylor number $\mathrm{Ta} = 110.3$ illustrated in Figure 6.8(a), showing results that closely match Munson's analytic solution. The contours maintain a similar shape across all three velocity components, with only slight differences in their absolute values. For instance, the radial velocity from the analytic solution is marginally higher in the equatorial region. The meridional velocity for the analytic solution is also slightly elevated in the mid-latitude area, while the azimuthal velocity remains consistent between both approaches.

Figure 6.8(b) presents the results for the same Rossby number with a Taylor number of $\mathrm{Ta} = 600.6$. These results are comparable to those obtained with the previously selected Taylor number; however, the agreement differs, particularly concerning the radial velocity contours in the polar region. Although the velocity magnitudes from both methods are close, the analytic contours still exhibit higher values for both radial and meridional velocities. Instead of round-shaped contours, the azimuthal velocity contour in the current work shows a flat region in the polar areas, suggesting the onset of non-linear effects.

[1] DRACULA code on GitHub: `https://github.com/AtmoFlow/DRACULA`

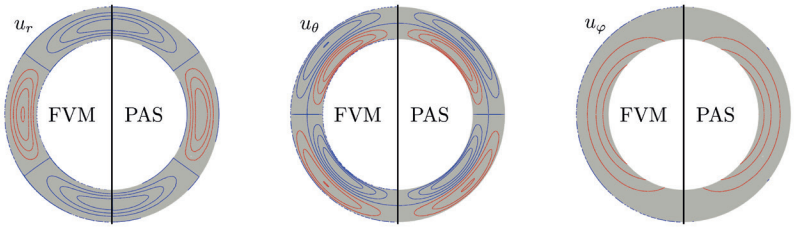

(a) Contour of radial velocity u_r: $u_{r,min} = -1.43(0.36)$, $u_{r,max} = 0.71(0.18)$ and meridional velocity u_θ: $u_{\theta,min} = -3.52(0.88)$, $u_{\theta,max} = 3.52(0.88)$ at $\mathrm{Ta} = 110.3$ and $\mathrm{Ro} = 0.429$

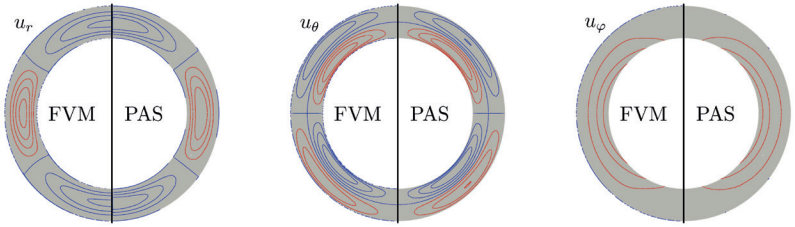

(b) Contour of radial velocity u_r: $u_{r,min} = -6.90(1.72)$, $u_{r,max} = 3.37(0.84)$ and meridional velocity u_θ: $u_{\theta,min} = -16.9(4.23)$, $u_{\theta,max} = 16.9(4.23)$ at $\mathrm{Ta} = 600.6$ and $\mathrm{Ro} = 0.429$

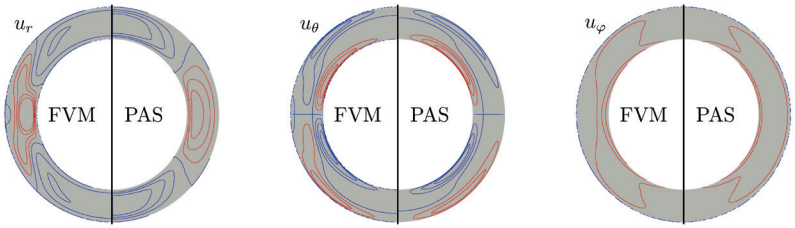

(c) Contour of radial velocity u_r: $u_{r,min} = -49.3(12.3)$, $u_{r,max} = 27.7(6.92)$ and meridional velocity u_θ: $u_{\theta,min} = -191.6(47.9)$, $u_{\theta,max} = 191.6(47.9)$ at $\mathrm{Ta} = 3.31 \cdot 10^4$ and $\mathrm{Ro} = 0.429$

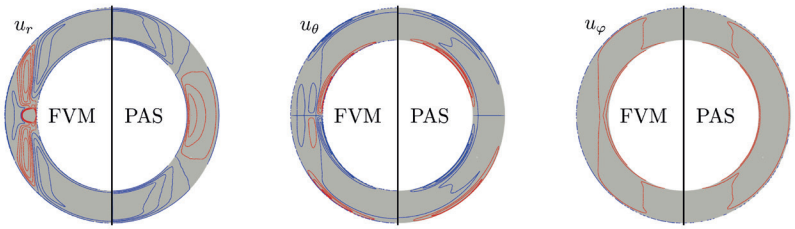

(d) Contour of radial velocity u_r: $u_{r,min} = -105.7(26.4)$, $u_{r,max} = 72.2(18.0)$ and meridional velocity u_θ: $u_{\theta,min} = -859.0(214.7)$, $u_{\theta,max} = 859.0(214.7)$ at $\mathrm{Ta} = 6.37 \cdot 10^5$ and $\mathrm{Ro} = 0.429$

Figure 6.8.: Contours of radial u_r, meridional u_θ and azimuthal u_φ velocities comparing the numerical results beside the pseudo-analytic solution proposed by Munson.

As the rotation speeds increase, as shown in Figure 6.8(c), the contours become increasingly heterogeneous. The radial velocity from the OpenFOAM simulation indicates a stagnation at the equatorial plane, a phenomenon also noted in the results of Figure 6.5 for the low Rossby number Ro = 0.429. In contrast, the analytic solution does not exhibit any shape changes for the radial velocity in the equatorial region. The meridional and azimuthal velocities present straight vertical profiles in the current work. In the mid-gap region, the meridional velocity either moves directly upward or downward, depending on the hemisphere.
The final Taylor number in this set, $6.37 \cdot 10^5$, highlights significant differences between the FVM simulation and the analytical solution shown in Figure 6.8(d). While the analytical solution attempts to represent a substantial outward-oriented radial velocity in the equatorial region, this work's results indicate an equatorial-like jet flowing outward in the equatorial zone. Additionally, the Stewartson-like pattern, which appears as a tangent cylinder in the meridional and azimuthal velocity, is even more pronounced in the current work. In contrast, the analytical solution fails to display any of these patterns.

In conclusion, the PAS for a spherical system deviates significantly at higher rotation rates, even for laminar steady-state cases, which signifies the PAS cannot capture nonlinear effects in sTC. It is worth noting that the series order required to resolve at least the low rotation case is relatively high, resulting in a fifth-order polynomial. Conversely, the definition of laminar angular momentum is straightforward for cylindrical systems. Given that the analytical solution diverges notably at medium rotation rates (Ta = $3.31 \cdot 10^4$), defining an angular momentum flux Nusselt number that provides reliable results across a broad range of rotations becomes challenging. The flow's nature diverges significantly, even in steady-state scenarios. This shift is further highlighted by the previous Figure 6.6, where the angular velocity rapidly diverges from the Stokes flow necessary in the approach used by Eckhardt et al. [76] for TC.
To ensure the accuracy of the FVM simulation results, these cases are verified using the commercial software COMSOL and the Pseudo Spectral Method (PSM) code MagIC, as detailed in section A.3.

6.3.2 Steady states and transient results in sTC flow

Wicht [20] investigated both co-rotating and counter-rotating sTC flows. The stability of these simulations is summarised in a regime diagram included in Wicht's study[20]. He defines a dimensionless outer rotation parameter, Ω, and a dimensionless relative

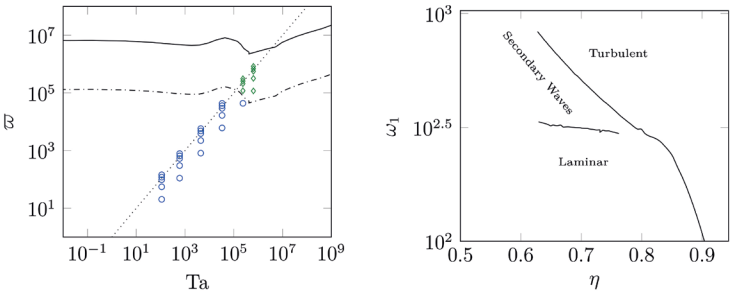

Figure 6.9.: Plots showing the (a) regime diagram adapted from Wicht [20] with the Stewartson stability $\varpi = \mathrm{Ta}$ line (·····), transient separation line (——), current work supposed transient separation line (-·-·-), current work stable case (○) and transient periodic case (◇) and (b) regime diagram adapted from Egbers and Rath [88] showing the margin to transient flows for inner sphere angular velocity, subjected to the aspect ratio.

outer rotation, $\Delta\Omega$. For clarity, this regime diagram has been updated in Figure 6.9(a) using current work dimensionless numbers[2]. The simulations from the current work are additionally plotted in Figure 6.9(a). The stationary rotation symmetric cases are indicated as ○, while the periodic transient cases are marked as ◇.

The Stewartson stability line is plotted from Wicht's regime diagram. The transient separation line outlines the region where differential rotation begins to exhibit transient solutions. The exact critical differential rotation can be extracted from Table 1 in Wicht's original study.

The current work identified transient cases for $\mathrm{Ta} = 2.37 \cdot 10^5$ and $\mathrm{Ta} = 6.37 \cdot 10^5$. The respective critical differential rotation is on the order of magnitude $\mathcal{O}(\varpi) = 1 \cdot 10^6$. However, the highest differential rotations observed for the selected Taylor numbers are $\varpi = 3.08 \cdot 10^5$ and $\varpi = 8.28 \cdot 10^5$, respectively, and these cases are also transient. Consequently, the differential cases in the current work remain below the separation line for transient cases defined by Wicht.

It is important to note a significant difference in the aspect ratios between Wicht's study and the current work. Wicht's investigation considered simulations using an aspect ratio

[2]The conversion is achieved using the formulas $\mathrm{Ta} = 4\Omega^2$, where Ω represents the dimensionless outer rotation number defined by Wicht, and $\varpi = 4\Delta\Omega^2$, where $\Delta\Omega$ is the relative dimensionless rotation also defined by Wicht.

of $\eta = 0.35$. While the author is not aware of any prior literature examining the steady-state limits of co-rotating, differentially rotating spheres concerning aspect ratio, Egbers and Rath [88] did analyse the transient flow concerning aspect ratio for a single rotating sphere. Although the specific rotation levels at which transient flows occur, as found in Egbers and Rath's work, cannot be directly compared to co-rotating differential rotation, a general trendline related to the aspect ratio can be observed when the flow becomes transient as secondary waves or turbulent flow. For slow rotating flow $\mathrm{Ta} \approx 0$ and $\varpi > 0$, the solution behaves similarly to a uniquely inner rotating flow [118].
This trend is illustrated in Figure 6.9(b), which shows that the rotation speed required to make the flow transient decreases as the aspect ratio increases. Therefore, the flow becomes transient at higher aspect ratios and lower differential rotation, accounting for the early transient flows observed despite remaining below the transient threshold set by Wicht. A proposed transient separation line for the current aspect ratio is indicated in Figure 6.9(a) marked as the dash-dotted line. This is not entirely verified since the parameter space does not cover the line range.

6.3.3 Dominant actor for the thermal exchange in sTC flow

The section 6.2.3 demonstrated how the Nusselt number at the wall evolves with increasing Taylor number and Rossby number. It showed that kinetic energy rises with higher rotation speeds, which is directly related to the boundary conditions. Both were done in the previous chapter when uniquely TEHD convection was analysed.
Currently, the focus shifts to understanding how the selected force, DEP force or forces from sTC transport heat. Since the boundary conditions between the two simulation chapters are entirely different, and the electric Rayleigh number $\mathrm{Ra_E}$ cannot be directly compared to the rotation rate ϖ, a common scaling quantity related to the Nusselt number. Because convective heat transfer is directly linked to velocity, kinetic energy is the common chosen variable for the next investigation in these heterogeneous cases.

Figure 6.10 compares the Nusselt number related to kinetic energy involving the DEP force only and the Nusselt number resulting from sTC only.
The first subfigure, 6.10, illustrates the Nusselt number at the inner wall for increasing. For both sets of simulations, the power law is processed. First, for the case with purely DEP forcing

$$\mathrm{Nu} = 0.4567\, \tilde{E}_{\mathrm{kin}}^{0.2774} \tag{6.10}$$

and then for sTC only

$$\mathrm{Nu} = 0.2427\, \tilde{E}_{\mathrm{kin}}^{0.2419}. \tag{6.11}$$

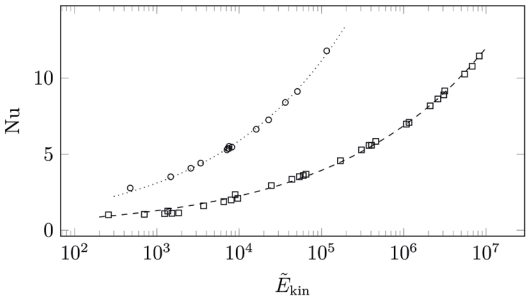

Figure 6.10.: Nusselt number over kinetic energy at the inner wall for TEHD (○) convection with power law $\mathrm{Nu} = 0.4567\,\tilde{E}_{\mathrm{kin}}^{0.2774}$ (·····) and sTC flow (□) with power law $\mathrm{Nu} = 0.2427\,\tilde{E}_{\mathrm{kin}}^{0.2419}$ (- - -).

The TEHD convection exhibits a superior Nusselt number for the same amount of kinetic energy as sTC. The power law factor from eq. (6.10) are also higher than in eq. (6.11).

The in-flow Nusselt number Nu^q (see eq. (4.18)) is introduced to provide further insights. A detailed explanation can be found in section 4.4.1, with its derivation included in Appendix A.4. This Nusselt number is equivalent to the Nusselt number defined in eq. (4.17) at the wall. Furthermore, the heat flux normal to the inner sphere must equal the flux at the outer sphere, as there are no additional heat sources or sinks within the spherical gap. Consequently, the in-flow Nusselt number level remains constant at any radius for time-averaged quantities.

This constant characteristic of the Nusselt number allows for the separation of the in-flow Nusselt number into a convective term, defined as $\mathrm{Nu}^q_{\mathrm{conv}} = \frac{(\eta-1)^2}{\eta} r^2 \langle u_r T \rangle_{A,t}$, and a conductive term, expressed as $\mathrm{Nu}^q_{\mathrm{cond}} = \frac{(\eta-1)^2}{\eta} r^2 \langle -\partial_r T \rangle_{A,t}$.

For both forces, DEP and resulting from sTC, the respective Nusselt number is plotted against kinetic energy in Figures 6.11(a) and 6.11(b). The Nusselt number is obtained from a sphere at the midgap, defined as

$$r_{1/2} = (1+\eta)/(2-2\eta) \tag{6.12}$$

Figure 6.11(a) shows notable similarities to the results from the Nusselt number measured at the inner wall seen in Figure 6.10. In the TEHD convection cases, a higher Nusselt number related to convective flow is observed for a similar amount of kinetic

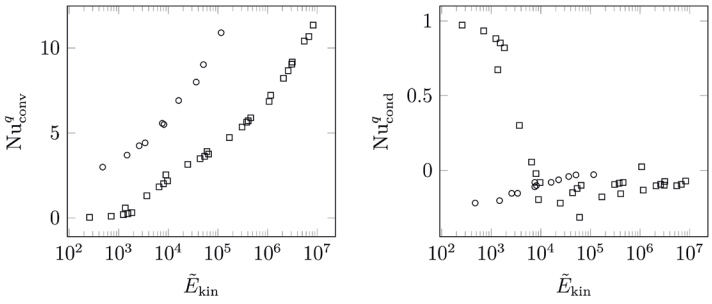

Figure 6.11.: In-flow Nusselt Nu^q sepparated in (a) the convective part $\mathrm{Nu}^q_{\mathrm{conv}}$ the and (b) conductive part $\mathrm{Nu}^q_{\mathrm{cond}}$ at radius $r_{1/2}$ for TEHD convection (○) and sTC flow (□).

energy. Since the definition of the Nusselt number, in terms of aspect ratio η and the investigated radius r, is consistent across all cases, the increased Nusselt number for TEHD convection can be attributed to the higher radial velocity that transports warmer fluid the radial outward direction, as defined by the variable term $u_r T$. While TEHD convection distributes its heat flux uniformly across the sphere, the differential rotation is confined to the equatorial region, necessitating a much higher rotation rate to achieve a similar level of heat transfer.

Regarding flow patterns, the TEHD convection is plume-dominated from the inner to the outer sphere. In contrast, the radially outward-oriented flow from sTC only occurs in the equatorial region, representing the main contribution to the Nusselt number observed. Additionally, it is significant that for the low-rotation case where $\tilde{E}_{\mathrm{kin}} < 10^4$ in Figure 6.11(b), the conductive component plays a significant positive role in transferring heat from the inner to the outer sphere. In contrast, for TEHD convection, the conductive part is negligible or even has a negative contribution, reversing the heat flow from the outer shell to the inner shell. For these low-rotation cases, conductive heat transfer is the dominant mechanism. However, once a threshold is exceeded, the heat flux also begins to have a convective nature for the differential rotating parameters.

6.4 Summary

The current sections present simulations of non-isothermal sTC. Similar to the previous section, the flow details are provided for increasing rotation rates. The resulting pattern and the time-dependent flows are identified. The flow is dominated by a radial outward-oriented flow at the Equator and an inward-oriented flow at the Poles. As the rotation rate increases, the tangent cylinder is identified, and the flow becomes time-dependent, resulting in an equatorial vortex as the rotation rate continues to increase. The periodic recurring patterns are well recognised in the space-time plots.

The radial and angular velocity profiles on the equatorial cut along various the radius are shown, demonstrating the deviation from cylindrical Stokes flow. The rapid attenuation of angular velocity for low Rossby numbers and higher Taylor numbers shows a linked lack of angular momentum, resulting in a rapidly decreasing radial velocity in those cases. To maintain continuity, the flow separates on the equatorial cut, proceeding axially up and down, creating the tangent cylinder.
The velocity profiles exhibit non-linear behaviour as the rotation rate increases. This non-linearity is further illustrated by comparing the FVM to the PAS. The FVM differs significantly from the PAS results at rising rotation rates. The outcomes of this investigation highlight the complexity of describing differentially rotating flows. It is particularly challenging to define a single value to characterise a regime state analogous to the angular momentum Nusselt number defined by Eckhard in cylindrical geometries. Furthermore, the current chapter shows that the aspect ratio affects the margin where the flow becomes transient. An estimation is made that for a higher aspect ratio, the flow becomes transient at lower Taylor and Rossby numbers. This necessitates further investigation in the future to define the exact thresholds.

The increasing Nusselt number and kinetic energy are plotted for the increasing rotation, and the power law eq. (6.6) and eq. (6.7) are proposed. They are compared to the power laws found for TEHD convection, and the dominant heat transport mechanism is shown via the in-flow Nusselt number. The cases with TEHD convection show higher heat transport for comparable kinetic energy in sTC. Furthermore, in cases of low rotation rates, sTC primarily transports heat through conduction, while TEHD is dominated by convective heat transfer within the selected parameter space.

7 TEHD convection in spherical Taylor-Couette flow with meridional isothermal boundary conditions

This chapter combines TEHD convection with sTC. It first shows the model formulation, followed by the presentation of flow results through isosurfaces depicting temperature and radial and meridional velocity. The Nusselt number and kinetic energy resulting from the flow are then illustrated, along with a discussion of transient effects in the second part. Additionally, a regime diagram is proposed in the discussion section.

7.1 Model formulation

Current simulations now incorporate differential rotation with TEHD convection. This means all equations from section 2.5 are necessary, starting with the continuity equation, followed by the momentum equation with centrifugal, Coriolis forces and the DEP force density

$$\boldsymbol{\nabla}\cdot\mathbf{u}=0 \tag{7.1}$$

$$\begin{aligned}\partial_t\mathbf{u}+(\mathbf{u}\cdot\boldsymbol{\nabla})\mathbf{u}=&-\boldsymbol{\nabla}P+\mathrm{Pr}\,\boldsymbol{\nabla}^2\mathbf{u}\\&-\mathrm{Pr}\sqrt{\mathrm{Ta}}\,\mathbf{e}_z\times\mathbf{u}\\&-\frac{1}{4}\mathrm{Pr}^2\,\mathrm{Ta}\,\mathbf{e}_z\times(\mathbf{e}_z\times\mathbf{x})\\&-\mathrm{Pr}\,\mathrm{Ra_E}|\mathbf{E}|^2\boldsymbol{\nabla}T.\end{aligned} \tag{7.2}$$

$$\partial_t T+(\mathbf{u}\cdot\boldsymbol{\nabla})T=\boldsymbol{\nabla}^2T \tag{7.3}$$

$$\boldsymbol{\nabla}\cdot[(1-\gamma_e T)\,\mathbf{E}]=0,\quad\text{with}\quad\mathbf{E}=-\boldsymbol{\nabla}\vartheta \tag{7.4}$$

The temperature eq. (7.3) is required to model the temperature advection and diffusion in the domain. Finally, the Gauss eq. (7.4) processes the temperature-dependent electric field in the gap.

Each shell's temperature boundary condition, as schematically shown in Figure 7.1, is uniform, maintaining a constant temperature difference, ΔT. The simulation is processed in the rotating reference frame, and the Taylor number controls the rotation rate. The differential rotation is set by the inner shell rotation velocity, which is defined as

$$\begin{cases} \mathbf{u} = \mathrm{Pr}\,\mathrm{Ro}\,\sqrt{1/4\mathrm{Ta}}\,r\sin(\theta)\mathbf{e}_\varphi, & T=1, \quad \vartheta=1, \quad \boldsymbol{\nabla} p = 0, \quad \text{at} \quad r = \dfrac{\eta}{1-\eta} \\ \mathbf{u} = 0, & T=0, \quad \vartheta=0, \quad \boldsymbol{\nabla} p = 0, \quad \text{at} \quad r = \dfrac{1}{1-\eta} \end{cases} \tag{7.5}$$

The parameters used are a combination of the parameters from the previous chapters. On one side, all electric Rayleigh numbers from Table 4.1 are selected. The second part combines these with all rotation rates from Table 4.3. This approach results in 12 parameters for TEHD convection, specifically 6 Taylor numbers and 5 Rossby numbers. Altogether, this leads to a total of 360 processed simulations.

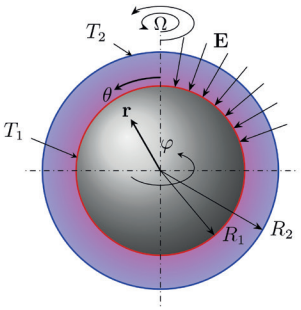

Figure 7.1.: Problem geometry and boundary conditions for TEHD convection in sTC using isothermal boundary conditions.

7.2 Results

This section discusses the results obtained from simulations for TEHD convection combined with flow from sTC. The initial part presents the results using isosurfaces and space-time plots of selected examples. Following this, the analysis continues into an integral parameter space analysis.

7.2.1 Spatial and temporal evolution of rotating TEHD convection

The case present in the first column of Figure 7.2 starts with the lowest electric Rayleigh number $\mathrm{Ra_E} = 1.59 \cdot 10^4$ and the lowest rotation parameters $\mathrm{Ta} = 110.3$ and $\mathrm{Ro} = 0.429$. The observed pattern resembles the previous structures for the basic flow with TEHD convection only. As shown in the temperature isosurface in Figure 7.2(a), three plume structures emerge. Two of these are located at the Poles. The third plume is situated at the Equator; however, this plume spans the entire equatorial plane, resembling the hot fluid band observed in Figure 6.2(a), resulting in an axis-symmetric case.
The radial velocity in Figure 7.2(d) shows fluid flows in a radial outward direction in the equatorial and polar regions. This is also where plumes emerge in Figure 7.2(a). The outward-oriented fluid then separates and transitions to meridional velocity, as demonstrated in Figure 7.2(g). The separated fluid flows toward the Equator from the Poles along the outer shell. Fluid at the Equator moves towards the Poles along the outer shell. Around the latitudes of $\theta = \pi/4$ and $\theta = 3\pi/4$, the two streams of fluid converge and flow inwards to the inner shell, entraining cold fluid and creating a cold plume band at this latitude.

The subsequent case, shown in the second column of Figure 7.2, is set at a electric Rayleigh number of $\mathrm{Ra_E} = 3.98 \cdot 10^4$ and a Taylor number of $\mathrm{Ta} = 600.6$, combined with a Rossby number of $\mathrm{Ro} = 0.708$. This configuration results in a non-axisymmetric simulation due to stronger forces from differential rotation and DEP forcing.
The influence of these parameter sets leads to irregular, vacillating patterns. In Figure 7.2(b), the plumes emerging at the Poles and the Equator remain discernible. However, the plume at the Equator appears wider in the meridional direction compared to the earlier case in Figure 7.2(a). In contrast, the plumes at the poles are narrower and more scattered.
Additionally, the convergence region where the fluid from the radially outward oriented flow at the Equator and Poles merges to return to the inner shell has shifted slightly towards the Poles, approximately $\theta \approx \pi/6$ and $\theta \approx 5\pi/6$. This shift can be observed in the radial velocity at the Pole-to-Pole plane in Figure 7.2(e), as well as in the meridional velocity in Figure 7.2(h).
A new type of pattern has been identified: streaks of hot fluid that exit the equatorial plane and rise towards the Poles. These streaks appear periodically in both hemispheres. For this analysis, this pattern is referred to as the fishbone pattern marked as a white dashed line in Figure 7.2(a). Observations of the radial velocity on the equatorial plane (see Figure 7.2(e)) reveal a slightly higher radial velocity where the fishbone pattern

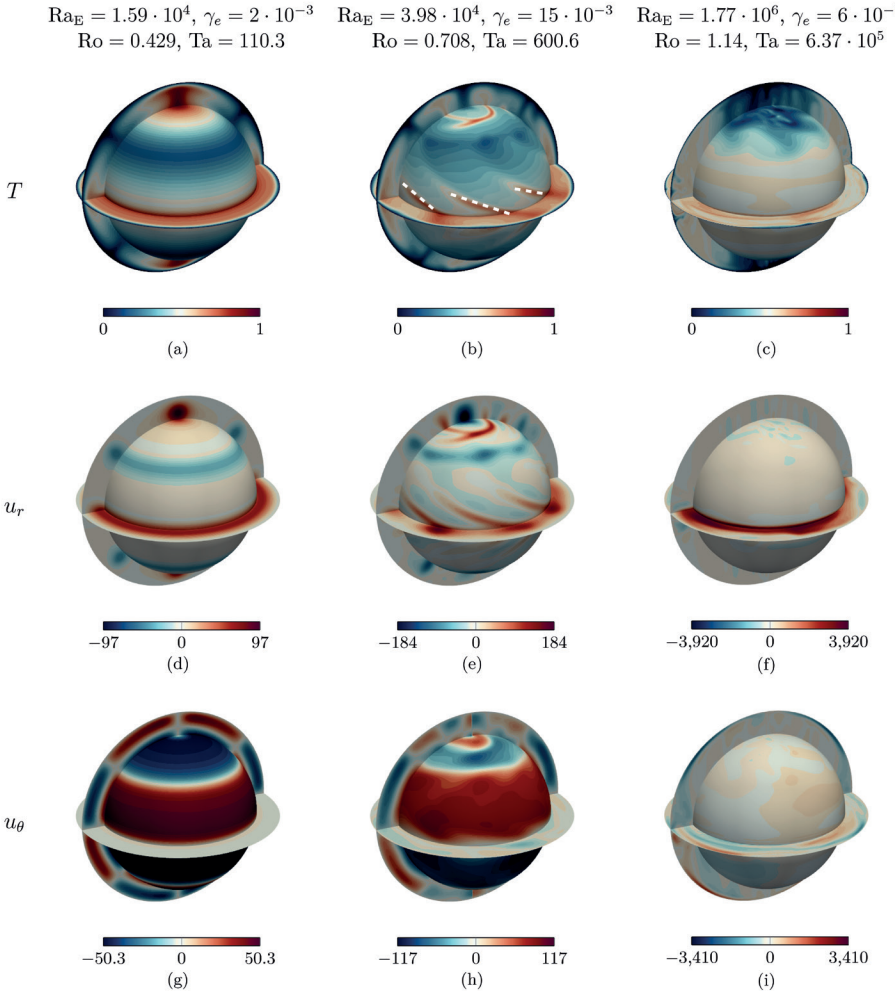

Figure 7.2.: Isosurface plots of temperature, T, radial velocity, u_r, and meridional velocity, u_θ, are shown in the top, middle, and bottom rows, respectively, across equatorial, meridional, and radial cross-sections on a spherical shell located at a quarter-radius $r_{1/4}$. Colour scales are provided below each panel. From left to right, the plots increase $\mathrm{Ra_E}$, Ta, and Ro incrementally.

emerges. Additionally, these fishbone patterns entrain hot fluid from the inner shell, which can be seen on the temperature isosurface, although they are not evident in the meridional velocity.

The third column of Figure 7.2 presents the simulation for the Taylor number $6.37 \cdot 10^5$ and Rossby number $\mathrm{Ro} = 1.14$ combined with the highest electric Rayleigh number $\mathrm{Ra_E} = 1.77 \cdot 10^6$. Overall, the flow shows similarities to the result without TEHD convection depicted in 6.2(c), but has additional scattered patterns in the equatorial region that alternate in the azimuthal direction. In general, the temperature isosurface in Figure 7.2(c) exhibits significantly more fluctuations. Notably, small hot fluid circular occurrences originating from narrow plumes are visible at the Poles, indicating the activity of TEHD convection in this area. Additionally, small cold plumes are observed travelling from the outer sphere to the inner sphere in the equatorial region on the Pole-to-Pole slice.

The radial velocity shown in Figure 7.2(f) indicates a dominant radially outward-oriented fluid flow in the equatorial region. The radial velocity on the equatorial plane is neither axis-symmetric nor does it have a distinct periodic pattern, like the fishbones.

Lastly, the meridional velocity displayed in Figure 7.2(i) still exhibits an alternating pattern visible in the equatorial slice, similar to that observed for the sTC case shown previously in Figure 6.2(i). However, the wave pattern is less distinct, as the overlaying structure from the DEP force adds additional vacillations.

Space-time analysis

Figure 7.3, presents the space-time plots for the previous cases seen in Figure 7.2 for the temperature on the Equator at radius $r_{3/4}$. No temperature change is observed in Figure 7.3(a) over time. Neither changes along the Equator are visible. The temperature of the Equator at this radius is therefore space- and time-invariant.

Figure 7.3(b) reveals oscillating structures where hotter regions appear periodically distributed in the azimuthal direction over time. These hotter areas are linked to the fishbone structures observed in Figure 7.2(b), showing a slight temporal drift.

Figure 7.3(c) shows drifting patterns also observed without TEHD convection in Figure 6.3(c). However, adding the DEP force, the drifting patterns become much more scattered. Additionally, the coupled grouped wave discussed in section 6.2.1 is no longer visible; it appears to be blended with the effects of the oscillating fluid. Furthermore, several cold fluid occurrences are identified in the analysed figure. These cold patterns

originate from the cold plumes previously observed in Figure 7.2(c).

Figure 7.4 displays the temperature over time on the Meridian at radius $r_{3/4}$ for the same parameters seen in Figure 7.2. For the first case in Figure 7.4(a), no spatial changes are visible in time. However, along the Meridian, the three hot areas are visible. They originate from the plumes discussed earlier, located at the Poles ($\theta = 0$ and $\theta = \pi$) and at the Equator ($\theta = \pi/2$).

In Figure 7.4(b), the vacillating and recurring structures associated with the travelling fishbone pattern are identified in the equatorial region around $\theta = \pi/2$. In the polar

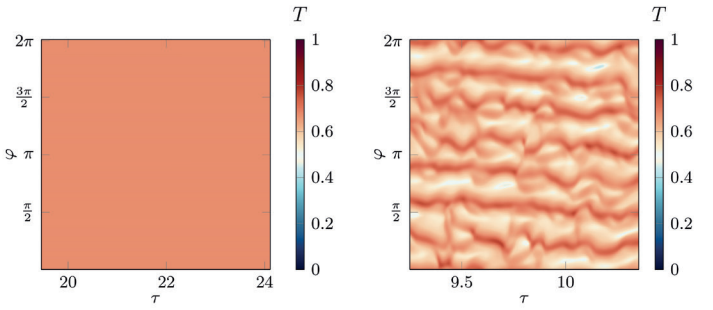

(a) $\mathrm{Ra_E} = 1.59 \cdot 10^4$, $\mathrm{Ro} = 0.429$, $\mathrm{Ta} = 110.3$ (b) $\mathrm{Ra_E} = 3.98 \cdot 10^4$, $\mathrm{Ro} = 0.708$, $\mathrm{Ta} = 600.6$

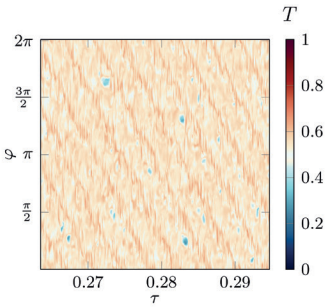

(c) $\mathrm{Ra_E} = 1.77 \cdot 10^6$, $\mathrm{Ro} = 1.14$, $\mathrm{Ta} = 6.37 \cdot 10^5$

Figure 7.3.: Space-time plots on the Equator at $r_{3/4}$ and $\theta = \pi/2$ for rising electric Rayleigh number $\mathrm{Ra_E}$ and rotation rate Ta and Ro.

regions, at angles $\theta \approx 0$ and $\theta \approx \pi$, fluctuations in the plume structure are noticeable, as previously referred to in Figure 7.2(b).

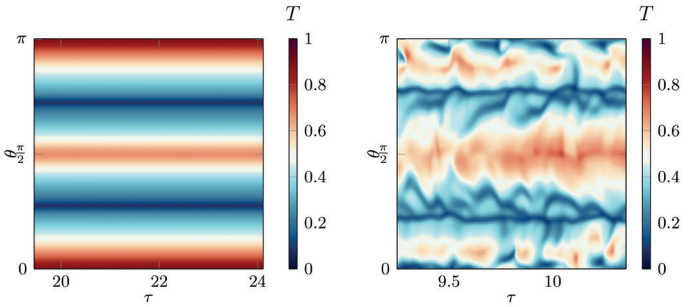

(a) $\mathrm{Ra_E} = 1.59 \cdot 10^4$, $\mathrm{Ro} = 0.429$, $\mathrm{Ta} = 110.3$ (b) $\mathrm{Ra_E} = 3.98 \cdot 10^4$, $\mathrm{Ro} = 0.708$, $\mathrm{Ta} = 600.6$

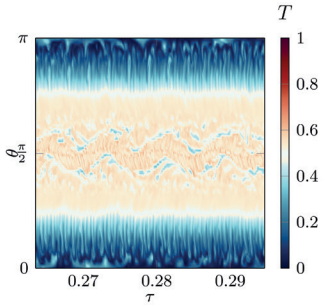

(c) $\mathrm{Ra_E} = 1.77 \cdot 10^6$, $\mathrm{Ro} = 1.14$, $\mathrm{Ta} = 6.37 \cdot 10^5$

Figure 7.4.: Space-time plots on the Meridian at $r_{3/4}$ and $\varphi = 0$ for rising electric Rayleigh number $\mathrm{Ra_E}$ and rotation rate Ta and Ro.

Final Figure 7.4(c) shows wave pattern observed in the equatorial region around $\theta = \pi/2$. This is similar to the wave pattern seen previously in Figure 6.4(c) without DEP force, but is now much scattered by vacillating structures here, making it hard to discern the wave seen before without the DEP forcing. Additionally, the previously identified colder circular occurrences now become evident, primarily located slightly above and below the Equator, as originating from a cold plume visible in Figure 7.2(c) on the Pole-to-Pole cut.

Focusing on the polar region in Figure 7.4(c), at $\theta \approx 0$ and $\theta \approx \pi$, hot fluid vacillations emerge over time, which were absent in the earlier Figure 6.4(c) without DEP force. These plumes manifest randomnly throughout the time-lapse and have been previously identified in the temperature plot in Figure 7.2(c) and the radial velocity graph in Figure 7.2(d).

To summarise the cases plotted in Figures 7.2, 7.3, and 7.4, the presence of the DEP force in sTC introduces additional fluctuations. TEHD convection exhibits a plume-dominated pattern, characterised by fluid movement both radially inward and outward over the shells. In contrast, sTC displays a meridional flow dominance. The combination of these two elements gives rise to what is referred to as the fishbone pattern in a particular combination. Additionally, the isosurfaces indicate that TEHD convection significantly contributes to flow oscillations, leading to an irregular flow pattern when subjected to high DEP force.

7.2.2 Convective heat transfer scaling

The previous section showed qualitative results using isosurfaces for TEHD convection with differential rotation. The following results present the Nusselt number and the volume and time-averaged kinetic energy $\tilde{E}_{\mathrm{kin}}$. Figures 7.5(a) and 7.5(b) illustrate these quantities concerning the electric Rayleigh number $\mathrm{Ra_E}$ and the differential rotation rate ϖ.

For the extreme values on the borders of the parameter space, the evolution of the Nusselt number is similar to that seen in Figures 5.6(a) and 6.7(a). Gaillard et al. [119] investigated the rise of the Nusselt number for combined rising DEP force and rotation rate for selected parameters. The forcing increases with the Nusselt number, specifically, at the highest rotation rate ϖ, $\mathrm{Nu} = 11.46$ in the presence of TEHD convection for the lowest electric Rayleigh number, while it is $\mathrm{Nu} = 11.45$ without the DEP force. Conversely, at the lowest rotation rate ϖ and the highest electric Rayleigh number $\mathrm{Ra_E}$, the Nusselt number is $\mathrm{Nu} = 11.70$, compared to $\mathrm{Nu} = 11.80$ in the case without rotation. Thus, it can be concluded that in extreme scenarios, each dominant force yields similar values for heat transfer, as shown in the simulation that investigates the forcing parameters individually.

The same analysis is performed with the kinetic energy, which is illustrated in Figure 7.5(b). As with the previous findings, the kinetic energy increases for the lowest rotation rate, ϖ, when the electric Rayleigh number $\mathrm{Ra_E}$ rises, similar to what is shown in Figure

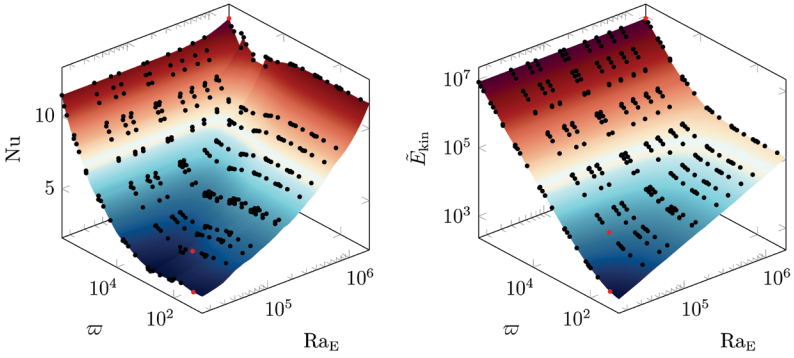

Figure 7.5.: Plots of (a) Nusselt number at the inner boundary, (b) volume, and time-averaged kinetic energy in the domain for rising electric Rayleigh number and rising differential rotation with isothermal boundary condition. The circular red marks (●) denote the cases seen in Figures 7.2.

5.6(b). Notably, the difference between the isolated and combined forces is even smaller for the kinetic energy compared to the variations observed in the Nusselt number.

At the highest rotation rate of ϖ without DEP force, the kinetic energy reaches $\tilde{E}_{\mathrm{kin}} = 8.27 \cdot 10^6$. When the smallest DEP force is applied, the kinetic energy increases slightly to $\tilde{E}_{\mathrm{kin}} = 8.28 \cdot 10^6$. Additionally, for the highest electric Rayleigh number at the lowest rotation rate, the kinetic energy is $\tilde{E}_{\mathrm{kin}} = 1.18 \cdot 10^5$, compared to $\tilde{E}_{\mathrm{kin}} = 1.16 \cdot 10^5$ without rotation.

In conclusion, it can be stated that at the selected high rotation rate, the kinetic energy changes only slightly when a small DEP force is introduced, and vice versa.

7.3 Discussion

The current section focuses on the transition from a rotation-dominated regime to a TEHD convection-dominated regime. The Nusselt number and kinetic energy serve as effective indicators for this transition. Both forces can exhibit a range of stable, transient, or even irregular states that impact these quantities. A regime diagram is proposed afterwards.

7.3.1 Transition between differential rotation and DEP force-dominated flow

After analysing minimum and maximum values from the parameter space in Figures 7.5(a) and 7.5(b), this section provides a detailed examination of the transition from a TEHD convection to a rotation-dominated regime and vice versa.

The following Figure 7.6 presents the Nusselt number, and volume and time-averaged kinetic energy as a function of the electric Rayleigh number for selected rotation rates, to better visualise the previous Figure 7.5. Figure 7.6(a) demonstrates that the case with the lowest rotation rate of $\varpi = 2.03 \cdot 10^1$ has a Nusselt number similar to that with uniquely TEHD convection. As discussed in section 6.3.3, for sTC flow at this rotation rate, heat is primarily transported through conduction. Consequently, convective heat transfer from TEHD convection becomes the dominant mechanism in this combined case for transporting heat.

For the rotation rate $\varpi = 6.09 \cdot 10^3$, the Nusselt number is initially higher than that for uniquely TEHD convection until the electric Rayleigh number reaches $\mathrm{Ra_E} = 7 \cdot 10^4$. Beyond this point, a slight and consistent separation in Nusselt number is observed, resulting in a slightly lower Nusselt number for the simulations combining the TEHD convection and sTC. A similar behaviour is seen at the rotation rate $\varpi = 1.17 \cdot 10^5$. Initially, the Nusselt number from differential rotation exceeds that of TEHD convection;

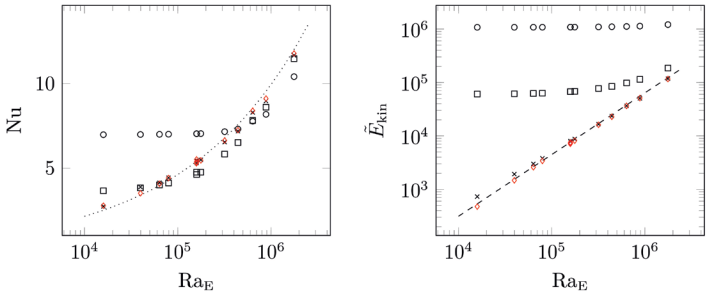

Figure 7.6.: Plots of (a) Nusselt number at the inner boundary with power law from eq. (5.8) (·····), (b) volume, and time-averaged kinetic energy in the domain with power law from eq. (5.10) (- - -) for rising electric Rayleigh number at selected rotation rates $\varpi = 0$(◇), $\varpi = 2.03 \cdot 10^1$ (×), $\varpi = 6.09 \cdot 10^3$(□) and $\varpi = 1.17 \cdot 10^5$ (○) for the simulations with isothermal temperature boundary conditions.

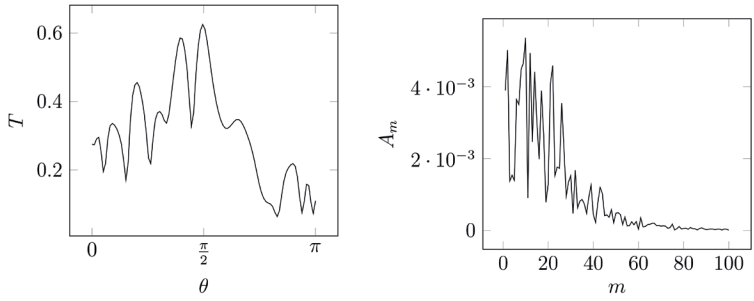

(a) (b)

Figure 7.7.: Plot of (a) the temperature along the Meridian at the mid-gap to process (b) the spatial modes from FFT for a timestep from where the STME is calculated.

however, beyond $\mathrm{Ra_E} = 4 \cdot 10^5$, the Nusselt number from differential rotation falls below that of TEHD convection without rotation.

The presence of differential rotation suppresses the Nusselt number-enhancing structures from TEHD convection. This phenomenon has been studied in a cylindrical annulus by Gaillard et al. [14], where it was demonstrated that flow structures distributed across a broad spectrum enhance the Nusselt number. High-vacillating structures spread the spectral energy over an extensive range of modes. Gaillard et al. showed that the Nusselt number increases as the STME decreases, provided that the vacillating structures dominate the domain and the flow remains strongly irregular. In this work, increasing the rotation resulted in higher STME levels, which decreased the Nusselt number.

This effect is apparent in the current work for the selected electric Rayleigh numbers $\mathrm{Ra_E} = 8.84 \cdot 10^5$ and $\mathrm{Ra_E} = 1.77 \cdot 10^6$. The STME is retrieved from temperature at the mid-gap along the Meridian as shown in Figure 7.7(a), where the interaction of radial dominated TEHD convection and meridional dominated sTC flow is best observable. The temperature along the Meridian is then processed via an FFT, where the spatial modes can be retrieved as shown in Figure 7.7(b) for a single time-step. For 300 available time steps, the results from the FFT are time-averaged. From it, the STME is then calculated using eq. (4.20).

The corresponding STME and Nusselt numbers for the different rotation rates are detailed in Table 7.1. As observed, the Nusselt number decreases when the STME in-

Table 7.1.: STME for selected electric Rayleigh number and rotation rates according to the resulting Nusselt number.

	$\mathrm{Ra_E} = 8.84 \cdot 10^5$		$\mathrm{Ra_E} = 1.77 \cdot 10^6$	
	E_m	Nu	E_m	Nu
$\varpi = 0$	$9.70 \cdot 10^{-2}$	9.12	$8.45 \cdot 10^{-2}$	$1.18 \cdot 10^1$
$\varpi = 8.13 \cdot 10^2$	$1.37 \cdot 10^{-1}$	8.99	$1.12 \cdot 10^{-1}$	$1.17 \cdot 10^1$
$\varpi = 6.09 \cdot 10^3$	$1.89 \cdot 10^{-1}$	8.61	$1.31 \cdot 10^{-1}$	$1.15 \cdot 10^1$
$\varpi = 4.35 \cdot 10^4$	$2.60 \cdot 10^{-1}$	7.90	$2.06 \cdot 10^{-1}$	$1.04 \cdot 10^1$

creases. Given that these cases predominantly exhibit irregular characteristics, it can be concluded that the presence of the sTC flow reduces the transport of heat through the gap by attenuating smaller scales in the flow.

Regarding the kinetic energy illustrated in Figure 7.6(b), the interaction between both forces is not visible. With each increment in rotation rate, a new level of kinetic energy is added, and the influence from TEHD convection becomes negligible. The kinetic energy for TEHD convection without rotation begins to catch up with that from $\varpi = 2.03 \cdot 10^1$, indicating that the kinetic energy contribution is primarily derived from TEHD for this specific case.

Figure 7.8 illustrates the Nusselt number and volumetric and time-averaged kinetic energy plotted for selected electric Rayleigh numbers as a function of the rising rotation rate. For the chosen electric Rayleigh numbers $\mathrm{Ra_E}$ above zero, the Nusselt number holds initially at a constant level, as depicted in Figure 7.8(a). Further increasing the rotation, the Nusselt number decreased. After this initial drop, the Nusselt number rises again with the rotation rate. This drop in Nusselt number is not visible for the case without DEP forcing; this one remains at a lower rotation rate, below the Nusselt number of the cases with DEP forcing, and catches up with increasing rotation.
The drop in the Nusselt number is well visible for $\mathrm{Ra_E} = 3.18 \cdot 10^5$ at a rotation rate of $\varpi = 6.09 \cdot 10^3$ and for $\mathrm{Ra_E} = 8.84 \cdot 10^5$ at $\varpi = 4.35 \cdot 10^4$. For the lowest chosen electric Rayleigh number, the minimum is less discernible but present at rotation rate $\varpi = 6.51 \cdot 10^2$.
Three regimes are proposed for this transition in the Nusselt number. Before the drop occurs, the Nusselt number remains constant, where the convection is mainly driven by the DEP force noted as regime (A). Regime (B) is the transitional regime where the Nusselt number begins to decrease until it reaches a minimum. The case where the

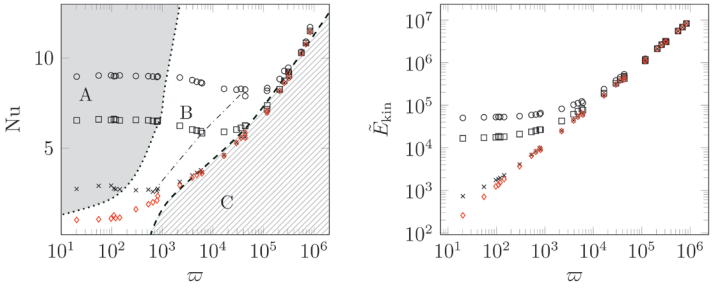

(a) (b)

Figure 7.8.: Plots of (a) Nusselt number at the inner boundary, (b) volume, and time-averaged kinetic energy in the domain for rising rotation rates at selected electric Rayleigh numbers $\mathrm{Ra_E} = 0(\diamond)$, $\mathrm{Ra_E} = 1.59 \cdot 10^4(\times)$, $\mathrm{Ra_E} = 3.18 \cdot 10^5(\square)$ and $\mathrm{Ra_E} = 8.84 \cdot 10^5(\circ)$ for the simulations with isothermal temperature boundary conditions. Line (·····) marks the beginning of the transition from DEP dominant regime (A) to regime (B) via decreasing Nusselt number, the transition line (-·-·-) connects the minimum Nusselt number and sTC dominant flow regime (C) is reached after line (- - -) via recovering values for Nusselt number.

minimum occurs for each electric Rayleigh number is connected by the dash-dotted line in Figure 7.8(a). When the Nusselt number recovers its original value, the regime (C) is reached, demonstrating a sTC dominant flow.

The Nusselt number is linked to convective heat and therefore to the kinetic energy, as illustrated in Figure 6.10. To clarify the mechanism behind the decrease in the Nusselt number, despite the constant increase in kinetic energy visible in Figure 7.8(b), three specific rotation rates are analysed for the electric Rayleigh number of $\mathrm{Ra_E} = 8.84 \cdot 10^5$ using the in-flow Nusselt number Nu^q (see eq. (4.18)).

Table 7.2.: Forcing parameter for an example transition from regime (A) to regime (B) and recovering in regime (C).

Regime	ϖ	$\mathrm{Ra_E}$	Nu	$\tilde{E}_{\mathrm{kin}}$
(A)	$8.13 \cdot 10^2$	$8.84 \cdot 10^5$	8.99	$6.54 \cdot 10^4$
(B)	$4.35 \cdot 10^4$	$8.84 \cdot 10^5$	7.90	$4.66 \cdot 10^5$
(C)	$1.17 \cdot 10^5$	$8.84 \cdot 10^5$	8.19	$1.13 \cdot 10^6$

The rotation rate $\varpi = 8.13 \cdot 10^2$ occurs before the drop in the Nusselt number. The rotation rate $\varpi = 4.35 \cdot 10^4$ corresponds to the minimum Nusselt number for this electric Rayleigh number. Finally, the rotation rate $\varpi = 1.17 \cdot 10^5$ marks the point where the Nusselt numbers begin to recover after the drop. The relevant Nusselt number and kinetic energy values are summarised in Table 7.2.

Remember the in-flow Nusselt number is equal to the Nusselt number at the walls, but can show local sources of heat transport in the bulk. As seen in section 6.3.3, the in-flow Nusselt number can be split into the conductive and convective parts to point out the dominant mechanism for transporting heat through the gap. The time-averaged convective $\langle r^2 u_r T \rangle_t$ and conductive $\langle -r^2 \partial_r T \rangle_t$ transport terms of the in-flow Nusselt number from cases seen in Table 7.2 are plotted in Figure 7.9 on a Pole-to-Pole isosurface cut. Figure 7.9(a) shows that the convective transport term is well distributed across the domain, which contributes to the high Nusselt number at the wall. However, further increases in the rotation rate, as indicated in Figure 7.9(b), lead to a concentration of the convective transport term at the Equator.

The significant difference in the conductive behaviour between Figure 7.9(a) and Figure 7.9(b) lies in the heat conduction distribution at the wall. The case presented in Figure 7.9(a) has a vast uniformly conductive heat transfer in the wall regions. In the case of the Nusselt number drop in Figure 7.9(b) in the wall region, heat conduction is heterogeneously distributed, indicating that the fluid cannot transfer additional heat from the wall and has become thermally equilibrated. With the only significant convective heat transfer at the mid-gap occurring at the Equator, hence the heat transfer capability diminishes, resulting in a lower Nusselt number.

The highest rotation rate, $\varpi = 1.17 \cdot 10^5$, shown in Figure 7.9(c), bears a resemblance to the rotation rate of $\varpi = 4.35 \cdot 10^4$ in Figure 7.9(b). However, the kinetic energy generated in this case is significantly greater, as detailed in Table 7.2. Consequently, the Nusselt number at $\varpi = 1.17 \cdot 10^5$ recovers from its previous drop, demonstrating an increase as the rotation rate rises.

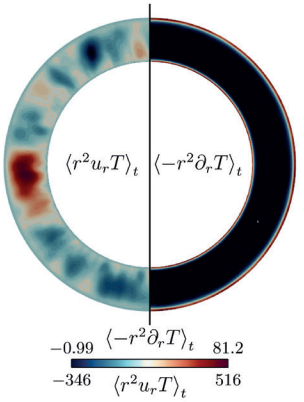

(a) $\varpi = 8.13 \cdot 10^2$, $\mathrm{Ra_E} = 8.84 \cdot 10^5$

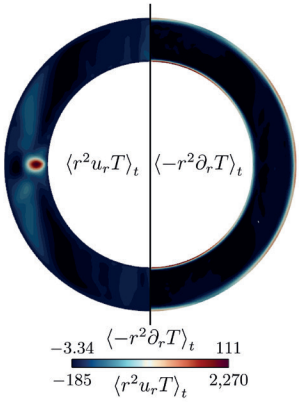

(b) $\varpi = 4.35 \cdot 10^4$, $\mathrm{Ra_E} = 8.84 \cdot 10^5$

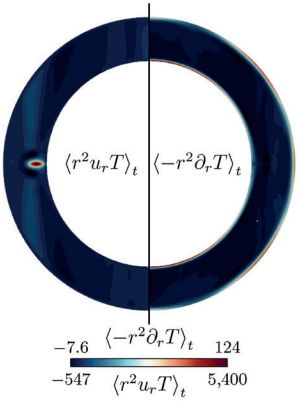

(c) $\varpi = 1.17 \cdot 10^5$, $\mathrm{Ra_E} = 8.84 \cdot 10^5$

Figure 7.9.: Isosurface of Pole-to-Pole cut of time-averaged convective $\langle r^2 u_r T \rangle_t$ and conductive $\langle -r^2 \partial_r T \rangle_t$ transport terms for selected electric Rayleigh numbers and rotation rates.

7.3.2 Regime classification

The following section presents the regime diagrams, which classify the simulations based on their patterns and link the previous regime changes to the Nusselt number. The regime diagrams examine the transition from steady-state to irregular simulations regarding the electric Rayleigh number and rotation rate. First, steady-state sTC will be discussed, followed by a second regime diagram that focuses on transient cases under the same conditions.

Regime diagram for steady-state sTC combining TEHD convection

The section begins by investigating the steady-state sTC seen in Figure 6.9(a), while incorporating the effects of TEHD convection, which then may result in transient flows. Plumes are observed in all these scenarios, where the rotation speed is not excessively high. This phenomenon is particularly evident in mid-latitude to polar regions, where the DEP force overcomes the meridional flow resulting from differential rotation, leading to the formation of plumes.

Furthermore, as illustrated in the previous section 6.2.2, specifically in Figure 6.5(e), for medium Rossby numbers, the angular velocity rapidly decreases in the outer region, resulting in conditions akin to those of a solid body. Consequently, this region, absent of meridional and azimuthal flow, does not inhibit plume formation caused by differential rotation. Since plumes are present in all these cases, they are not depicted in the subsequent regime diagram in Figure 7.10. The resulting patterns, such as fishbone and Stewartson-like structures, are illustrated in the mentioned regime.

The three colours, blue, green, and red, represent stationary, transient, and irregular flow patterns, respectively. Initially, all processed cases begin with a stationary solution at the lowest electric Rayleigh number. For the highest rotation in the diagram $\varpi = 4.35 \cdot 10^4$, Stewartson-like patterns emerge.

As the DEP force continues to increase, the simulation transitions to a transient and irregular state, leading to the disappearance of the Stewartson-like pattern and the formation of irregular plume structures. The specific electric Rayleigh number at which this transition occurs depends on the amount of differential rotation, ϖ. In particular, the transient region appears at a larger electric Rayleigh number as the rotation rate increases.

Section 7.3.1 discussed a regime change characterised by a drop in Nusselt number at a fixed electric Rayleigh number and an increasing rotation rate. The regime for the decreasing and recovering Nusselt number seen in Figure 7.8(a) is processed for the

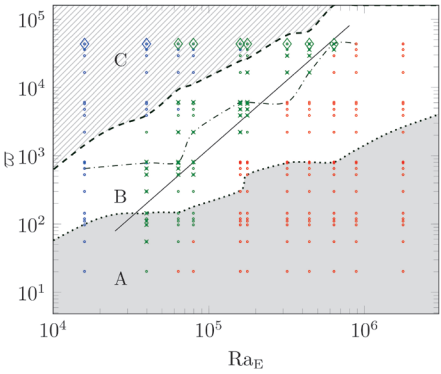

Figure 7.10.: Regime diagram for rotation rates and electric Rayleigh numbers for steady-state sTC flows classifying them as steady-state (•), transient (•) and irregular (•) flows, while marking fishbone (×) and Stewartson-like (◇) pattern. The solid linear regression line (——) is fit through the cases with fishbone patterns. Line (·····) marks the beginning of the transition from DEP dominant regime (A) to regime (B) via decreasing Nusselt number, the transition line (-·-·-) connects the minimum Nusselt number and sTC dominant flow regime (C) is reached after line (- - -) via recovering values for Nusselt number.

remaining electric Rayleigh numbers and added to Figure 7.10. The dash-dotted line connects the locations of the Nusselt number minimum in the transition regime (B) for each electric Rayleigh number in rising rotation. Regime (A) marks the area before the decrease in Nusselt number, and regime (C) denotes the area when the Nusselt number recovers its original value.

The fishbone patterns, as shown before in Figure 7.2(b), occur in uniquely in transient non-irregular flow. They are primarily located in regime (B) and are present when the minimum Nusselt number is reached. An exception is the Rayleigh number $\mathrm{Ra_E} = 3.18 \cdot 10^5$ which reaches the minum Nusselt number at $\varpi = 6.09 \cdot 10^3$. This may be due to the fact that the minimum is processed from discrete data, and the gap from $\varpi = 6.09 \cdot 10^3$ to the next rotation rate $\varpi = 3.59 \cdot 10^4$ does not cover continuous values for the minima.

In conclusion, the presence of the fishbone pattern links the regime change from mostly irregular plume-dominated flow to sTC-dominated flow.

To mark the transition relation between the TEHD convection and the sTC flow, a power law is fitted through the cases with a fishbone pattern marking the regime change defined as

$$\mathrm{Ra_E} = 2.8127 \cdot 10^3 \sqrt{\varpi} = 2.8127 \cdot 10^3 Ro\sqrt{\mathrm{Ta}}. \tag{7.6}$$

The rotation rate defined is directly proportional to the square of the system's rotation, expressed as $\varpi \sim \omega^2$. Therefore, the power law can be simplified to a linear fit as shown in eq. (7.6). The relation $\mathrm{Ro}\sqrt{\mathrm{Ta}}$ is the definition of the differential rotation rate in the system as defined in eq. (7.5). The regime change occurs at an electric Rayleigh number that is linearly related to the system's rotation, indicating that a certain equilibrium between the competing forces is being established. For future work, this should be further investigated to define the dependency on the Prandtl number and aspect ratio.

Regime diagram for transient sTC combining TEHD convection

The impact of the DEP force on transient sTC flows is analysed in this section. The results from the simulations, which analyse the electric Rayleigh number and rotation rates, are presented in Figure 7.11, where the different colours blue, green, and red designate stable, transient, and irregular flow patterns, respectively.

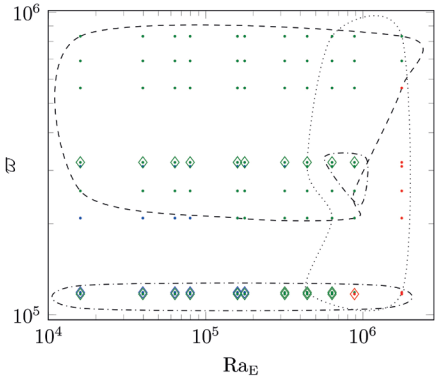

Figure 7.11.: Regime diagram for rotation rates and electric Rayleigh numbers for transient sTC flows classifying them as steady-state (●), transient (●) and irregular (●) flows, marking regions with Stewartson-like (◇) pattern, equatorial vortex(- - -), plumes(·····) and fishbones (-·-·-) pattern.

After the initial observation, some cases with a small rotation rate seem to stabilise again. However, an excessive increase in the electric Rayleigh number causes these cases to become transient and irregular states, where only the plume structure remains visible. Simultaneously, increasing the rotation rate creates the equatorial vortex, and the stable simulations become transient once again.

Fishbone patterns appear only occasionally compared to the regime diagram shown in Figure 7.10. This discrepancy is understandable, as there is no regime change from the steady-state sTC to transient by DEP force driven flow; these occur mainly for transient simulations for electric Rayleigh numbers below threshold, where the flow becomes plume-dominated and irregular.

The boundaries between specific regimes are not as distinct as in the previous regime diagram. Different patterns observed in this parameter range are grouped. The stable cases at the lower range of rotation exhibit Stewartson-like patterns. Plume structures only develop under strong DEP forcing when the electric Rayleigh number $\mathrm{Ra_E} > 5 \cdot 10^5$. Passing $\mathrm{Ra_E} > 1 \cdot 10^6$ leads to irregular flow. The equatorial vortex appears only during transient high-rotation flow. For $\varpi \in [2 \cdot 10^5, 3 \cdot 10^5]$ and $\mathrm{Ra_E} = 1.77 \cdot 10^6$, the DEP force suppresses the vortex resulting from sTC.

Figures 7.12 and 7.13 explain the origin of the stabilisation of the flow observed previously. For this purpose, the first differential transient case is chosen, located at $\mathrm{Ta} = 2.37 \cdot 10^5$ and $\mathrm{Ro} = 0.429$. Figure 7.12 displays the temperature on the corresponding equatorial slice on the left side. This case with $\mathrm{Ra_E} = 0$ clearly shows the development of alternating structures; the outward radial temperature is referred to as a "hill," while the inward-oriented fluid structure is referred to as a "valley." On the right side of Figure 7.12, the simulation with the same rotation rate is presented, but this time it adds the DEP force at an electric Rayleigh number of $\mathrm{Ra_E} = 1.59 \cdot 10^4$. The resulting flow does not show any alternating structures and remains rotational axis-symmetric.

Next, at the azimuthal locations of a "hill" and "valley" on the equatorial cut, a Pole-to-Pole cut temperature cut is done and plotted in Figure 7.13. The upper half of each subfigure shows the case without the influence of TEHD convection, and the lower half includes the forcing from DEP. Figure 7.13(a), illustrates the Pole-to-Pole cut at a "hill". Figure 7.13(b) shows the Pole-to-Pole cut at a "valley". Both figures indicate the magnitude and direction of the flow velocity using blue quivers and the magnitude and direction of the dynamic part of the DEP force $\mathbf{f}'_{\mathrm{DEP,dyn}}$ (see eq. (5.21)) using black quivers. Note, for the upper half of the Figures 7.13(a) and 7.13(b), the DEP force is processed but does not apply a forcing on the momentum eq. (7.2).

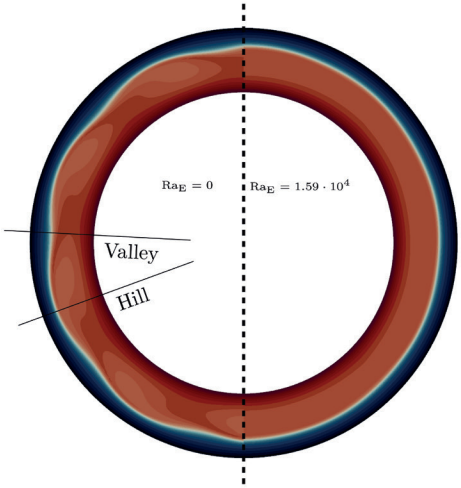

Figure 7.12.: Isosurface of the equatorial cut showing the temperature for rotation rate $\mathrm{Ta} = 2.37 \cdot 10^5$ and $\mathrm{Ro} = 0.429$ with and without DEP force for given electric Rayleigh number.

The orientation of the dynamic part of the DEP force does not change remarkably in the "hill" and "valley" sections plotted in Figures 7.13(a) and 7.13(b). The magnitude decreases along the gap width, as already seen in Figure 5.10. This means that in the case of active DEP, the fluid is pushed mainly radially outwards.

The velocity direction and magnitude do not differ significantly between those dependent on DEP forcing and those not. A slight difference is observable in Figure 7.13(a) for the "hill" in the dotted areas. When no DEP forcing is present, the velocity is more radially outward than the active DEP forcing on the lower half, where the quivers orient along the Meridian. This difference is also notable in Figure 7.13(b) for the "valley". However, without forcing from the DEP, the velocity orients slightly radially inwards in the dotted area compared to the lower half of the Figure, showing the quivers orienting along the Meridian. This change in radially outward and inward oriented velocity is responsible for generating "hills" and "valleys". Section 5.3.3 showed that the stronger electric field on the inner side of the gap is mainly responsible for the plume generation and the induced radial outward-oriented velocity in spherical geometries. The stronger forcing of the DEP on the inner side of the gap causes the velocity to orient less radially

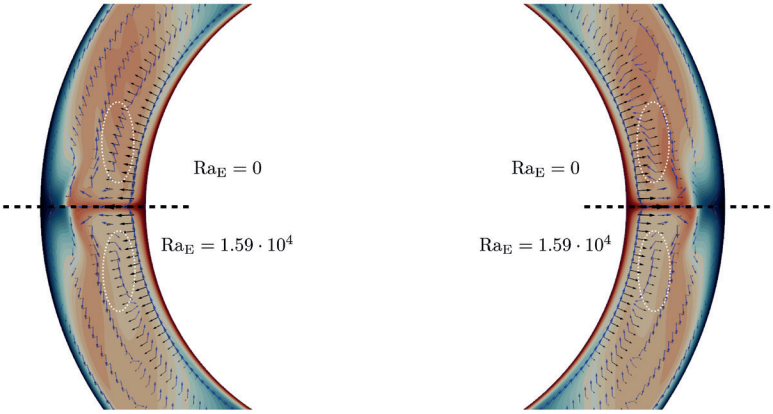

(a) (b)

Figure 7.13.: Isosurfaces of Pole-to-Pole cut showing the temperature for rotation rate $\mathrm{Ta} = 2.37 \cdot 10^5$ and $\mathrm{Ro} = 0.429$ with and without DEP force for (a) a hill and (b) a valley with quivers showing the velocity magnitude (⟶) and quivers of the dynamic part of the DEP force (⟶).

inward, leading to a "valley" otherwise. To maintain continuity, the velocity can no longer alternate between radially inward and outward-oriented flows, resulting in the axis-symmetric case when active DEP forcing is present.
Future work may show different behaviour implementing a force, which does not decrease radially with r^5 like the DEP force.

7.4 Summary

The current chapter combines TEHD convection with sTC flow. By visualising the resulting quantities on the isosurfaces, significant alterations in the behaviour of the individual flow are observed. The presence of the DEP force introduces additional vacillating structures within the steady-state sTC flows. Recurrent structures over time are scattered or become hardly discernible. A novel pattern, designated as the fishbone, has been identified.

The progression of the Nusselt number across the combined parameters is compared to the individual flows. The DEP force is the dominant force increasing the Nusselt number

for a low rotation rate. Vice versa, for a low DEP force, the Nusselt number and the kinetic energy rise are mainly driven by differential rotation. This change is significant for moderate and high combined values of electric Rayleigh numbers and rotation rates. Differential rotation attenuates small structures in regions where the flow from the DEP force is high-vacillating, resulting in a lower Nusselt number while maintaining a high level of kinetic energy.
A regime classification using the Nusselt number is proposed by transitioning from a TEHD convection-dominated flow to a regime dominated by sTC flow, achieved by continuously increasing the rotation. The in-flow Nusselt number shows the distribution of heat transfer in the gap. The TEHD convection transports heat along the whole Meridian while the flow from sTC concentrates heat transport in the equatorial region. After reaching the thermal equilibrium in the wall region, the flow from sTC cannot transport more heat for a similar level of kinetic energy.
A diagram shows that the regime transition correlates with the presence of the fish-bone pattern. A relation marking the regime change from irregular TEHD convection to steady-state sTC is proposed in eq. (7.6).

A second regime diagram combining the transient sTC flow with the DEP force shows its stabilising effect, resulting again in steady state cases. The recurring transient pattern in sTC flow shows alternating radially inward and outward-oriented flow. The strong DEP forcing on the inner side of the gap is responsible for repelling the inward-oriented flow. To maintain the continuity of the flow, the outward-oriented flow vanishes, resulting in the steady-state flow. This finding needs to be further analysed in the future. It would be interesting to see if this behaviour repeats when the force decreases less steeply, like with r or r^2 instead of r^5.

8 TEHD convection in spherical Taylor-Couette flow with experiment-like thermal boundary conditions

The final chapter of the results examines the combination of TEHD convection with differential rotation, where the thermal boundary condition is heterogeneous, mimicking AtmoFlow's thermal boundary conditions. The heterogeneous boundary condition induces instabilities resulting in different patterns, which is the core investigation of this chapter. The first section outlines the model formulation setup. The results present an analysis of the new emerging patterns, which are then classified in a separate section.

8.1 Model formulation

The evaluation of the demanded setup necessitates the same equations as in the previous chapter. The governing equations begin with the continuity and momentum equations defined as:

$$\boldsymbol{\nabla} \cdot \mathbf{u} = 0 \tag{8.1}$$

$$\begin{aligned} \partial_t \mathbf{u} + (\mathbf{u} \cdot \boldsymbol{\nabla})\mathbf{u} = &- \boldsymbol{\nabla} P + \mathrm{Pr}\, \boldsymbol{\nabla}^2 \mathbf{u} \\ &- \mathrm{Pr}\sqrt{\mathrm{Ta}}\, \mathbf{e}_z \times \mathbf{u} \\ &- \frac{1}{4}\mathrm{Pr}^2\, \mathrm{Ta}\, \mathbf{e}_z \times (\mathbf{e}_z \times \mathbf{x}) \\ &- \mathrm{Pr}\, \mathrm{Ra}_\mathrm{E} |\mathbf{E}|^2 \boldsymbol{\nabla} T. \end{aligned} \tag{8.2}$$

$$\partial_t T + (\mathbf{u} \cdot \boldsymbol{\nabla}) T = \boldsymbol{\nabla}^2 T \tag{8.3}$$

$$\boldsymbol{\nabla} \cdot [(1 - \gamma_e T)\,\mathbf{E}] = 0, \quad \text{with} \quad \mathbf{E} = -\boldsymbol{\nabla}\vartheta \tag{8.4}$$

Equation 8.2 includes the forcing from the DEP, Coriolis, and centrifugal forces from the rotating reference frame. To process heat transport in the field, the temperature eq. (8.3) needs to be solved. The Gauss eq. (8.4) solves the temperature-dependent electric field.

An electric potential is applied to the inner boundary. The temperature boundary conditions are now dependent on the meridional location and are defined by eq. (4.1) and eq. (4.2) for the inner and outer boundaries, respectively. The inner shells rotate relatively to the outer one, which remains at rest in the rotating reference frame, controlled by the Taylor number. The Dirichlet boundary conditions are summarised as

$$\begin{cases} \mathbf{u} = \mathrm{Pr}\,\mathrm{Ro}\,\sqrt{{}^{1}\!/_{4}\mathrm{Ta}}\; r\sin(\theta)\mathbf{e}_{\varphi}, & T = T_{\mathrm{in}}(\theta), \quad \vartheta = 1, \quad \boldsymbol{\nabla} p = 0, \quad \text{at} \quad r = \dfrac{\eta}{1-\eta} \\ \mathbf{u} = 0, & T = T_{\mathrm{out}}(\theta), \quad \vartheta = 0, \quad \boldsymbol{\nabla} p = 0, \quad \text{at} \quad r = \dfrac{1}{1-\eta} \end{cases} \tag{8.5}$$

and are schematically shown in Figure 8.1.

Note that the conductive heat flux Q_{cond} necessary for processing the Nusselt number can no longer be calculated analytically; it must now be processed numerically. For a given temperature relationship in a conductive base state, the dimensionless heat flux is processed numerically as $Q_{\mathrm{cond}} = 7.056$. The regime parameters for gap temperature, voltage, and rotation rate remain unchanged compared to the previous chapter. This results in a combination of 12 parameters for TEHD convection (see Table 4.1) and 30 parameters for sTC (see Table 4.3), leading to a total of 360 simulations.

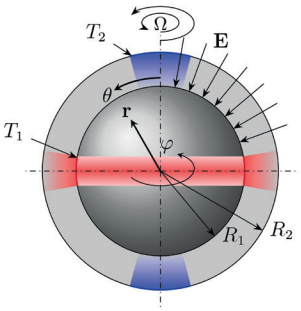

Figure 8.1.: Problem geometry and boundary conditions for TEHD convection in sTC using experiment-like boundary conditions.

8.2 Results

In the first part of this analysis, a qualitative comparison of contours for the chosen parameter is performed using isosurfaces. In the second part, a more detailed examination of the integral values for heat flux and kinetic energy is presented.

8.2.1 Spatial and temporal evolution of TEHD convection in sTC

The first parameter investigated in Figure 8.2 is set at a lowest rotation rate defined by a Taylor number of $\mathrm{Ta} = 110.3$ and a Rossby number of $\mathrm{Ro} = 0.429$ with the lowest DEP forcing from parameter space is chosen at electric Rayleigh $\mathrm{Ra_E} = 1.59 \cdot 10^4$, which is depicted in the first column of Figure 8.2. Figure 8.2(a) illustrates the temperature distribution across azimuthal, equatorial, and spherical slices. A noticeable band of hot fluid is present at the Equator, while cold plumes are observed at the Poles.

The radial velocity of the flow is represented in Figure 8.2(d), which shows a radially outwards-oriented flow at the Equator and a radially inwards-oriented flow at the Poles.

In the region between the Equator and the Poles, a predominantly meridional flow is established, as seen in Figure 8.2(g). It is important to note that, compared to the isothermal boundary case discussed in the previous chapter (refer to Figures 7.2(a), 7.2(d) and 7.2(g)), the cold plume at the Pole in this instance is oriented inward, and no plume is present in the area defined by $\theta = \pi/2 \pm \pi/4$.

The electric Rayleigh, Taylor and Rossby numbers increase, resulting in a new pattern emerging. The second column of Figure 8.2 depicts the cases where the electric Rayleigh number is set at $\mathrm{Ra_E} = 1.59 \cdot 10^5$, while the rotation rate aligns with the Taylor number $\mathrm{Ta} = 3.31 \cdot 10^4$ and a Rossby number of $\mathrm{Ro} = 0.429$. A distinct pattern becomes evident on the equatorial slice of temperature in Figure 8.2(b). The observed wave pattern appears only in the outer area of the gap width. Additionally, these visible patterns lead to slight fluctuations in radial speed within this region, as illustrated in Figure 8.2(e).

Instead of remaining perfectly aligned with the rotation axis, the plumes at the Poles shift around the axis. The off-centred plume is visible in both the temperature and radial velocity isosurfaces shown in Figures 8.2(b) and 8.2(e), respectively. Figure 8.2(h) displays the meridional velocity, demonstrating how the fluid bends the polar plume away from the rotation axis due to an enhanced velocity in the meridional direction.

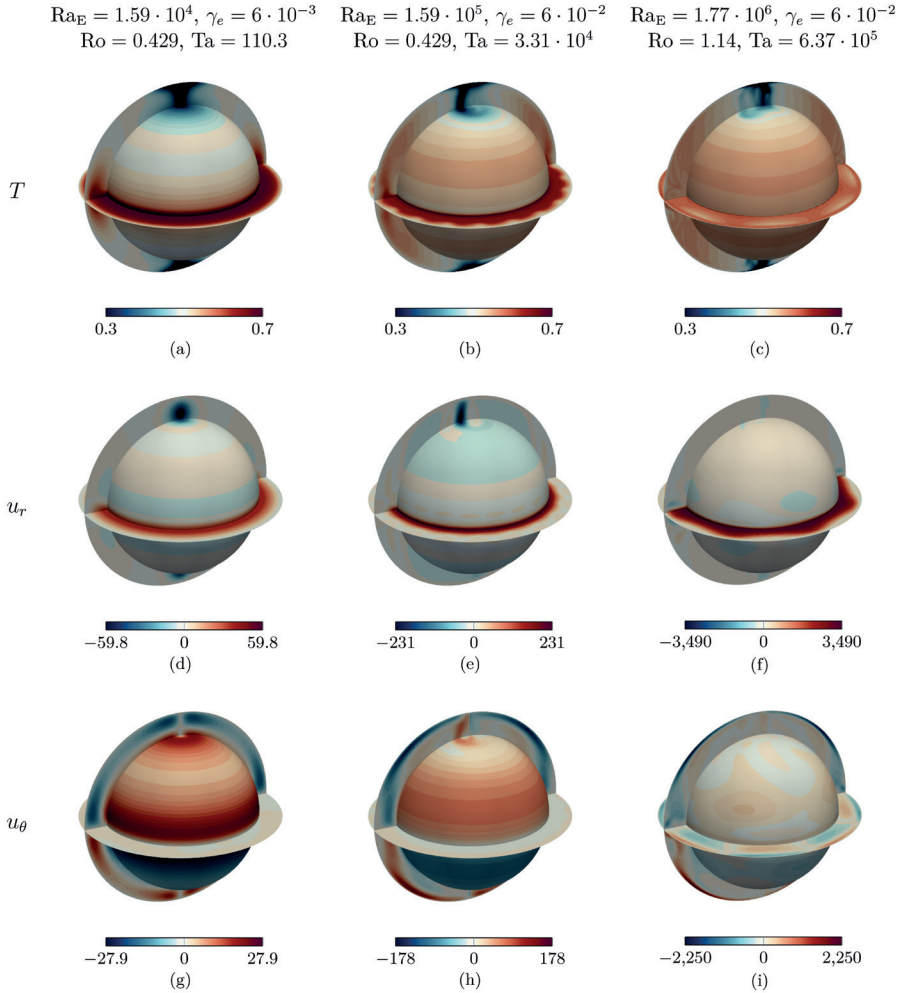

Figure 8.2.: Isosurface plots of temperature, T, radial velocity, u_r, and meridional velocity, u_θ, are shown in the top, middle, and bottom rows, respectively, across equatorial, meridional, and radial cross-sections on a spherical shell located at a quarter-radius $r_{1/4}$. Colour scales are provided below each panel. From left to right, the plots increase $\mathrm{Ra_E}$, Ta, and Ro incrementally.

The final case presented in the third column of Figure 8.2 sets the electric Rayleigh number is set at $\mathrm{Ra_E} = 1.77 \cdot 10^6$ and rotation rate at Taylor $\mathrm{Ta} = 6.37 \cdot 10^5$ and the Rossby number $\mathrm{Ro} = 1.14$.
This particular combination of parameters also results in a transient simulation. The equatorial plane of the temperature isosurface in Figure 8.2(c) displays a periodic wave pattern, while the polar cold plumes exhibit significant vacillations. The wave pattern is a significant pattern for the sTC has also been identified in Figure 6.2(c) from the previous chapter, which shares the same parameter setting for rotation.
The equatorial patterns are also apparent in the radial velocity isosurface shown in Figure 8.2(f), where an ongoing wavy pattern is visible around the rotation axis. This pattern is even more pronounced in the radial velocity compared to the isosurface without DEP forcing, as shown in Figure 6.2(f).
The meridional velocity displays a distinct alternating pattern congruous to the radial velocity on the equatorial cut shown in Figure 8.2(i). Notably, each pattern identifiable in the equatorial temperature isosurface depicted in Figure 8.2(c) alternates between upstream and downstream at that location. Additionally, a flow shear is evident for meridional velocity on the equatorial plane. When the flow closer to the inner side moves upward, the flow near the outer shell moves downward. This pattern is reversed in the adjacent neighbouring cell.

Space-time analysis

Figure 8.3 presents space-time plots of temperature at the Equator for a radius of $r_{3/4}$, based on the parameters shown in Figure 8.2. Figure 8.3(a) indicates no variation over time and space, confirming that this case is steady-state and axisymmetric.
In contrast, Figure 8.3(b) reveals alternating patterns with a mode number of 20 that are observable around the rotational axis. These patterns do not remain stationary over time; instead, they exhibit a slight drift.
Lastly, Figure 8.3(c) depicts a travelling mode, which aligns with observations made on the equatorial cut in Figure 8.2(c). It is important to note that the mode number has changed to 8, and this mode travels at a significantly faster rate due to the steeper angle over a shorter time interval.

The space-time plot of temperature along the Meridian at radius $r_{3/4}$ is shown in Figure 8.4. The parameters are the same as the isosurfaces given in Figure 8.2.
For the first parameter set in Figure 8.4(a), no change in time is visible either. Along the Meridian, the cold Plume on $\theta = 0$ and $\theta = \pi$ is visible. The hot region at $\theta = \pi/2$

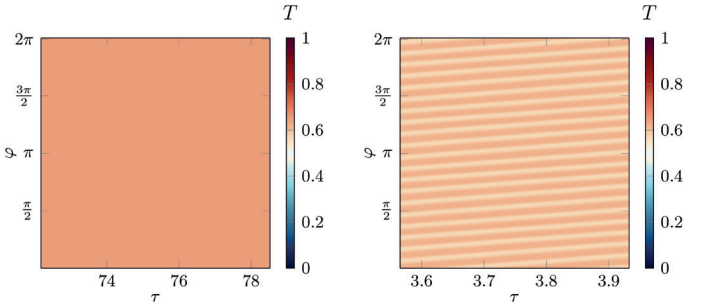

(a) $\mathrm{Ra_E} = 1.59 \cdot 10^4$, $\mathrm{Ro} = 0.429$, $\mathrm{Ta} = 110.3$ (b) $\mathrm{Ra_E} = 1.59 \cdot 10^5$, $\mathrm{Ro} = 0.429$, $\mathrm{Ta} = 3.31 \cdot 10^4$

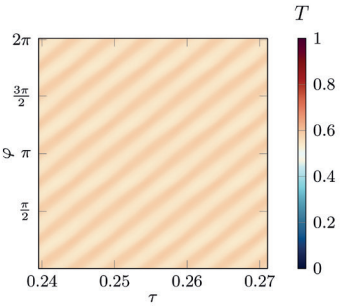

(c) $\mathrm{Ra_E} = 1.77 \cdot 10^6$, $\mathrm{Ro} = 1.14$, $\mathrm{Ta} = 6.37 \cdot 10^5$

Figure 8.3.: Space-time plots on the Equator at $r_{3/4}$ and $\theta = \pi/2$ for rising electric Rayleigh number $\mathrm{Ra_E}$ and rotation rate Ta and Ro using experiment-like thermal boundary conditions.

comes from the heated inner equatorial region. Besides the Poles and the Equator, the temperature remains around $T \approx 0.5$, which is close to the temperature of the Dirichlet boundary.

In Figure 8.4(b), a travelling mode can also be observed near the Equator $\theta = \pi/2$. In this region, the travelling mode aligns with the time-examined windows. The pattern continues from the Equator symmetrically towards the Poles until vanishing at $\theta \approx \pi/2 \pm \pi/6$, forming an angle.

In Figure 8.4(c), a recurrent oscillation is also visible in the equatorial region $\theta = \pi/2$. The inner rotating sphere entrains the travelling mode, displaying three identifiable periods

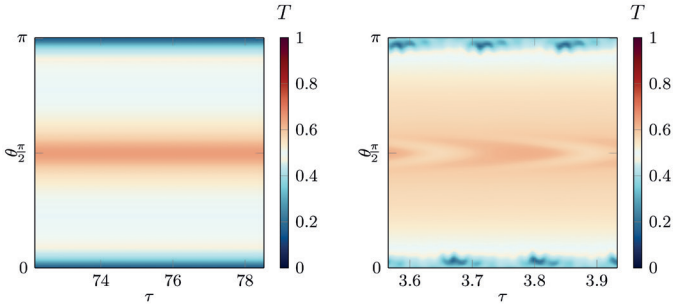

(a) $\mathrm{Ra_E} = 1.59 \cdot 10^4$, $\mathrm{Ro} = 0.429$, $\mathrm{Ta} = 110.3$ (b) $\mathrm{Ra_E} = 1.59 \cdot 10^5$, $\mathrm{Ro} = 0.429$, $\mathrm{Ta} = 3.31 \cdot 10^4$

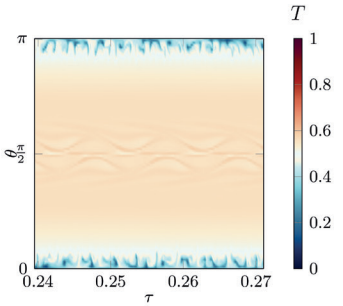

(c) $\mathrm{Ra_E} = 1.77 \cdot 10^6$, $\mathrm{Ro} = 1.14$, $\mathrm{Ta} = 6.37 \cdot 10^5$

Figure 8.4.: Space-time plots on the Meridian at $r_{3/4}$ and $\varphi = 0$ for rising electric Rayleigh number $\mathrm{Ra_E}$ and rotation rate Ta and Ro using experiment-like thermal boundary conditions.

during the time lapse. Additionally, at the Pole, the flow fluctuations are similar to those observed in Figure 8.4(b). However, these vacillations appear scattered and do not follow a periodic behaviour.

8.2.2 Convective heat transfer

After conducting a qualitative analysis of the isosurface, a more in-depth examination is performed using integral values such as the Nusselt number and the volumetric, time-averaged kinetic energy. This is illustrated in Figures 8.5(a) and 8.5(b), respectively.

As shown in Figure 8.5(a), the Nusselt number increases with the rising DEP force, which is represented by the electric Rayleigh number. Notably, the increase in Nusselt number corresponding to the electric Rayleigh number $\mathrm{Ra_E}$ is much more pronounced at low rotation rates ϖ compared to high rotation rates.

As the rotation rate increases, the Nusselt number rises, reaching significantly higher values for the highest rotation rate compared to the highest DEP forcing. Overall, the Nusselt number for cases using the experiment-like boundary conditions is considerably higher than in the isothermal cases plotted previously in 7.5(a).

The behaviour of kinetic energy mirrors this trend; a higher kinetic energy is observed with an increasing electric Rayleigh number. However, even at the highest electric Rayleigh number with rotation rate $\varpi > 10^3$, the kinetic energy seems to remain unaffected by the influence of the electrical field.

To clarify the observations from Figure 8.5, the Nusselt number and kinetic energy are plotted against the rising electric Rayleigh number $\mathrm{Ra_E}$ for selected rotation rates ϖ.

For the lowest rotation rate, $\varpi = 2.03 \cdot 10^1$, the Nusselt number shown in Figure 8.6(a) increases continuously with increasing electric Rayleigh number. As previously discussed

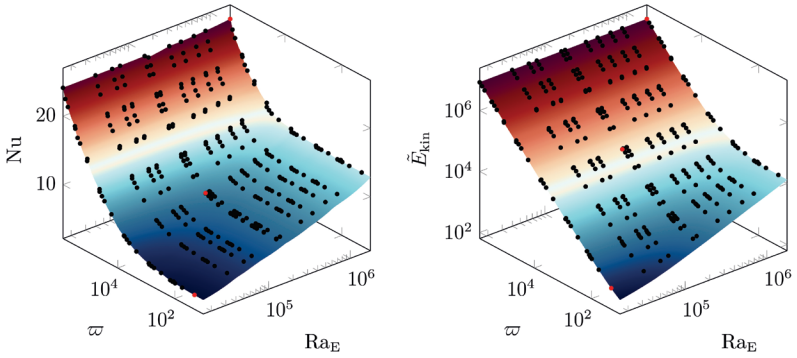

(a) Nusselt number

(b) Kinetic energy

Figure 8.5.: Plots of (a) Nusselt number at the inner boundary, (b) volume, and time-averaged kinetic energy in the domain for rising electric Rayleigh number and rising differential rotation with experiment-like boundary condition. The circular red marks (•) denote the cases seen in Figure 8.2.

in section 6.3.3, this rotation rate primarily transports heat via conduction. The dominant force for the convection here is the DEP force.
At the intermediate rotation rate of $\varpi = 6.09 \cdot 10^3$, the Nusselt number exhibits a higher offset compared to the lower rotation rate. Additionally, the rate of increase of the Nusselt number with respect to the electric Rayleigh number is slightly lower up to $\mathrm{Ra_E} = 1.8 \cdot 10^5$ in comparison to the lower rotation rate. Beyond this point, the Nusselt number for $\varpi = 6.09 \cdot 10^3$ increases parallel to the trend observed for $\varpi = 2.03 \cdot 10^1$, while still maintaining a slight offset.
The influence of the DEP force is even less pronounced at the highest selected rotation rate of $\varpi = 1.17 \cdot 10^5$. Until $\mathrm{Ra_E} \approx 3 \cdot 10^5$, the presence of the DEP force does not significantly affect the results; the Nusselt number remains relatively constant and only starts to increase slightly after the named threshold.
The same analysis is applied to the kinetic energy shown in Figure 8.6(b).
Starting with the lowest rotation rate, $\varpi = 2.03 \cdot 10^1$, an increase in electric Rayleigh number leads to a significant rise in kinetic energy, which is responsible for the notable convective heat observed earlier.
In contrast, for the next rotation rate, $\varpi = 6.09 \cdot 10^3$, the kinetic energy is already substantial from the outset. In this case, changes in the electric Rayleigh number do not significantly affect the energy levels, whether they increase or decrease. However, when comparing the values, a slight increase in kinetic energy can be observed between the electric Rayleigh numbers $\mathrm{Ra_E} = 8.84 \cdot 10^5$ and $\mathrm{Ra_E} = 1.77 \cdot 10^6$.
For the highest selected rotation rate, the kinetic energy remains at a consistently high level and is unaffected by changes in the electric Rayleigh number.

The comparison of the Nusselt number and kinetic energy is illustrated in Figures 8.7(a) and 8.7(b), respectively, for selected electric Rayleigh numbers across varying rotation rates. Starting at the lowest selected electric Rayleigh number, $\mathrm{Ra_E} = 1.59 \cdot 10^4$, the Nusselt number shows an increase with the rotation rate. This trend is similar to what was observed in the previously analysed case with isothermal boundary conditions (see Figure 7.8).
At a moderate electric Rayleigh number of $\mathrm{Ra_E} = 3.18 \cdot 10^5$, the Nusselt number begins with a significant offset compared to the previously selected electric Rayleigh number. As the rotation rate, ϖ, increases, the Nusselt number remains close to its initial value. It starts to increase around a rotation rate of $\varpi \approx 3 \cdot 10^3$, eventually catching up with the value at the lowest electric Rayleigh number at $\varpi \approx 3 \cdot 10^4$. Although a slight offset remains visible in the Nusselt number compared to the lower electric Rayleigh number, the values are relatively close.

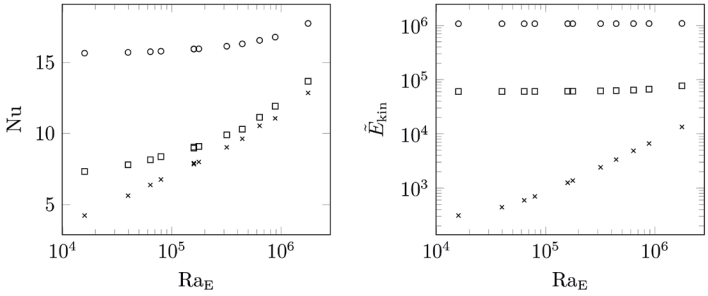

(a) Nusselt number

(b) Kinetic energy

Figure 8.6.: Plots of (a) Nusselt number at the inner boundary, (b) volume, and time-averaged kinetic energy in the domain for rising electric Rayleigh number at selected rotation rates $\varpi = 2.03{\cdot}10^1$ ($\times$), $\varpi = 6.09{\cdot}10^3$ ($\square$), $\varpi = 1.17{\cdot}10^5$ ($\circ$) for the simulations with experiment-like temperature boundary conditions.

The behaviour observed for the highest selected electric Rayleigh number, $\mathrm{Ra_E} = 8.84 \cdot 10^5$, shows a significant offset at low rotation rates. The Nusselt number begins to increase slightly at higher rotation rates, compared to the slope observed earlier, around a rotation rate of $\varpi \approx 2 \cdot 10^4$. The slope corresponding to the lowest electric Rayleigh number catches up at a rotation ratio of $\varpi = 3 \cdot 10^5$. However, a significant regime transition, as noted in the previous chapter, seen in Figure 7.8(a) is not evident in this case.

All observed slopes converge together where the distinction between the different electric Rayleigh numbers becomes difficult, meaning the influence of the DEP forcing becomes marginal. The power law found in section 6.2.3 from eq. (6.6) is added to Figure 8.7(a). The slopes adhere well to the power law at specific rotation rate, decreasing with smaller electric Rayleigh numbers. This supports the assumption that the DEP force makes only a marginal contribution to the Nusselt number for high-rotating flows. The power law was fitted for homogeneous thermal boundary conditions. It is remarkable that it still applies to this heterogeneous thermal boundary condition.

In Figure 8.7(b), the kinetic energy exhibits a behaviour similar to that of the Nusselt number. As the electric Rayleigh number increases, the kinetic energy rises at low rotation rates. With an increase in the rotation rate, the kinetic energy consistently increases. Additionally, the power law eq. (6.7) from section 6.2.3 is also plotted in this figure. The good agreement for rotation rates above $\varpi > 10^3$ again shows the marginal

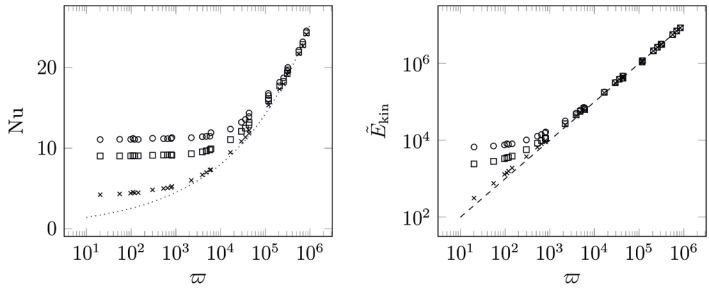

(a) (b)

Figure 8.7.: Plots of (a) Nusselt number at the inner boundary, (b) volume, and time-averaged kinetic energy in the domain for rising rotation rates at selected electric Rayleigh numbers $\mathrm{Ra_E} = 1.59 \cdot 10^4(\times)$, $\mathrm{Ra_E} = 3.18 \cdot 10^5(\square)$ and $\mathrm{Ra_E} = 8.84 \cdot 10^5(\circ)$ for the simulations with experiment-like temperature boundary conditions. Power laws from previous section are plotted $\mathrm{Nu} \sim \varpi^{1/4}$ (·····) $\tilde{E}_{\mathrm{kin}} \sim \varpi$ (- - -)

contribution from TEHD convection to the kinetic energy.

In concluding this description, for low electric Rayleigh numbers, the convection comes mainly from the differential rotation transporting cold fluid from the Pole along the inner sphere and, vice versa, hot fluid along the outer sphere. Furthermore, at a low rotation rate, the TEHD convection is primarily responsible for heat convection but is quickly overpowered by convection from differential rotation. A regime change, as seen previously in chapter 7 before, cannot be identified.

8.3 Discussion

This section discusses the characterisation of the regimes encountered. Unlike the isothermal boundary condition, the experiment-like boundary condition does not exhibit distinct regime changes in terms of Nusselt number and kinetic energy, nor does it allow for a clear identification of transient or irregular cases.

In the campaign utilising the experiment-like boundary condition, significant patterns, when they do appear, are primarily found in the equatorial or polar regions. The transient patterns observed in the polar region are mainly associated with instabilities from

the DEP force. This is primarily due to the lack of influence from differential rotation cases in the polar region, even at high rotation rates, as illustrated in section 6.2.1.
As shown in Figures 8.2(b) and 8.2(c), the changes in patterns are much more subtle. To improve comparability and quantify the observations, the equatorial slices are post-processed using EOF (see section 4.4.4). First, the emerging patterns are presented, followed by a classification of their intensity in a regime diagram.

8.3.1 Convective pattern classification with EOF

The first column of Figure 8.8 shows the equatorial temperature and the related EOFs at an electric Rayleigh number of $\mathrm{Ra_E} = 4.42 \cdot 10^5$ and a rotation rate of $\varpi = 300.6$. Figure 8.8(a) illustrates the temperature distribution at the Equator. The temperature changes are so subtle that they are not easily identifiable.
Figure 8.8(e) shows the first EOF of the temperature data across 300 time samples. This analysis reveals a mode 2 pattern with a high explained variance of $var_{\mathrm{exp}} = 95.7\%$. It is important to note that the highest amplitude is concentrated at the inner shell and decreases as the distance from the shell increases.
The subsequent EOF in Figure 8.8(i) exhibits a significantly lower explained variance of $var_{\mathrm{exp}} = 3.81\%$ and represents a single mode pattern. This pattern also appears near the inner shell, but its low variance makes it negligible for classification purposes.
The case presented in the second column of Figure 8.8 illustrates an example at a electric Rayleigh number of $\mathrm{Ra_E} = 8.84 \cdot 10^5$ with a rotation rate of $\varpi = 1.17 \cdot 10^5$. In this scenario, an instability can be observed in the equatorial temperature, as shown in Figure 8.8(b). Additionally, the mode formation is easily identifiable without the need for any additional post-processing, owing to its clear characteristics. The first EOF displayed in Figure 8.8(f) corresponds to a mode of 14, accounting for an explained variance of $var_{\mathrm{exp}} = 93.0\%$. It is important to note that the primary amplitude is concentrated in the mid-gap region. This observation is further supported by the second EOF in Figure 8.8(j), which shows a significantly lower variance compared to the first EOF.

Figure 8.8.: Isosurface plots of temperature T and its first EOF 0 and second EOF 1 and the associated explained variation for selected electric Rayleigh number and rotation rate showing the change of dominant inner pattern, to midgap pattern to outer pattern on the equatorial cut.

Finally, the remaining case in the third and fourth column has an electric Rayleigh number of $\mathrm{Ra_E} = 4.42 \cdot 10^5$ and a rotation rate of $\varpi = 4.35 \cdot 10^4$. The latter case features a higher rotation rate of $\varpi = 8.32 \cdot 10^5$ and an electric Rayleigh number at $\mathrm{Ra_E} = 6.36 \cdot 10^5$. Both cases exhibit a clear pattern in the temperature contours shown in Figures 8.8(c) and 8.8(d), where the maximum amplitude of the EOF is located on the outer side of the shell. A notable difference between the two cases is the mode number. The first EOF in Figure 8.8(g) is characterised by a high order mode number of 16, with an explained variance exceeding 95%. In contrast, the first EOF related to Figure 8.8(h) has a lower order mode number of 8 and a significantly lower explained variance of just above 50%. This indicates that the modes are distributed across higher orders in the second case.

In conclusion, EOFs can provide a more quantified representation of patterns and locations when oscillations are less visible. Depending on the parameter set, different patterns, inner, midgap, or outer, can be identified. This information allows for the classification of these structures.

8.3.2 Regime classification

A regime diagram is proposed in Figure 8.9, based on the pattern example shown via the EOF. The position of the most dominant pattern is determined using an FFT on the resulting EOF. The domain is divided into three regions: the inner region, defined by $r_{1/4}$; the mid-gap region, at $r_{1/2}$; and the outer region, at $r_{3/4}$. The FFT is applied to the first EOF for each radius, and the amplitude related to the mode is used to identify the dominant mode and its location.
Instability on the inner side of the shell is indicated by a diamond shape ($\diamond$). Patterns located in the mid-gap region are marked with a circle ($\circ$), while instabilities outside the shell are represented by a cross ($\times$). Base states, or mode 0, are designated with a dot. The size of the markers is scaled according to the explained variance of each case, multiplied by the amplitude of the dominant mode processed by the FFT. This approach helps to eliminate bias from stable patterns, which may show a high explained variance in the EOF analysis but a low amplitude in the FFT results.

Starting with the pattern inside the gap, the appearance begins at an electric Rayleigh number of $\mathrm{Ra_E} = 1 \cdot 10^5$, marked by the dotted line. As the electric Rayleigh number increases, the amplitude of the pattern diminishes. Previous results indicate that a higher electric Rayleigh number leads to a more unstable flow; consequently, the amplitude of the main periodic structure is overshadowed by other modes.

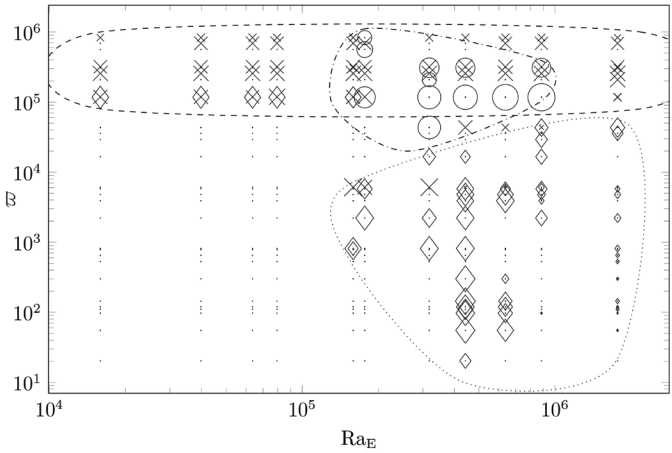

Figure 8.9.: Regime diagram for rotation rate ϖ and electric Rayleigh number $\mathrm{Ra_E}$ with experiment-like boundary conditions showing the pattern location on the inner side of the gap ($\diamond$) grouped by (·····), on the mid-gap ($\circ$) grouped by (-·-·-) and on the outer side of the gap ($\times$) grouped by (- - -)

Outer instability patterns primarily emerge at high rotation rates, starting at $\varpi = 10^5$. Here, the patterns initially display a noticeable amplitude. However, as the rotation rate continues to increase, the mark size decreases slightly, correlating with a reduction in the patterns amplitude. As indicated in section 6.2.1, further increasing the differential rotation may lead to irregular flow, resulting in a decreased amplitude of the periodic patterns in favour of smaller, oscillating structures. A dashed line groups the parameters for the outer pattern regime.

Finally, there is a transition from the inner instability patterns to the outer, mid-gap patterns. These are represented by the dash-dotted line in Figure 8.9 and emerge in conditions characterised by high electric Rayleigh and high rotation rates.

However, some locations of instability still do not align with the presumed origin of the pattern. At a rotation rate of $\varpi = 10^5$, where only outer instability patterns are expected, there is a range of even low electric Rayleigh numbers where the pattern appears within the shell gap. Additionally, in the case of grouped dotted patterns, where high electric Rayleigh number cases are anticipated and most patterns are found on the inside of the gap, there are spurious instances where the dominant pattern is situated close to the outer shell.

For investigating this inconsistency, Figure 8.10 illustrates the associated mode numbers for inner, mid-gap, and outer patterns.

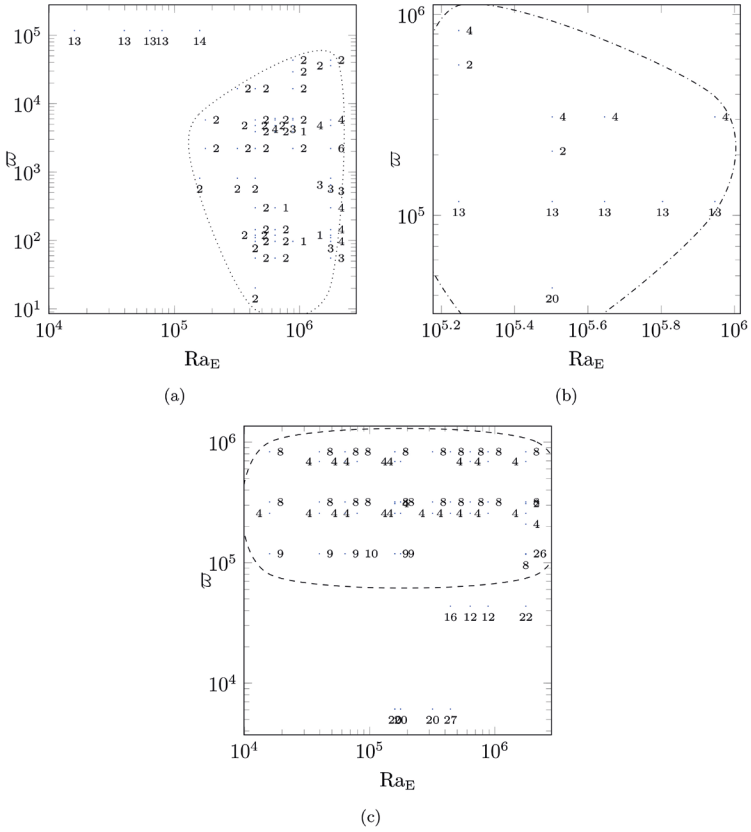

Figure 8.10.: Diagram showing for electric Rayleigh number and rotation rate the associated mode for dominant pattern at (a) the quarter gap $r_{1/4}$ (b) the mid-gap $r_{1/2}$ and (c) the three-quarter gap $r_{3/4}$. The grouped patterns seen in Figure 8.9 are plotted, grouping them at a quarter gap (·····), at the mid-gap (-·-·-), and at three-quarters of the gap (- - -).

Starting with the cases whose pattern from EOF lies on the inner side of the gap. Figure 8.10(a) shows that the enveloped cases inside the dotted line indicate that the mode number falls between one and four. It can be concluded that the TEHD dominant, $\mathrm{Ra_E} > 2 \cdot 10^5$ convection contributes to a lower mode number close to the inner shell.
The previously mentioned exceptional cases exhibit significantly higher mode numbers. Conversely, these instances are comparable to the mid-gap cases, which have an approximate mode number of around 13, as seen in Figure 8.10(b). Thus, those exceptional cases are comparable to the midgap case, an interplay of the DEP force and sTC flow, but reside a bit closer to the inner shell.

The pattern from EOF residing on the outer part of the gap, the cases circled by the dashed line have mode numbers of 4, 8, 9, and 10, as shown in Figure 8.10(c). The grouped cases are associated with instabilities arising from high rotation rates. The effect of the DEP force is marginal, since they are already unstable without any influences from the DEP force at this rotation rate, see the previous section 6.3.2.
The exceptional cases outside the grouping are of higher interest. These cases emerge only at considerable rotation speeds when $\mathrm{Ta} > 3.31 \cdot 10^4$, and all of those exceptional cases have a low Rossby number $\mathrm{Ro} = 0.429$. The prior Figure 6.6 shows that the outer angular velocity decreases rapidly on the equatorial line along the radius for this combination, resulting in a near solid-body rotation in the outer part of the gap.
The formation pattern in this outer region resembles TEHD convection in a solid body cylindrical annulus investigated by Gaillard et al. [14]. The solid-body part of the outer gap region represents a very narrow gap. The remaining temperature at this location can trigger those high-mode structures. Further investigation is necessary to confirm this effect at even lower Rossby numbers.

8.4 Summary

The investigation reveals the flow produced in sTC flow combined with TEHD convection using experimental-like temperature conditions. The first observation using isosurfaces reveals that the DEP force, resulting from the lower temperature gradient, scatters the flow significantly less. The flow results in the equatorial region as an axisymmetric steady-state case or exhibits a recurrent pattern. The polar areas still exhibit vacillations for high electric Rayleigh numbers due to the low effect of differential rotation in these areas.
The remaining visible patterns are therefore plumes at the Poles and a wave pattern along the Equator. The mode of the equatorial shifts significantly depends on the rota-

tion rate and forcing from the DEP force.

The resulting Nusselt number and kinetic energy are quickly dominated by the sTC flow. Using these boundary conditions, a regime change from TEHD convection-dominant flow to sTC flow cannot be identified.
A regime classification based on the pattern appearing becomes challenging, necessitating using EOFs. Using them, the recurring structures over time are identified on the equatorial cut and classified by their position in the gap and their mode number.
Flows with high electric Rayleigh numbers result in low-order modes in the inner layer of the gap. In contrast, differential rotation at high rotation rates significantly influences the modes in the outer layers of the gap. A transition from TEHD convection to a sTC pattern is observed, appearing in the mid-gap region.
Some exceptional high-mode patterns are found in the outer layer at high Taylor numbers and low Rossby numbers. This pattern may have originated from flow behaviours resembling near solid-body rotation, including TEHD convection effects. To gain a deeper understanding of this mechanism, further research with extended parameters or other numerical methods is of interest.

9 Conclusion and remarks for future work

The previous chapters examined the impact of TEHD convection in differential co-rotating spheres. This section summarises the results, discussion, and conclusions. The investigation utilised numerical methods implemented in the OpenFOAM CFD toolbox. A custom-coded solver within the OpenFOAM framework incorporates the temperature-dependent Gauss equation and accounts for the body force exerted by the electric field on the thermally heterogeneous fluid.

In the first result section of the thesis, both competing forces are analysed separately using isothermal boundary conditions for the sphere's boundary. The initial setup investigates TEHD convection in spheres, highlighting the plume-dominated flow that results from the DEP force. The study presents examples of steady-state, transient, and irregular flow. The results are compared to those of GeoFlow. Although the current research features a different aspect ratio than GeoFlow, the results show that the margins from steady-state, over transient to irregular flows are similar.

Additionally, the Nusselt number and volumetric and time-averaged kinetic energy are plotted as a function of the increasing electric Rayleigh number. The study via the power law examines the similarities of the Nusselt number between TEHD and natural convection. The kinetic energy does not increase linearly with the electric Rayleigh number. Compared to natural convection, TEHD convection induces more energy to the flow shown via a higher exponent in the power law eq. (5.10).

The impact of the thermal boundary condition, affecting the thermo-electric parameter, is examined. This section employs an analytical approach to demonstrate that for aspect ratio $\eta = 0.7$ an increase in thermal boundary conditions results in a stronger electric field. Consequently, this leads to greater forcing for the same Rayleigh number, resulting

in higher Nusselt numbers. However, the magnitude of this effect is found to be marginal in spherical geometries compared to the curvature affecting the electrical field.
The closing section shows the difference between TEHD in spherical geometries and natural convection. The stronger electric field close to the inner boundary drives the convection, resulting in outward-oriented hot plumes. The colder plumes result instead from the continuity conservation than the DEP force, becoming marginal in the outer section of the gap.

The second result chapter investigates the behaviour of non-isothermal sTC. It examines the non-linear behaviour of co-rotating differential rotating shells by comparing FVM to PAS results. As the rotation rate increases, the differences between the two solutions become more pronounced, highlighting the challenge of categorising flows in sTC. Notably, the angular velocity in the equatorial slice undergoes a significant change compared to cylindrical Stokes flow, leading to the non-linearity observed. The study also reveals patterns such as Stewartson-like patterns and equatorial vortices.
Furthermore, the margin to transient flow of sTC is analysed concerning the aspect ratio. Unlike previous studies with lower aspect ratios, the current work demonstrates an earlier transient behaviour in the flow.
Finally, the heat transport is compared to TEHD convection. The results show that, for the same amount of resulting kinetic energy, the TEHD convection can transport more heat through convection. Additionally, at low rotation rates, heat transport primarily occurs through conduction.

Then, the results combining TEHD convection in sTC flows are shown. Initially, an isothermal thermal boundary condition is maintained. Alongside patterns already observed in TEHD convection and sTC flows, a new pattern named "fishbone" emerges. This pattern marks the transition from steady-state sTC to transient and irregular TEHD flows. Additionally, a decrease in Nusselt number is noted in the transition region, which is linked to meridional flows from sTC that suppress more effective plume convection driven by the DEP force. To illustrate the transition area clearly, along with the fishbone patterns and heat transport minima observed, a regime diagram is proposed for the steady-state sTC combined with TEHD convection.
Next, the influence of TEHD on transient sTC is analysed. At high rotation rates, the primary patterns are predominantly from sTC, with the influence of the DEP force only becoming significant at higher electric Rayleigh numbers. Notably, TEHD exhibits a stabilising effect for slow-rotating sTC flows. A detailed analysis reveals that a stronger electric field on the inner side of the gap pushes the wavy equatorial vortex outward,

thereby inhibiting transient sTC.

The final chapter sets the AtmoFlow experiment-like temperature boundary conditions. In these simulations, the effect of the DEP force is considerably lower, leading primarily to steady-state and periodic transient cases. The resulting Nusselt number and kinetic energy do not indicate any transition between regimes. Therefore, EOFs are employed to identify and quantify the resulting transient cases.
Three groups of pattern locations have been identified. The inner part of the gap, which corresponds to a low-order mode pattern, is more closely associated with TEHD convection. Conversely, the pattern shifts to the outer section of the gap in rotation-dominated regimes. Additionally, midgap patterns are found between these two extremes.
However, some exceptional cases exhibit remarkably high-order patterns in the outer region of the gap, despite experiencing significant DEP forcing. These cases are characterised by a high rotation rate and a low Rossby number, leading to a near solid-body rotation in the outer region. In this context, the flow resembles a cylindrical TEHD solid-body annulus.

Outlook

For future research, more attention must be paid to the broader impact of the thermal boundary condition on the electric field and, consequently, on the resulting heat. Additionally, spherical geometries should be verified by comparing them with other aspect ratios, as this work only employed an analytical approach. Further numerical investigation is necessary because analytical solutions may not capture potential non-linear results.
Moreover, the stability margin for different aspect ratios in sTC systems requires further exploration. The current study provided insight into the early transient solution compared to Wicht's findings. It is essential to define the exact boundaries of the transient solution for co-rotating sTC systems dependent on the different aspect ratios.
Finally, expanding the parameter range may uncover additional regimes for combined forcing. Exploring further parameters could help clarify regime boundaries and better identify the transition to stable TEHD convection, particularly for transient sTC with TEHD.
The simulations that examined experiment-like thermal boundaries for low Rossby numbers and high Taylor numbers resulted in solid-body-like patterns in the outer gap region. As the current campaign produced only spurious cases, investigating even higher Taylor and lower Rossby numbers could provide improved insights into the appearance and

mode number associated with this flow type. Also, more other numerical methods, like Pseudo-Spectral methods, may give better insights into the overall mode distribution in these particular cases.

References

[1] F. Zaussinger, P. Canfield, A. Froitzheim, V. Travnikov, P. Haun, M. Meier, A. Meyer, P. Heintzmann, T. Driebe, and Ch. Egbers, "AtmoFlow - Investigation of Atmospheric-Like Fluid Flows Under Microgravity Conditions," *Microgravity Science and Technology*, vol. 31, pp. 569–587, Oct. 2019.

[2] C. Tropea, A. L. Yarin, and J. F. Foss, eds., *Springer Handbook of Experimental Fluid Mechanics*. Berlin, Heidelberg: Springer, 2007.

[3] G. I. Taylor, "VIII. Stability of a viscous liquid contained between two rotating cylinders," *Philosophical Transactions of the Royal Society of London. Series A, Containing Papers of a Mathematical or Physical Character*, vol. 223, pp. 289–343, Jan. 1923.

[4] A. Castellanos, ed., *Electrohydrodynamics*. Vienna: Springer Vienna, 1998.

[5] L.D. Landau and E.M. Lifshitz, *Electrodynamics of Continuous Media*. Internet Archive, 1960.

[6] H. N. Yoshikawa, M. Tadie Fogaing, O. Crumeyrolle, and I. Mutabazi, "Dielectrophoretic Rayleigh-Bénard convection under microgravity conditions," *Physical Review E*, vol. 87, p. 043003, Apr. 2013.

[7] R. J. Turnbull, "Electroconvective Instability with a Stabilizing Temperature Gradient. II. Experimental Results," *The Physics of Fluids*, vol. 11, pp. 2597–2603, Dec. 1968.

[8] A. Meyer, H. N. Yoshikawa, P. S. B. Szabo, M. Meier, C. Egbers, and I. Mutabazi, "Thermoelectric instabilities in a circular Couette flow," *Philosophical Transactions of the Royal Society A: Mathematical, Physical and Engineering Sciences*, vol. 381, p. 20220139, Jan. 2023.

[9] H. N. Yoshikawa, C. Kang, I. Mutabazi, F. Zaussinger, P. Haun, and C. Egbers, "Thermoelectrohydrodynamic convection in parallel plate capacitors under dielectric heating conditions," *Physical Review Fluids*, vol. 5, p. 113503, Nov. 2020.

[10] P. H. Roberts, "Electrohydrodynamic convection," *The Quarterly Journal of Mechanics and Applied Mathematics*, vol. 22, no. 2, pp. 211–220, 1969.

[11] C. Kang and I. Mutabazi, "Dielectrophoretic buoyancy and heat transfer in a dielectric liquid contained in a cylindrical annular cavity," *Journal of Applied Physics*, vol. 125, p. 184902, May 2019.

[12] V. Travnikov and C. Egbers, "Numerical investigation of atmospherelike flows in a spherical geometry," *Physical Review E*, vol. 104, p. 065110, Dec. 2021.

[13] P. S. Szabo, Y. Gaillard, F. Zaussinger, and C. Egbers, "Thermo-electrohydrodynamic convection in a differentially heated shell with electric central force field," *PAMM*, vol. 23, no. 1, p. e202200121, 2023.

[14] Y. Gaillard, P. S. B. Szabo, V. Travnikov, and C. Egbers, "Thermo-electrohydrodynamic convection in a rotating shell with central force field," *International Journal of Heat and Mass Transfer*, vol. 218, p. 124760, Jan. 2024.

[15] L. D Landau, E. M Lifshits, and L. P. Pitaevskiĭ, *Electrodynamics of Continuous Media*. Oxford: Pergamon Press Ltd, 1984.

[16] R. J. Turnbull, "Effect of Dielectrophoretic Forces on the Bénard Instability," *The Physics of Fluids*, vol. 12, pp. 1809–1815, Sept. 1969.

[17] P. J. Stiles, "Electro-thermal convection in dielectric liquids," *Chemical Physics Letters*, vol. 179, pp. 311–315, Apr. 1991.

[18] V. Babu, *Fundamentals of Incompressible Fluid Flow*. Cham: Springer International Publishing, 2022.

[19] L. D. Landau, *Fluid Mechanics: Landau and Lifshitz: Course of Theoretical Physics, Volume 6*. Pergamon, Nov. 2013.

[20] J. Wicht, "Flow instabilities in the wide-gap spherical Couette system," *Journal of Fluid Mechanics*, vol. 738, pp. 184–221, Jan. 2014.

[21] Joel H. Ferziger, Milovan Perić, and Robert L. Street, *Numerische Strömungsmechanik*. Springer, 2020.

[22] H. Bénard, "Les tourbillons cellulaires dans une nappe liquide. - Méthodes optiques d'observation et d'enregistrement," *Journal de Physique Théorique et Appliquée*, vol. 10, no. 1, pp. 254–266, 1901.

[23] S. C. Hung and E. J. Davis, "The onset of natural convection and its enhancement of heat transfer in stratified gas-liquid flow," *International Journal of Heat and Mass Transfer*, vol. 17, pp. 1357–1364, Nov. 1974.

[24] L. Rayleigh, "On convection currents in a horizontal layer of fluid, when the higher temperature is on the under side," *The London, Edinburgh, and Dublin Philosophical Magazine and Journal of Science*, vol. 32, pp. 529–546, Dec. 1916.

[25] F. H. Busse and J. A. Whitehead, "Instabilities of convection rolls in a high Prandtl number fluid," *Journal of Fluid Mechanics*, vol. 47, pp. 305–320, May 1971.

[26] F. H. Busse and R. M. Clever, "Instabilities of convection rolls in a fluid of moderate Prandtl number," *Journal of Fluid Mechanics*, vol. 91, pp. 319–335, Mar. 1979.

[27] F. H. Busse, "Non-linear properties of thermal convection," *Reports on Progress in Physics*, vol. 41, p. 1929, Dec. 1978.

[28] E. H. Bishop, L. R. Mack, and J. A. Scanlan, "Heat transfer by natural convection between concentric spheres," *International Journal of Heat and Mass Transfer*, vol. 9, pp. 649–662, July 1966.

[29] J. A. Scanlan, E. H. Bishop, and R. E. Powe, "Natural convection heat transfer between concentric spheres," *International Journal of Heat and Mass Transfer*, vol. 13, pp. 1857–1872, Dec. 1970.

[30] T. Nakagawa, Zierep, J., Bühler, K., Wimmer, M., and Kirchartz, K. R., "Thermal convection between two concentric spheres," *Proceedings of the 2nd JSME-KSME*, 1992.

[31] V. Travnikov, K. Eckert, and S. Odenbach, "Linear stability analysis of the convective flow in a spherical gap with H=0.714," *International Journal of Heat and Mass Transfer*, vol. 80, pp. 266–273, Jan. 2015.

[32] S. Chandrasekhar, "CXXXII. The thermal instability of a fluid sphere heated within," *The London, Edinburgh, and Dublin Philosophical Magazine and Journal of Science*, vol. 43, pp. 1317–1329, Dec. 1952.

[33] S. Chandrasekhar, "XXV. The onset of convection by thermal instability in spherical shells," *The London, Edinburgh, and Dublin Philosophical Magazine and Journal of Science*, vol. 44, pp. 233–241, Mar. 1953.

[34] F. H. Busse, "Patterns of convection in spherical shells," *Journal of Fluid Mechanics*, vol. 72, pp. 67–85, Nov. 1975.

[35] F. H. Busse and N. Riahi, "Patterns of convection in spherical shells. Part 2," *Journal of Fluid Mechanics*, vol. 123, pp. 283–301, Oct. 1982.

[36] H. Senftleben, "Über den Einfluß von magnetischen und elektrischen Feldern auf den Wärmestrom in Gasen," *Zeitschrift für Physik*, vol. 74, pp. 757–769, Nov. 1932.

[37] H. Senftleben and W. Braun, "Der Einfluß elektrischer Felder auf den Wärmestrom in Gasen," *Zeitschrift für Physik*, vol. 102, pp. 480–506, July 1936.

[38] B. L. Smorodin, "The effect of an alternating electric field on the liquid dielectric convection in a horizontal capacitor," *Technical Physics Letters*, vol. 27, pp. 1062–1064, Dec. 2001.

[39] B. L. Smorodin and M. G. Velarde, "On the parametric excitation of electrothermal instability in a dielectric liquid layer using an alternating electric field," *Journal of Electrostatics*, vol. 50, pp. 205–226, Feb. 2001.

[40] E. Barry, C. Kang, H. Yoshikawa, and I. Mutabazi, "Transfert de chaleur par convection thermoélectrique dans des cavités rectangulaires horizontales," *Entropie: thermodynamique énergie environnement économie*, vol. 2, Jan. 2021.

[41] H. N. Yoshikawa, O. Crumeyrolle, and I. Mutabazi, "Dielectrophoretic force-driven thermal convection in annular geometry," *Physics of Fluids*, vol. 25, p. 024106, Feb. 2013.

[42] V. Travnikov, O. Crumeyrolle, and I. Mutabazi, "Influence of the thermo-electric coupling on the heat transfer in cylindrical annulus with a dielectric fluid under microgravity," *Acta Astronautica*, vol. 129, pp. 88–94, Dec. 2016.

[43] C. Kang, A. Meyer, H. N. Yoshikawa, and I. Mutabazi, "Numerical simulation of circular Couette flow under a radial thermo-electric body force," *Physics of Fluids*, vol. 29, p. 114105, Nov. 2017.

[44] C. Kang, A. Meyer, H. N. Yoshikawa, and I. Mutabazi, "Thermoelectric convection in a dielectric liquid inside a cylindrical annulus with a solid-body rotation," *Physical Review Fluids*, vol. 4, p. 093502, Sept. 2019.

[45] A. Meyer, O. Crumeyrolle, I. Mutabazi, M. Meier, M. Jongmanns, M.-C. Renoult, T. Seelig, and C. Egbers, "Flow Patterns and Heat Transfer in a Cylindrical Annulus under 1g and low-g Conditions: Theory and Simulation," *Microgravity Science and Technology*, vol. 30, pp. 653–662, Oct. 2018.

[46] A. Meyer, M. Meier, M. Jongmanns, T. Seelig, C. Egbers, and I. Mutabazi, "Effect of the Initial Conditions on the Growth of Thermoelectric Instabilities During Parabolic Flights," *Microgravity Science and Technology*, vol. 31, pp. 715–721, Oct. 2019.

[47] P. S. B. Szabo, M. Meier, A. Meyer, E. Barry, V. Motuz, I. Mutabazi, and C. Egbers, "PIV and shadowgraph measurements of thermo-electrohydrodynamic convection in a horizontal aligned differentially heated annulus at different gravity conditions," *Experimental Thermal and Fluid Science*, vol. 129, p. 110470, Nov. 2021.

[48] P. S. B. Szabo, A. Meyer, M. Meier, V. Motuz, Y. Sliavin, and C. Egbers, "Simultaneous PIV and shadowgraph measurements of thermo-electrohydrodynamic convection in a differentially heated annulus," *tm - Technisches Messen*, vol. 89, pp. 148–157, Mar. 2022.

[49] C. Kang and I. Mutabazi, "Columnar vortices induced by dielectrophoretic force in a stationary cylindrical annulus filled with a dielectric liquid," *Journal of Fluid Mechanics*, vol. 908, Feb. 2021.

[50] I. Mutabazi, H. N. Yoshikawa, M. T. Fogaing, V. Travnikov, O. Crumeyrolle, B. Futterer, and C. Egbers, "Thermo-electro-hydrodynamic convection under microgravity: A review," *Fluid Dynamics Research*, vol. 48, p. 061413, Nov. 2016.

[51] J. E. Hart, J. Toomre, A. E. Deane, N. E. Hurlburt, G. A. Glatzmaier, G. H. Fichtl, F. Leslie, W. W. Fowlis, and P. A. Gilman, "Laboratory experiments on planetary and stellar convection performed on spacelab 3," *Science (New York, N.Y.)*, vol. 234, pp. 61–64, Oct. 1986.

[52] J. E. Hart, G. A. Glatzmaier, and J. Toomre, "Space-laboratory and numerical simulations of thermal convection in a rotating hemispherical shell with radial gravity," *Journal of Fluid Mechanics*, vol. 173, pp. 519–544, Dec. 1986.

[53] C. Egbers, W. Beyer, A. Bonhage, R. Hollerbach, and P. Beltrame, "The geoflow-experiment on ISS (part I): Experimental preparation and design of laboratory testing hardware," *Advances in Space Research*, vol. 32, pp. 171–180, July 2003.

[54] V. Travnikov, C. Egbers, and R. Hollerbach, "The geoflow-experiment on ISS (Part II): Numerical simulation," *Advances in Space Research*, vol. 32, pp. 181–189, July 2003.

[55] P. Beltrame, C. Egbers, and R. Hollerbach, "The GEOFLOW-experiment on ISS (Part III): Bifurcation analysis," *Advances in Space Research*, vol. 32, pp. 191–197, July 2003.

[56] B. Futterer, R. Hollerbach, and C. Egbers, "GeoFlow: 3D numerical simulation of supercritical thermal convective states," *Journal of Physics: Conference Series*, vol. 137, p. 012026, Nov. 2008.

[57] B. Futterer, C. Egbers, N. Dahley, S. Koch, and L. Jehring, "First identification of sub- and supercritical convection patterns from 'GeoFlow', the geophysical flow simulation experiment integrated in Fluid Science Laboratory," *Acta Astronautica*, vol. 66, pp. 193–200, Jan. 2010.

[58] B. Futterer, N. Dahley, S. Koch, N. Scurtu, and C. Egbers, "From isoviscous convective experiment 'GeoFlow I' to temperature-dependent viscosity in 'GeoFlow II'—Fluid physics experiments on-board ISS for the capture of convection phenomena in Earth's outer core and mantle," *Acta Astronautica*, vol. 71, pp. 11–19, Feb. 2012.

[59] B. Futterer, A. Krebs, A.-C. Plesa, F. Zaussinger, R. Hollerbach, D. Breuer, and C. Egbers, "Sheet-like and plume-like thermal flow in a spherical convection experiment performed under microgravity," *Journal of Fluid Mechanics*, vol. 735, pp. 647–683, Nov. 2013.

[60] S. Chandrasekhar, "The thermal instability of a rotating fluid sphere heated within," *The Philosophical Magazine: A Journal of Theoretical Experimental and Applied Physics*, vol. 2, pp. 845–858, July 1957.

[61] S. F. Chandrasekhar, "The thermal instability of a rotating fluid sphere heated within: II," *The Philosophical Magazine: A Journal of Theoretical Experimental and Applied Physics*, vol. 2, pp. 1282–1284, Oct. 1957.

[62] P. H. Roberts, "On the Thermal Instability of a Highly Rotating Fluid Sphere.," *The Astrophysical Journal*, vol. 141, p. 240, Jan. 1965.

[63] S. Chandrasekhar, *Hydrodynamic and Hydromagnetic Stability.* International Series of Monographs on Physics, Oxford: Clarendon Press, 1961.

[64] P. H. Roberts, "On the Thermal Instability of a Rotating-Fluid Sphere Containing Heat Sources," *Philosophical Transactions of the Royal Society of London. Series A, Mathematical and Physical Sciences*, vol. 263, no. 1136, pp. 93–117, 1968.

[65] F. H. Busse, "Thermal instabilities in rapidly rotating systems," *Journal of Fluid Mechanics*, vol. 44, pp. 441–460, Nov. 1970.

[66] F. H. Busse, "Convection driven zonal flows and vortices in the major planets," *Chaos: An Interdisciplinary Journal of Nonlinear Science*, vol. 4, pp. 123–134, June 1994.

[67] F. H. Busse and C. R. Carrigan, "Laboratory simulation of thermal convection in rotating planets and stars," *Science (New York, N.Y.)*, vol. 191, pp. 81–83, Jan. 1976.

[68] C. R. Carrigan and F. H. Busse, "An experimental and theoretical investigation of the onset of convection in rotating spherical shells," *Journal of Fluid Mechanics*, vol. 126, pp. 287–305, Jan. 1983.

[69] T. Gastine, J. Wicht, and J. Aubert, "Scaling regimes in spherical shell rotating convection," *Journal of Fluid Mechanics*, vol. 808, pp. 690–732, Dec. 2016.

[70] D. Wang, H. Jiang, S. Liu, X. Zhu, and C. Sun, "Effects of radius ratio on annular centrifugal Rayleigh–Bénard convection," *Journal of Fluid Mechanics*, vol. 930, p. A19, Jan. 2022.

[71] A. Pothérat and S. Horn, "Seven decades of exploring planetary interiors with rotating convection experiments," *Comptes Rendus. Physique*, vol. 25, no. S3, pp. 1–55, 2024.

[72] L. Rayleigh, "On the dynamics of revolving fluids," *Proceedings of the Royal Society of London. Series A, Containing Papers of a Mathematical and Physical Character*, vol. 93, no. 648, pp. 148–154, 1916.

[73] C. D. Andereck, S. S. Liu, and H. L. Swinney, "Flow regimes in a circular Couette system with independently rotating cylinders," *Journal of Fluid Mechanics*, vol. 164, pp. 155–183, Mar. 1986.

[74] B. Eckhardt, S. Grossmann, and D. Lohse, "Scaling of global momentum transport in Taylor-Couette and pipe flow," *The European Physical Journal B - Condensed Matter and Complex Systems*, vol. 18, pp. 541–544, Dec. 2000.

[75] B. Eckhardt, S. Grossmann, and D. Lohse, "Fluxes and energy dissipation in thermal convection and shear flows," *Europhysics Letters*, vol. 78, p. 24001, Mar. 2007.

[76] B. Eckhardt, S. Grossmann, and D. Lohse, "Torque scaling in turbulent Taylor–Couette flow between independently rotating cylinders," *Journal of Fluid Mechanics*, vol. 581, pp. 221–250, June 2007.

[77] D. Coles, "Transition in circular Couette flow," *Journal of Fluid Mechanics*, vol. 21, pp. 385–425, Mar. 1965.

[78] G. Rüdiger, M. Gellert, R. Hollerbach, M. Schultz, and F. Stefani, "Stability and instability of hydromagnetic Taylor–Couette flows," *Physics Reports*, vol. 741, pp. 1–89, Apr. 2018.

[79] H. Ji and J. Goodman, "Taylor-Couette flow for astrophysical purposes," *Philosophical Transactions of the Royal Society A: Mathematical, Physical and Engineering Sciences*, vol. 381, p. 20220119, May 2023.

[80] W. L. Haberman, "Secondary Flow about a Sphere Rotating in a Viscous Liquid inside a Coaxially Rotating Spherical Container," *The Physics of Fluids*, vol. 5, pp. 625–626, May 1962.

[81] Yu. G. Ovseenko, "Über die Bewegung einer viskosen Flüssigkeit zwischen zwei rotierenden Kugelflächen," *Izvestija VUZ, Mathematika*, vol. 4, pp. 129–139, 1963.

[82] O. Sawatzki and J. Zierep, "Das Stromfeld im Spalt zwischen zwei konzentrischen Kugelflächen, von denen die innere rotiert," *Acta Mechanica*, vol. 9, pp. 13–35, Mar. 1970.

[83] M. Wimmer, "Experiments on a viscous fluid flow between concentric rotating spheres," *Journal of Fluid Mechanics*, vol. 78, pp. 317–335, Nov. 1976.

[84] P. S. Marcus and L. S. Tuckerman, "Simulation of flow between concentric rotating spheres. Part 1. Steady states," *Journal of Fluid Mechanics*, vol. 185, pp. 1–30, Dec. 1987.

[85] P. S. Marcus and L. S. Tuckerman, "Simulation of flow between concentric rotating spheres. Part 2. Transitions," *Journal of Fluid Mechanics*, vol. 185, pp. 31–65, Dec. 1987.

[86] K. Bühler, "Symmetric and asymmetric Taylor vortex flow in spherical gaps," *Acta Mechanica*, vol. 81, pp. 3–38, Mar. 1990.

[87] Christoph Egbers, *Zur Stabilität Der Strömung Im Konzentrischen Kugelspalt*. PhD thesis, Universität Bremen, 1994.

[88] C. Egbers and H. J. Rath, "The existence of Taylor vortices and wide-gap instabilities in spherical Couette flow," *Acta Mechanica*, vol. 111, pp. 125–140, Sept. 1995.

[89] C. Egbers and G. Pfister, eds., *Physics of Rotating Fluids: Selected Topics of the 11th International Couette-Taylor Workshop, Held at Bremen, Germany, 20-23 July 1999*. No. 549 in Lecture Notes in Physics, Berlin ; New York: Springer, 2000.

[90] R. Hollerbach, M. Junk, and C. Egbers, "Non-axisymmetric instabilities in basic state spherical Couette flow," *Fluid Dynamics Research*, vol. 38, pp. 257–273, Apr. 2006.

[91] F. Feudel and U. Feudel, "Bifurcations in rotating spherical shell convection under the influence of differential rotation," *Chaos: An Interdisciplinary Journal of Nonlinear Science*, vol. 31, p. 113112, Nov. 2021.

[92] C. E. Pearson, "A numerical study of the time-dependent viscous flow between two rotating spheres," *Journal of Fluid Mechanics*, vol. 28, pp. 323–336, May 1967.

[93] B. R. Munson and D. D. Joseph, "Viscous incompressible flow between concentric rotating spheres. Part 1. Basic flow," *Journal of Fluid Mechanics*, vol. 49, pp. 289–303, Sept. 1971.

[94] B. R. Munson and D. D. Joseph, "Viscous incompressible flow between concentric rotating spheres. Part 2. Hydrodynamic stability," *Journal of Fluid Mechanics*, vol. 49, pp. 305–318, Sept. 1971.

[95] B. R. Munson and M. Menguturk, "Viscous incompressible flow between concentric rotating spheres. Part 3. Linear stability and experiments," *Journal of Fluid Mechanics*, vol. 69, pp. 705–719, June 1975.

[96] I. Proudman, "The almost-rigid rotation of viscous fluid between concentric spheres," *Journal of Fluid Mechanics*, vol. 1, pp. 505–516, Nov. 1956.

[97] K. Stewartson, "On almost rigid rotations," *Journal of Fluid Mechanics*, vol. 3, pp. 17–26, Oct. 1957.

[98] K. Stewartson, "On almost rigid rotations. Part 2," *Journal of Fluid Mechanics*, vol. 26, pp. 131–144, Sept. 1966.

[99] N. Schaeffer and P. Cardin, "Quasigeostrophic model of the instabilities of the Stewartson layer in flat and depth-varying containers," *Physics of Fluids*, vol. 17, p. 104111, 2005.

[100] R. Hollerbach, "Instabilities of the Stewartson layer Part 1. The dependence on the sign of," *Journal of Fluid Mechanics*, vol. 492, pp. 289–302, Oct. 2003.

[101] M. Wimmer, "Viscous flows and instabilities near rotating bodies," *Progress in Aerospace Sciences*, vol. 25, pp. 43–103, Jan. 1988.

[102] M. Wimmer, "Experiments on the stability of viscous flow between two concentric rotating spheres," *Journal of Fluid Mechanics*, vol. 103, pp. 117–131, Feb. 1981.

[103] K. Nakabayashi and Y. Tsuchida, "Transition phenomena in a spherical Couette flow between independently rotating spheres," *Physics of Fluids*, vol. 17, p. 104110, Oct. 2005.

[104] S. B. Pope, *Turbulent Flows*. Cambridge University Press, Aug. 2000.

[105] "OpenFOAM Documentation." https://www.openfoam.com/documentation/overview.

[106] L. S. Caretto, A. D. Gosman, S. V. Patankar, and D. B. Spalding, "Two calculation procedures for steady, three-dimensional flows with recirculation," in *Proceedings of the Third International Conference on Numerical Methods in Fluid Mechanics* (H. Cabannes and R. Temam, eds.), Lecture Notes in Physics, (Berlin, Heidelberg), pp. 60–68, Springer, 1973.

[107] "OpenFOAM: User Guide: GAMG Solver." https://www.openfoam.com/documentation/guides/latest/doc/guide-solvers-multigrid-gamg.html.

[108] Y. Gaillard, P. S. B. Szabo, V. Travnikov, and C. Egbers, "Modelling Thermo-Electrohydrodynamic Convection in Rotating Spherical Shell Using OpenFOAM®," *OpenFOAM® Journal*, vol. 5, pp. 1–16, Jan. 2025.

[109] T. Seelig, U. Harlander, R. Faulwetter, and C. Egbers, "Irregularity and singular vector growth in the differentially heated rotating annulus," *Theoretical and Computational Fluid Dynamics*, vol. 27, June 2012.

[110] T. von Larcher and A. Dörnbrack, "Numerical simulations of baroclinic driven flows in a thermally driven rotating annulus using the immersed boundary method," *Meteorologische Zeitschrift*, vol. 23, pp. 599–610, Jan. 2015.

[111] I. M. Yavorskaya, N. I. Fomina, and Yu. N. Belyaev, "A simulation of central-symmetry convection in microgravity conditions," *Acta Astronautica*, vol. 11, pp. 179–183, Mar. 1984.

[112] N. Rieger and S. J. Levang, "Xeofs: Comprehensive EOF analysis in Python with xarray," *Journal of Open Source Software*, vol. 9, p. 6060, Jan. 2024.

[113] N. Rieger and S. J. Levang, "Xeofs." Zenodo, Sept. 2024.

[114] D. Moore and N. Weiss, "Two Dimensional Rayleigh-Benard Convection," *Journal of Fluid Mechanics - J FLUID MECH*, vol. 58, pp. 289–312, Apr. 1973.

[115] S. Grossmann and D. Lohse, "Scaling in thermal convection: A unifying theory," *Journal of Fluid Mechanics*, vol. 407, pp. 27–56, Mar. 2000.

[116] N. Ouertatani, N. Ben Cheikh, B. Ben Beya, and T. Lili, "Numerical simulation of two-dimensional Rayleigh–Bénard convection in an enclosure," *Comptes Rendus Mécanique*, vol. 336, pp. 464–470, May 2008.

[117] B. R. Munson, *Hydrodynamic Stability of Flow between Rotating Spheres and Rotating-Sliding Cylinders*. PhD thesis, Univ. of Minnesota., 1970.

[118] C. Guervilly and P. and Cardin, "Numerical simulations of dynamos generated in spherical Couette flows," *Geophysical & Astrophysical Fluid Dynamics*, vol. 104, pp. 221–248, Apr. 2010.

[119] Y. Gaillard, P. S. Szabo, and C. Egbers, "Thermo-electrohydrodynamic convection in the thermally driven spherical shell with differential rotation," *PAMM*, vol. n/a, no. n/a, p. e202300036, 2023.

[120] R. Badent and M. Suriyah, "Ermittlung der dielektrischen Eigenschaften der Flüssigkeit 3M Novec 7200," Tech. Rep. 2018-20, Institut für Elektroenergiesysteme und Hochspannungstechnik (KIT), 2018.

[121] "3M Novec 7200 High-Tech Flüssigkeit | 3M Deutschland," tech. rep.

[122] "Magic 6.3." https://magic-sph.github.io/.

[123] J. Wicht, "Inner-core conductivity in numerical dynamo simulations," *Physics of the Earth and Planetary Interiors*, vol. 132, pp. 281–302, Oct. 2002.

[124] T. Gastine and J. Wicht, "Effects of compressibility on driving zonal flow in gas giants," *Icarus*, vol. 219, pp. 428–442, May 2012.

[125] N. Schaeffer, "Efficient spherical harmonic transforms aimed at pseudospectral numerical simulations," *Geochemistry, Geophysics, Geosystems*, vol. 14, pp. 751–758, Mar. 2013.

[126] U. Christensen, J. Aubert, P. Cardin, E. Dormy, S. Gibbons, G. Glatzmaier, E. Grote, Y. Honkura, C. Jones, M. Kono, M. Matsushima, A. Sakuraba, F. Takahashi, A. Tilgner, J. Wicht, and K. Zhang, "A numerical dynamo benchmark," *Physics of the Earth and Planetary Interiors*, vol. 128, pp. 25–34, Dec. 2001.

[127] C. Jones, P. Boronski, A. Brun, G. Glatzmaier, T. Gastine, M. Miesch, and J. Wicht, "Anelastic convection-driven dynamo benchmarks," *Icarus*, vol. 216, pp. 120–135, Nov. 2011.

[128] R. K. Yadav, T. Gastine, U. R. Christensen, and A. Reiners, "Formation of starspots in self-consistent global dynamo models: Polar spots on cool stars," *Astronomy & Astrophysics*, vol. 573, p. A68, Jan. 2015.

A Appendix

A.1 Fluid properties

The fluid in use in the experiment is an ethoxynonafluorbutan ($C_4F_9OC_2H_5$) derivative called Novec7200 and a dielectric fluid, which inhibits the flow of free charges. The permittivity and density change with rising temperature. For small temperature variations, a linear description, also called the Bousinessq approximation, can be processed.

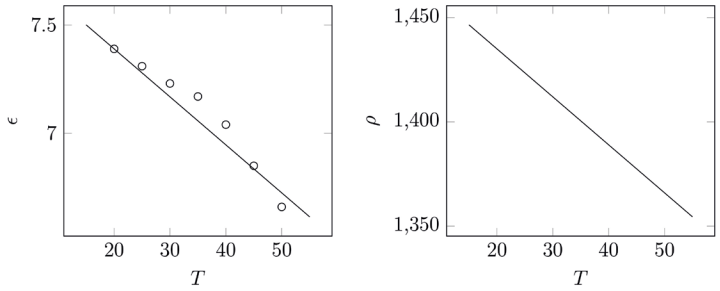

(a) Electric permitvity over temperature from [120]

(b) Density over temperature from [121]

Figure A.1.: Novec's material properties over temperature.

The density change from temperature affects the centrifugal buoyancy. Despite its known effect on the flow it is not included in this thesis and the focus remain on the interarction of TEHD with the differential rotation, since for the range of selected rotation the centrifugal buoyancy has a minor role compare to the differential rotation.

Also Novec7200 has a permanment dipole moment. When applying an electric field, the polarity causes the molecules to orient accordingly. Using an alternating current as a

Property	Symbol	Value
Electric permittivity relative	ϵ_r	7.39
Thermal permitivity coeff.	e	$0.003\,\mathrm{K}^{-1}$
Density at 293K	ρ_0	$1435\,\mathrm{kgm}^{-3}$
Thermal expansion coeff.	β	$0.0016\,\mathrm{K}^{-1}$
Viscosity at 293K	ν	$4.71 \cdot 10^{-7}\,\mathrm{m}^2\mathrm{s}^{-1}$
Thermal diffusivity at 293K	κ	$4.0992 \cdot 10^{-8}\,\mathrm{m}^2\mathrm{s}^{-1}$
Prandtl number	Pr	11.49

source leads to the molecules' oscillation. At a high frequency, this oscillation causes losses transferred in heat.

A.2 Solver algorithm

A brief overview of SIMPLE and PISO is provided in this section, focusing on their development in conjunction with the solution of the Gauss equation.

A.2.1 SIMPLE

Figure A.2 shows the loops implemented in the SIMPLE algorithm. The momentum and temperature equations are not time-dependent in this context. The matrices are solved until the chosen residual is achieved, ensuring that the defined boundary conditions are met. An iteration is similar to a time step, where the simulation develops from the initial state. The change from one iteration to the next, however, is not physical.

A.2.2 PISO

Figure A.3 shows the flowchart for an example solver using the PSIO algorithm for a single timestep. The time-dependent temperature and momentum equations necessitate the physical time. The time step must be less than 1 in this algorithm. Via the corrector and orthogonal corrector loops, the target residual is reached. Note that the solver does not check the residual on its own. This causes unnecessary iterations in the corrector loops where the residual is met before the loops are completed.

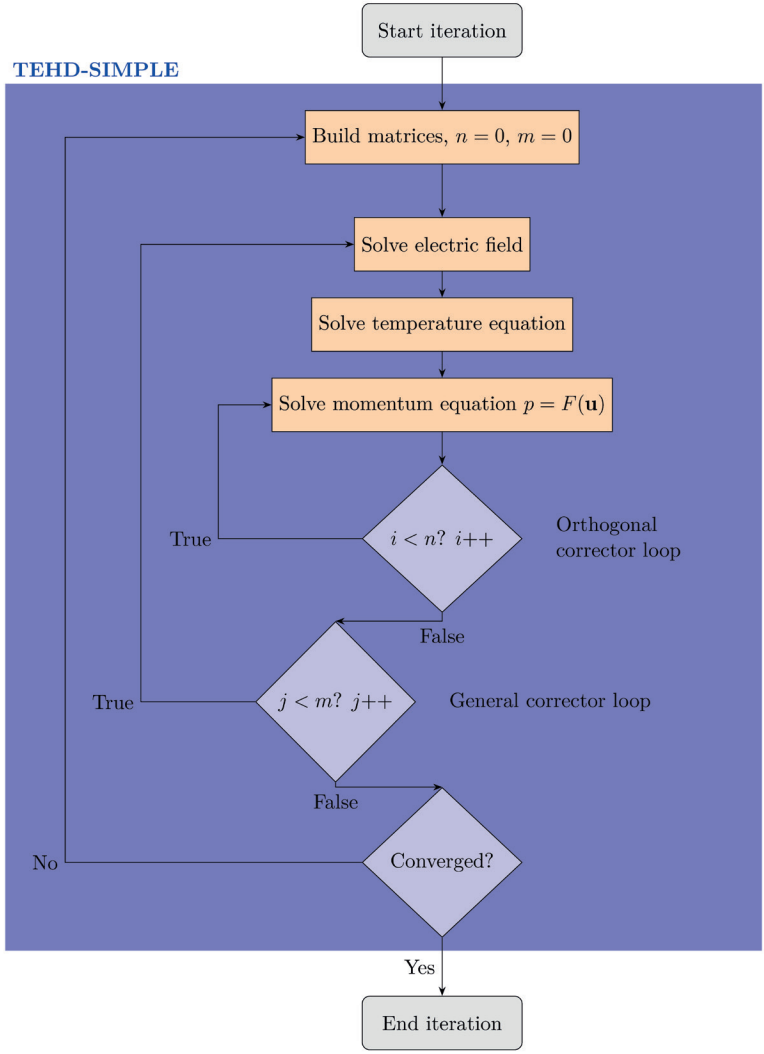

Figure A.2.: Flowchart showing the different loops the TEHD-SIMPLE solver uses until reaching convergence.

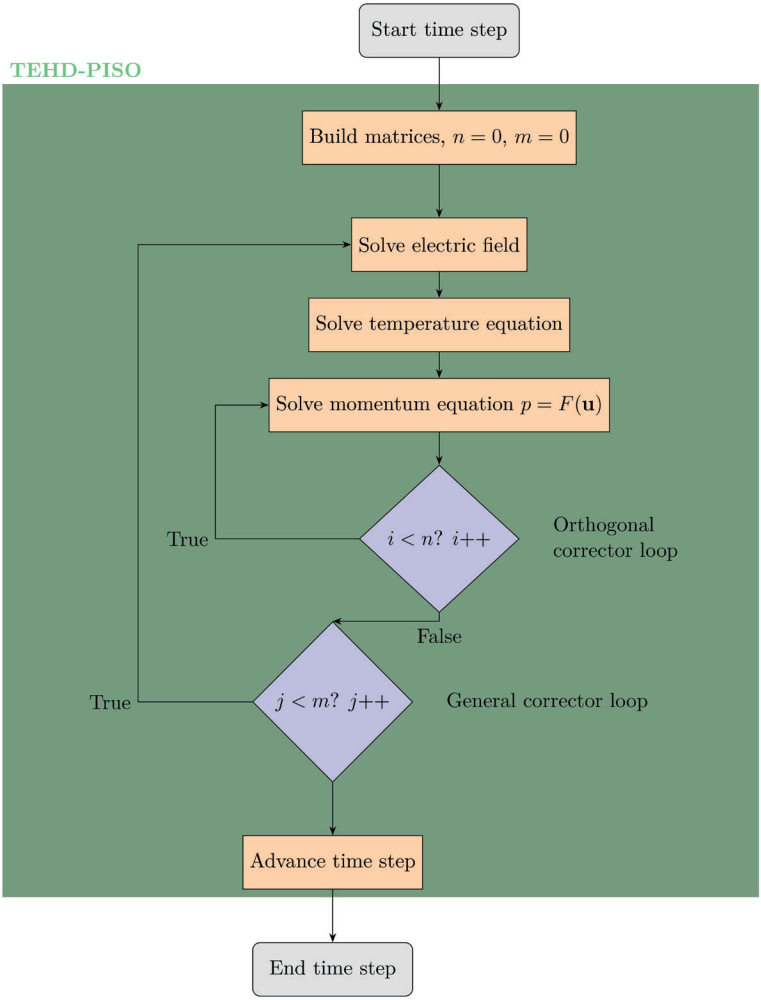

Figure A.3.: Flowchart showing the different loops the TEHD-PISO solver processing one time-step.

A.3 Differential rotation verification

The correct implementation of the TEHD was verified in Gaillard et al. work [14]. However, the differential rotation side shall also be verified. This task is performed by comparing the results of four example cases, which remain stable. The simulation is processed with commercial software COMSOL using Finite Element Method (FEM) and using open-source MagIC code. For all processed cases, the radial, meridional and azimuthal velocity contours are plotted (see Figure A.4). The verification shall especially confirm the usage of a rotating reference frame since the error in the sign may result in a completely different result. The FEM use a relative coarse mesh less than $1 \cdot 10^6$ element with quadratic dicretisation.
MagIC [122] uses the PSM and is developed for magneto-hydrodynamics in stellar bodies. Developed initially by Wicht [20, 123], later continued by Gastine [124] and supported by Schäffer [125], Christensen et al. [126], Jones et al. [127] and Yadav et al. [128].

For each case, the overall contours of all three methods seem to match well. There are small artifact noticiable for the radial velocity in equatorial region which are present for the FVM and FEM but not for the PSM. An artefact is also noticeable for the Taylor number $3.31 \cdot 10^4$ in the midlatitude region for the meridional velocity. The author's knowledge is limited for the PSM, hence the origin of those artefacts cannot be explained. Besides, the velocity extrema match well and one can conclude that MagIC were correctly used for this verification. The non-linearity effect could also be well resolved using MagIC and the FEM which are absent in the method used by Munson in Figure 6.1. The result from this testcase shows therefore an adequate implementation of differential rotation in OpenFOAM.

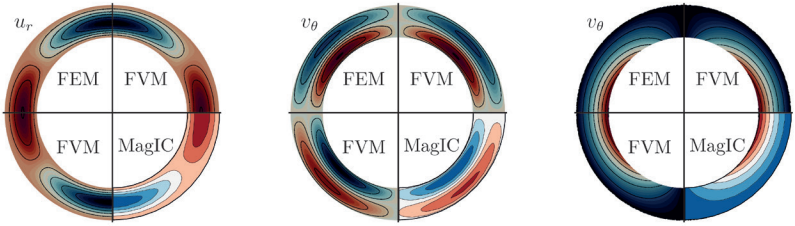

(a) Contour of radial velocity u_r: $u_{r,min} = -1.43(0.36)$, $u_{r,max} = 0.71(0.18)$ and meridional velocity u_θ: $u_{\theta,min} = -3.52(0.88)$, $u_{\theta,max} = 3.52(0.88)$ at $Ta = 110.3$

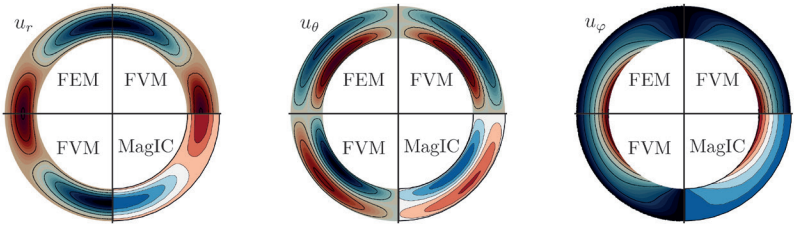

(b) Contour of radial velocity u_r: $u_{r,min} = -6.90(1.72)$, $u_{r,max} = 3.37(0.84)$ and meridional velocity u_θ: $u_{\theta,min} = -16.9(4.23)$, $u_{\theta,max} = 16.9(4.23)$ at $Ta = 600.6$

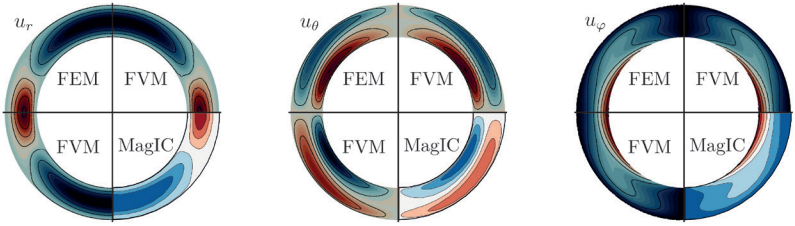

(c) Contour of radial velocity u_r: $u_{r,min} = -49.3(12.3)$, $u_{r,max} = 27.7(6.92)$ and meridional velocity u_θ: $u_{\theta,min} = -191.6(47.9)$, $u_{\theta,max} = 191.6(47.9)$ at $Ta = 4.42 \cdot 10^3$

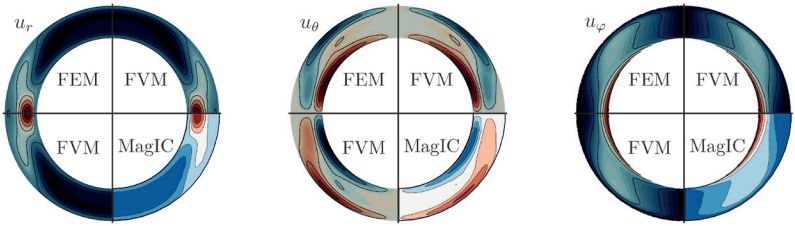

(d) Contour of radial velocity u_r: $u_{r,min} = -49.3(12.3)$, $u_{r,max} = 27.7(6.92)$ and meridional velocity u_θ: $u_{\theta,min} = -191.6(47.9)$, $u_{\theta,max} = 191.6(47.9)$ at $Ta = 3.31 \cdot 10^4$

Figure A.4.: Isosurface of velocities for verification of implementation of differential rotation.

A.4 Derivation of the In-Flow Nusselt number

This method follows the approach used by Wang [70] for cylindrical cavities, and it is based on the work of Eckhardt [76].

For clarity, we substitute the spherical coordinate variables u_r, u_θ, and u_φ with:

$$u = u_r, v = u_\theta, , w = u_\varphi \tag{A.1}$$

We then define an average over spherical surfaces and time, showing that the operation is commutative with respect to r:

$$\langle \dots \rangle_{A,t} = \int \frac{r^2 \sin(\theta)}{4\pi r^2} d\theta d\varphi \cdots = \frac{1}{4\pi} \int \sin(\theta) d\theta \int d\varphi \dots \tag{A.2}$$

This averaging is valid for flows when they are measured over a sufficiently long timespan. All flows are driven by differential rotation, which in these regimes is both equatorially and rotationally symmetric. The meridional and azimuthal components, therefore, cancel each other out.

The dimensionless temperature, as defined in eq. (2.38), is now expressed in spherical coordinates:

$$\frac{DT}{Dt} = \boldsymbol{\nabla}^2 T \tag{A.3}$$

$$\partial_t T + u\partial_r T + \frac{v}{r}\partial_\theta T + \frac{w}{r\sin\theta}\partial_\varphi T = \frac{1}{r^2}\partial_r\left(r^2\partial_r T\right) + \frac{1}{r^2\sin\theta}\partial_\theta\left(\sin(\theta)\partial_\theta T\right) + \frac{1}{r^2\sin(\theta)^2}\partial_\varphi^2 T \tag{A.4}$$

By incorporating the continuity equation in spherical coordinates and multiplying it by the temperature

$$T \cdot \left(\frac{1}{r^2}\partial_r(r^2 u) + \frac{1}{r\sin\theta}\partial_\theta(v\sin\theta) + \frac{1}{r\sin\theta}\partial_\varphi w\right) = 0 \cdot T \tag{A.5}$$

$$\frac{2uT}{r} + T\partial_r u + \frac{vT\cot\theta}{r} + \frac{T}{r}\partial_\theta v + \frac{T}{r\sin\theta}\partial_\varphi w = 0 \tag{A.6}$$

to eq. (A.4) the partial differential can be factorised. After some transformations, this leads to the following equation

$$\begin{aligned} \partial_t T + \frac{1}{r^2}\left(\partial_r(r^2 uT) - \partial_r\left(r^2\partial_r T\right)\right) &+ \\ \frac{1}{r\sin\theta}\left(\partial_\theta(\sin(\theta)vT) - \frac{1}{r}\partial_\theta\left(\sin(\theta)\partial_\theta T\right)\right) &+ \\ \frac{1}{r\sin\theta}\left(\partial_\varphi wT - \frac{1}{r\sin(\theta)}\partial_\varphi^2 T\right) &= 0 \end{aligned} \tag{A.7}$$

$$\begin{aligned} \partial_t T + \frac{1}{r}\left(\partial_r\left(r^2\left[uT - \partial_r T\right]\right)\right) &+ \\ \frac{1}{\sin\theta}\left(\partial_\theta\left(\sin\theta\left[vT - \frac{1}{r}\partial_\theta T\right]\right)\right) &+ \\ \frac{1}{\sin\theta}\left(\partial_\varphi\left(wT - \frac{1}{r\sin(\theta)}\partial_\varphi T\right)\right) &= 0 \end{aligned} \tag{A.8}$$

Applying the time and spatial average as in eq. (A.2), following Wang's [70] method, simplifies this to:

$$\left\langle \partial_r\left(r^2\left[uT - \partial_r T\right]\right)\right\rangle_{A,t} = 0 \tag{A.9}$$

Since operations with r are commutative, integration with respect to r can be performed from both sides. The resulting heat flux, when normalised by the conductive heat flux, is referred to as the in-flow Nusselt number, denoted as Nu^q, and is given by:

$$\mathrm{Nu}^q = \frac{(\eta-1)^2}{4\pi\eta}\left\langle\left(r^2\left[uT - \partial_r T\right]\right\rangle_{A,t}\right. \tag{A.10}$$